PHASED ARRAYS FOR METEOROLOGICAL SATELLITE

By Charles E. Profera, Jr.

June 1967

TABLE OF CONTENTS

LIST OF ILLUSTRATIONS

ACKNOWLEDGMENT

PHASED ARRAYS FOR METEOROLOGICAL SATELLITE

By Charles E. Profera, Jr.

Radio Corporation of America
Moorestown, New Jersey

SUMMARY

Multimode techniques have been applied to the design of an E-plane sectoral horn to produce tapered line source illuminations resulting in low-sidelobe patterns. An H-plane array of multimode horns can be combined through a multimode power combiner to provide a single-plane electronic scan capability.

Basic design data for the multimode line source has been formulated and two array configurations considered.

The staggered array consists of two linear arrays of multimode half-horns displaced from each other in the H-plane by one-half the element width to eliminate grating lobes along the scan axis. Patterns recorded from a pair of multimode half-horns exhibited maximum side lobe levels of -30 dB over a frequency band in excess of 5%. Projected array beam efficiency ranged from 92% to 96% over a 10% frequency band. An analysis of the staggered array geometry revealed a pair of grating lobes equally displaced about the scan axis appearing in visible space as the beam is scanned only a few degrees. Beam efficiency is seriously degraded to the extent that the staggered array concept is unsuitable for incorporation into a scanned array.

A parallel array of reduced-width multimode horns was evaluated for reduced bandwidth and scan capability. Pattern measurements in the plane of the line source revealed a negligible effect due to the presence of the dummy elements.

An analysis was made to determine the effect of phase shifter errors on array patterns. The errors associated with a 5-bit phase shifter typically increase maximum computed sidelobes resulting in a decrease of beam efficiency.

1

INTRODUCTION

Phased array antennas operated at frequencies above X-band are generally characterized by high insertion loss. Attempts to reduce this loss generally results in a design which is inherently narrow band. A satellite-borne phased array antenna for radiometric measurements must exhibit low noise temperature and high beam efficiency, with wide-band characteristics an attractive feature.

This report discusses the analysis and evaluation of a basic multimode horn line source element for an array of line sources. The inherent low loss of the waveguide horn and its intended multimode horn power combiner along with the sidelobe level and beam efficiency control attended by multimode aperture distribution tapering techniques make this an attractive array antenna for operation at frequencies above X-band. Bandwidth of a multimode sectoral horn for array application is typically about 5%.

THEORY OF MULTIMODE TECHNIQUES

Techniques requiring generation and radiation of several waveguide modes have been utilized recently (Ref. 1, 2, 3) for controlling the shape and reducing the sidelobe levels of the radiation patterns of horn feeds for large reflector antennas. The multimode horn feeds discussed in the literature to date have been relatively low-gain pyramidal or conical horns having dual polarization symmetry. The most directive of these feeds are used in the Cassegrain reflector geometry and have typical half power beamwidths of 15 to 25 degrees with horn apertures of 3 to 5 wavelengths.

Multimode sidelobe reduction techniques can be applied equally well to the linearly polarized sectoral horn resulting in a continuous aperture line source whose radiation pattern exhibits very low sidelobe levels. Using an aperture lens to correct the inherent field curvature of the flared horn permits the design of a long line source with a relatively short horn. Half-power beamwidths of only a few degrees can be realized in applications of this technique.

A directive array of multimode line sources can be realized by utilizing the sectoral horn arrangement shown in Figure 1. If E-plane multimode sectoral horns are employed, H-plane electronic scanning can be provided by incorporation of electronically variable phase shifters at the horn inputs. The E-plane array pattern will be essentially that of a single line source and will possess the same low sidelobe characteristics. Low H-plane array sidelobes and consequently high beam efficiency can be obtained by incorporating a beamformer to provide a suitable tapered aperture distribution in the H-plane of the array. Utilizing optical power division techniques for the H-plane beamformer will result in an extremely low loss array. Hybrid couplers and magic tees are excluded from the full array thereby eliminating the losses of these elements and their interconnecting waveguide.
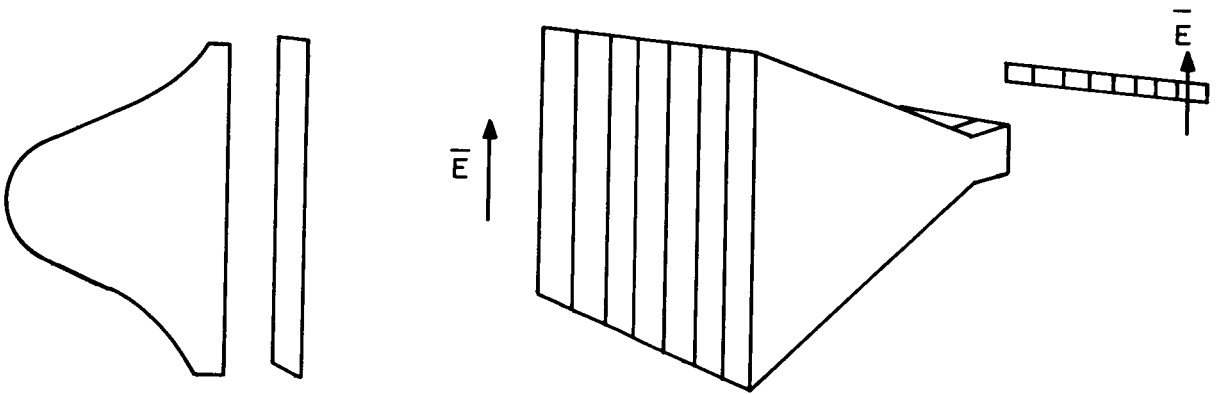
Figure 1. Continuous Line Source Array

The low sidelobe levels, high beam efficiency and low loss characteristics of the multimode array make it well suited for use in radiometric applications.

Pattern Sidelobe Beamwidth and Beam Efficiency Control

Techniques employed to provide aperture distribution tapering in the E-plane of a rectangular waveguide radiator require generation of at least two modes, the TE_{10} and LSE_{12}. The TE_{10} mode is the dominant waveguide mode and is characterized by

the electric field distribution shown in Figure 2. The expression for the TE_{10} mode electric field distribution is given in equation (1) for a y-polarized field

$$\bar{E}_{10}\ (x, y) = a_{10} \cos \frac{\pi x}{a} \bar{\imath}_y \tag{1}$$
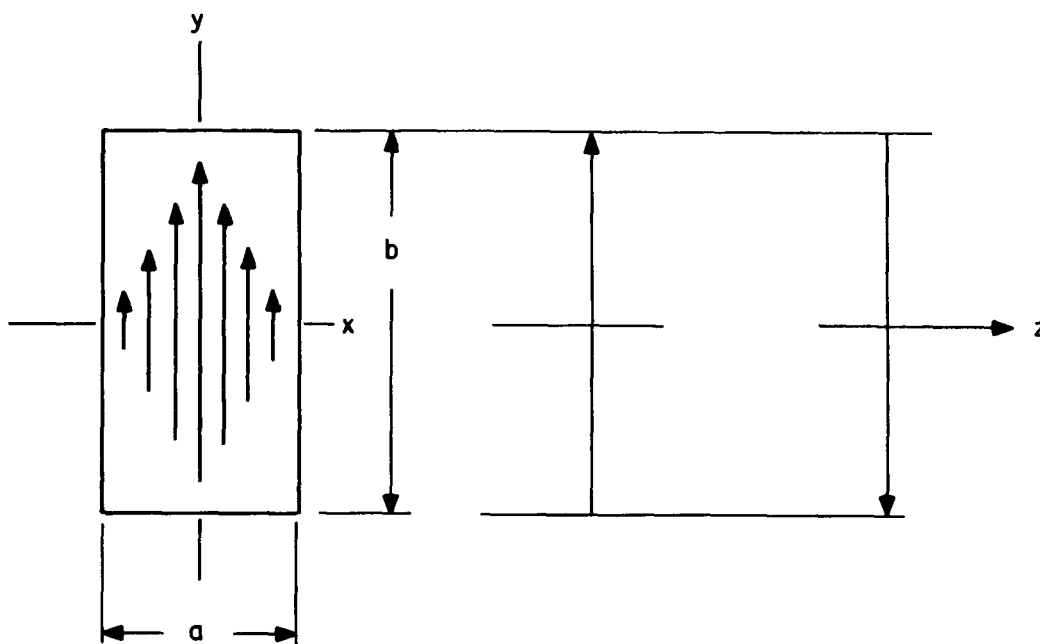
Figure 2. TE_{10} Mode $\bar{E}$ Field Distribution

The LSE_{12} mode is a hybrid mode formed by a combination of the TE_{12} and TM_{12} modes. The TE_{12} and TM_{12} rectangular waveguide modes are a degenerate pair (i.e., they have equal phase velocities but different field configurations) permitting combination to form the single hybrid LSE_{12} mode. The electric field distribution of the LSE_{12} mode is shown in Figure 3. The transverse electric field distribution of the LSE_{12} mode is given in equation (2) for a y-polarized field

$$\bar{E}_{12}\ (x, y) = a_{12} \cos \frac{\pi x}{a} \cos \frac{2 \pi y}{b} \bar{\imath}_y \tag{2}$$

The LSE_{12} mode is a "longitudinal section" E mode (i.e. zero x-component of electric field) from which the terminology is derived.

4
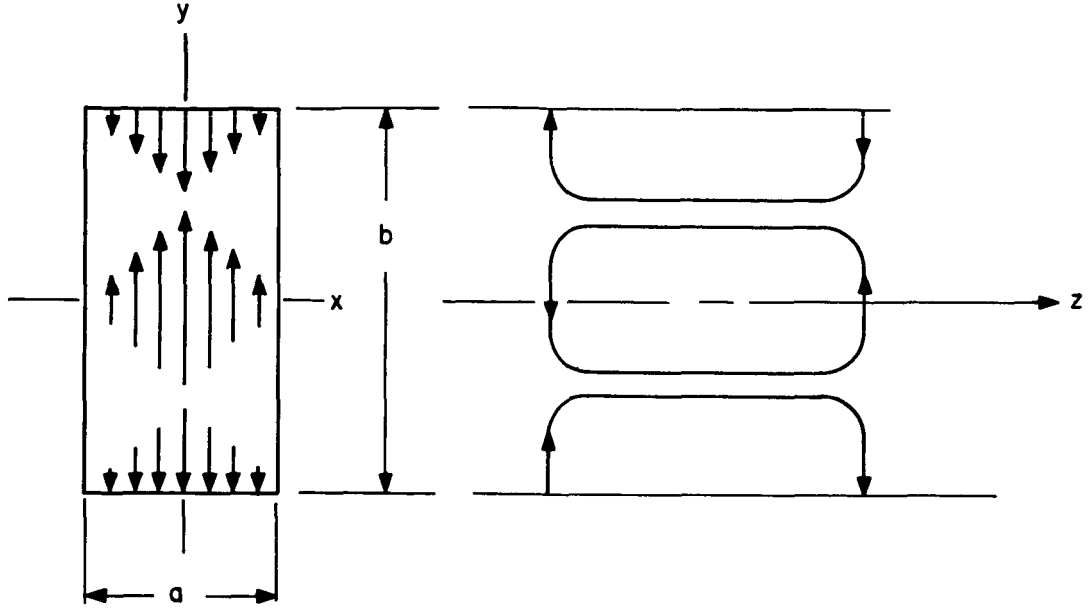
Figure 3. LSE_{12} Mode $\bar{E}$ Field Distribution

In-phase, principal plane, aperture field distributions for the TE_{10} and LSE_{12} modes are illustrated in Figure 4. It is evident that by adding the in-phase distributions a resultant tapered E-plane distribution is produced while the inherent tapered H-plane distribution is retained. The resultant normallized E-plane distribution is plotted in Figure 5. The E-plane aperture distribution, hence the E-plane radiation pattern characteristics, can be adjusted by control of the mode amplitude ratio a_{12}/a_{10}.

The radiation pattern from a rectangular aperture excited in the TE_{10} and LSE_{12} modes (Ref. 4) is

$$f(\theta, \phi) = \frac{\sin u_b \cos u_a}{u_b \left[(\pi/2)^2 - u_a^2\right]} + \frac{a_{12} u_b \sin u_b \cos u_a}{a_{10} \left[\pi^2 - u_b^2\right] \left[(\pi/2)^2 - u_a^2\right]} e^{j \alpha_M} \tag{3}$$

where

$$u_a = \frac{\pi a}{\lambda} \sin \theta \sin \phi \, ; \, u_b = \frac{\pi b}{\lambda} \sin \theta \cos \phi$$

θ and ϕ are the spherical antenna coordinates shown in Figure 6. α_M = aperture phase difference between TE_{10} and LSE_{12} modes.
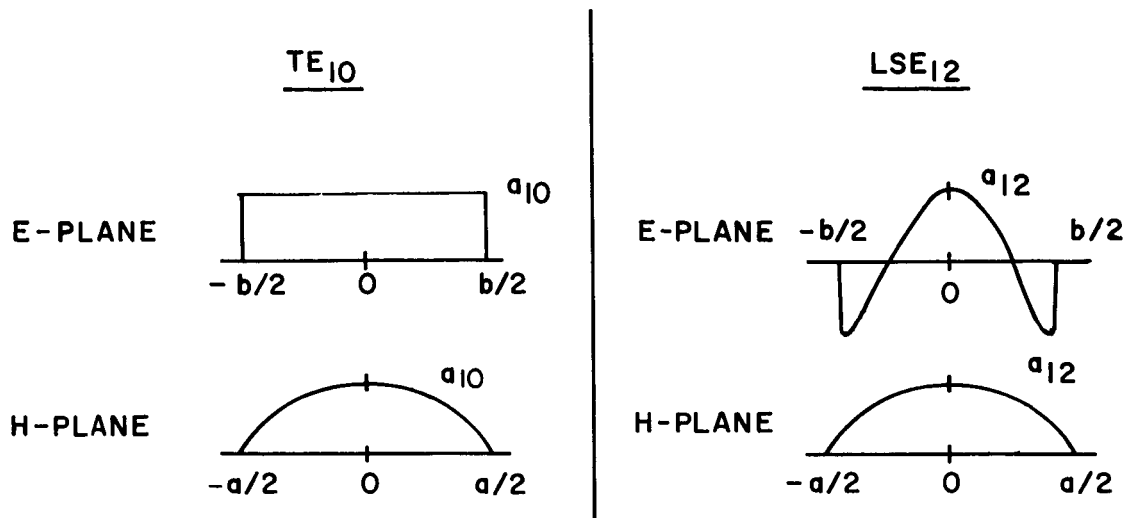
Figure 4. In-Phase Principal Plane $\overline{E}$ Distributions
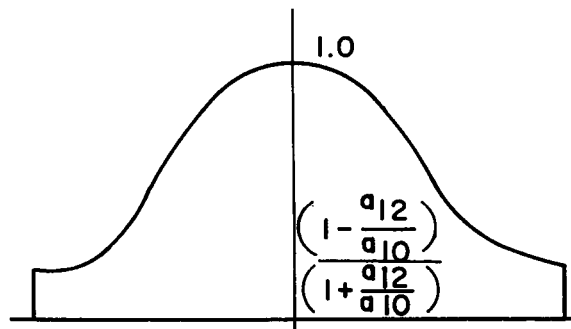
Figure 5. $TE_{10} + LSE_{12}$ In-Phase E-Plane Distributions

The maximum sidelobe level and half-power beamwidth of the computed composite mode E-plane radiation pattern, $f(u_b, \pi/2)$, is plotted vs a_{12}/a_{10} in Figure 7 with α_M as a parameter. For the in-phase case ($\alpha_M = 0$), the maximum sidelobe is less than -30 dB for $0.65 < a_{12}/a_{10} < 1.05$. For the case where a ±20-degree aperture mode phase difference exists, the maximum sidelobe level is below -25 dB for the same range of mode amplitude ratios. This data indicates the feasibility of using multimode radiators as low-sidelobe antennas over some bandwidth specified by α_M.
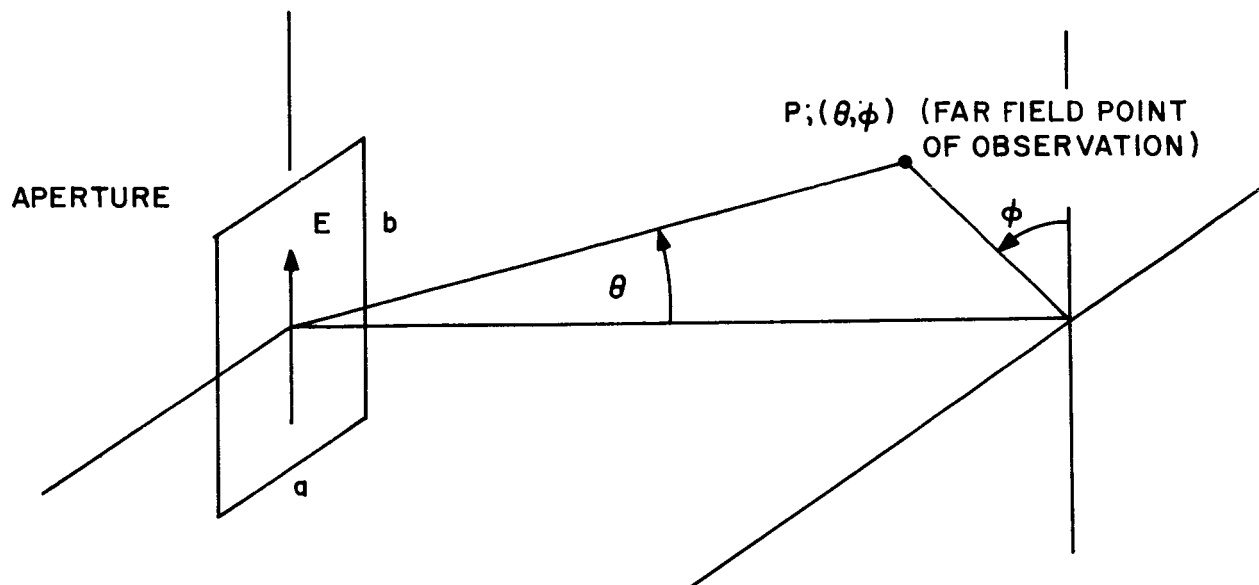
Figure 6. Antenna Co-ordinate System

Beam efficiency (η_B), which is defined as the ratio of power in the main beam of the antenna to the total power radiated or absorbed by the antenna through all space, is plotted vs mode amplitude ratio a_{12}/a_{10} with α_M as a parameter for computed multimode line source patterns of revolution in Figure 8. Beam efficiency exceeds 98.5% for $0.6 < a_{12}/a_{10} < 1.0$ where $\alpha_M = 0$. For optimum design over a maximum bandwidth a mode amplitude ratio in the vicinity of 0.8 is required. Beam efficiency for this ratio exceeds 96.5% for $|\alpha_M| \leq 20°$.

Mode Generation Techniques

There are several methods which may be employed to generate the LSE_{12} mode. Examples of the most common are shown in Figures 9(a) to (d). The most practical of these, for most applications, is the step mode generator shown in Figure 9(d). Generation of an LSE_{12} mode is accomplished by providing a symmetrical step discontinuity in the path of an incident TE_{10} wave for the geometry of Figure 9(d). If the larger waveguide supports LSE_{12} mode propagation while the smaller does not, an LSE_{12} mode will be launched which propagates only in the larger section with the remaining component of TE_{10} mode. The LSE_{12} mode will be generated in phase

7
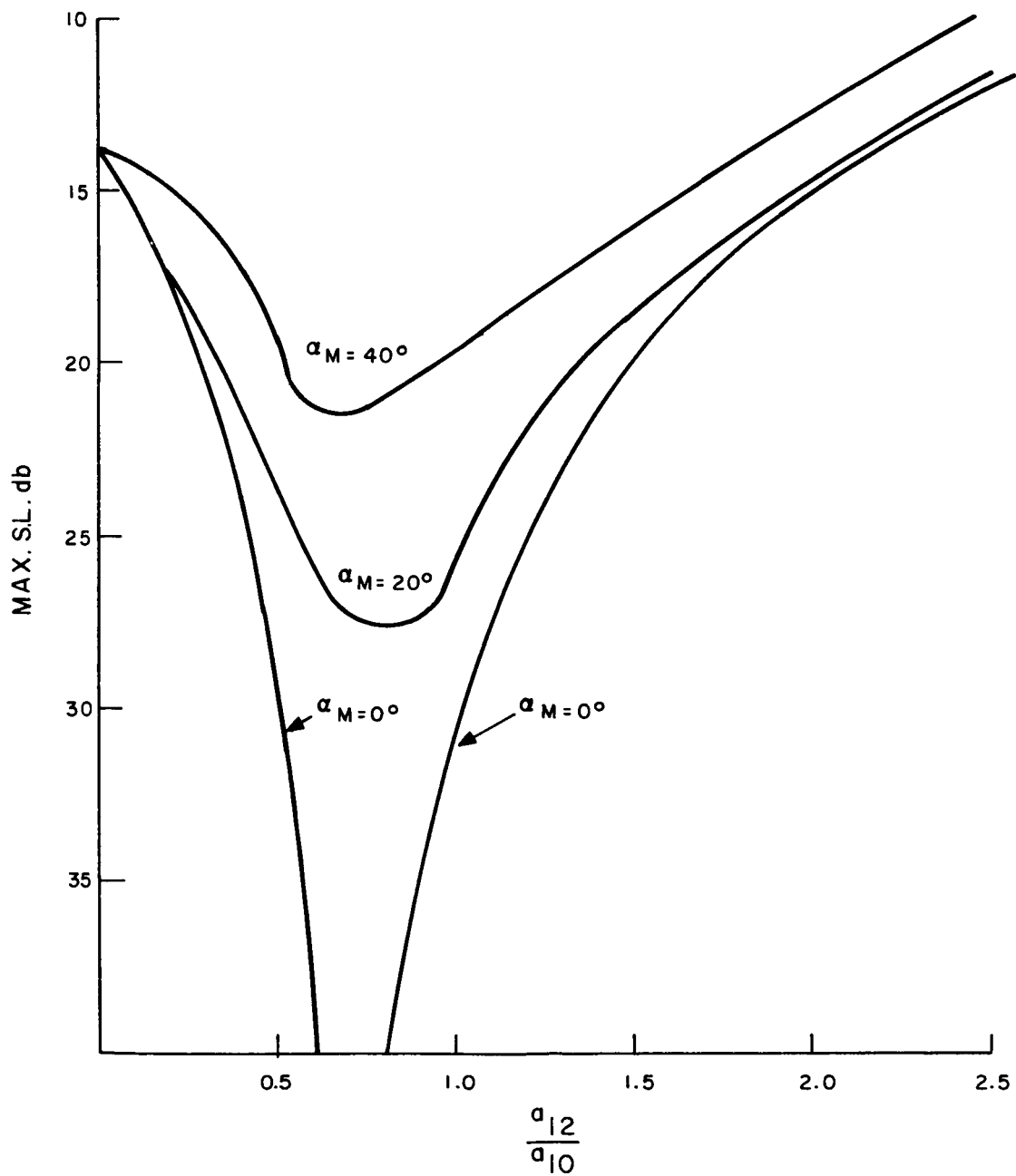
Figure 7.   Maximum E-Plane Sidelobe in dB vs a_{12}/a_{10}

with the TE_{10} mode at the step. The mode amplitude ratio, a_{12}/a_{10}, is a function of the two waveguide dimensions. This relationship will be discussed further in the following section. Additional higher order modes may be generated at the discontinuity. The step symmetry will permit generation of only those TE_{mn}, TM_{mn} modes that are even functions in y (n = even integer) where the origin of coordinates is located at the guide center. The problem of unwanted higher order mode generation is avoided by restricting the dimensions of the larger waveguide to support only TE_{10} and LSE_{12} mode propagation. All TE_{mn} and TM_{mn} modes with n ≥ 4 will be cut off in this section.
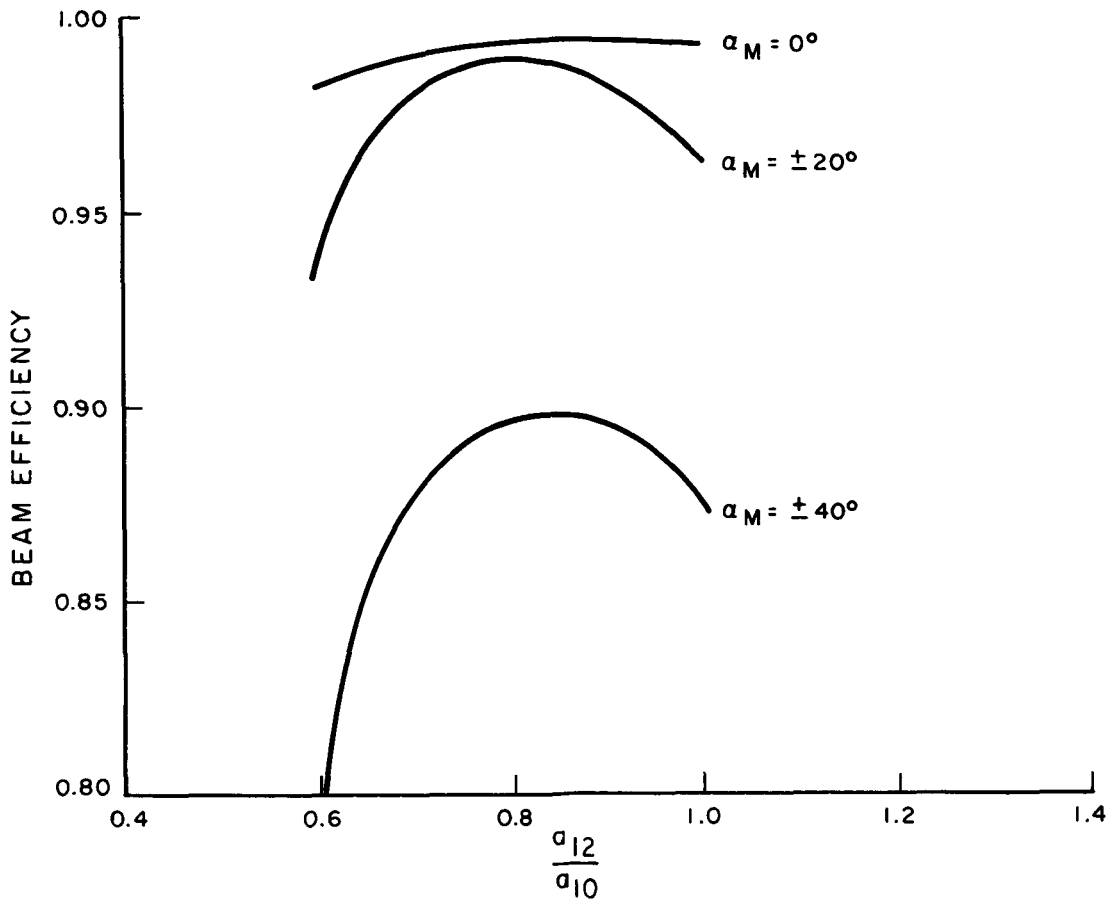
Figure 8. Beam Efficiency vs Mode Amplitude Ratio (a_{12}/a_{10}) for Multimode Pattern of Revolution

a)
TE$_{10}$ →   LSE$_{12}$ →
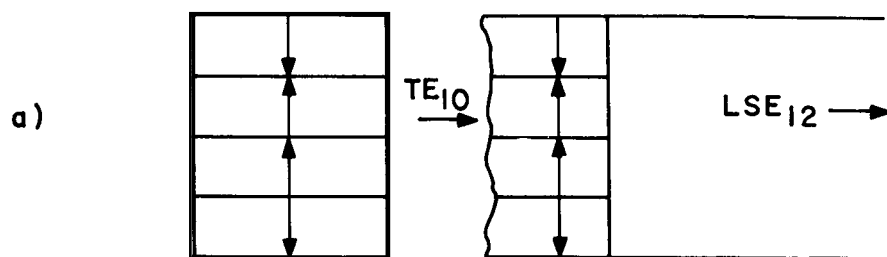
WAVEGUIDE GENERATOR

b)
TE$_{10}$ →   TE$_{10}$ →
LSE$_{12}$ ←   LSE$_{12}$ →
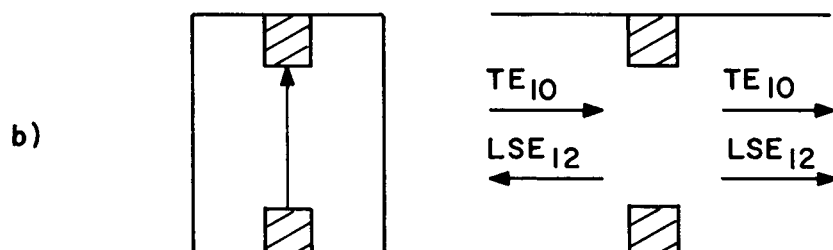
REACTIVE POST GENERATOR

c)
TE$_{10}$ →   TE$_{10}$ →
LSE$_{12}$ ←   LSE$_{12}$ →
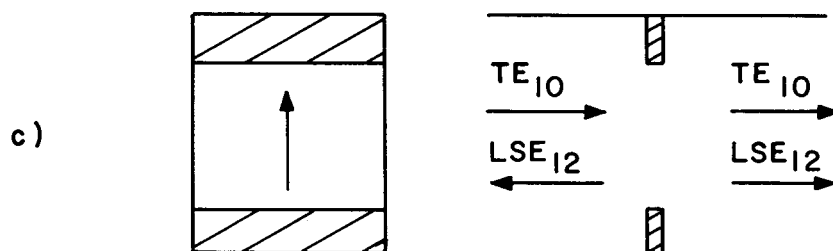
REACTIVE IRIS GENERATOR

d)
TE$_{10}$ →   TE$_{10}$ + LSE$_{12}$ →
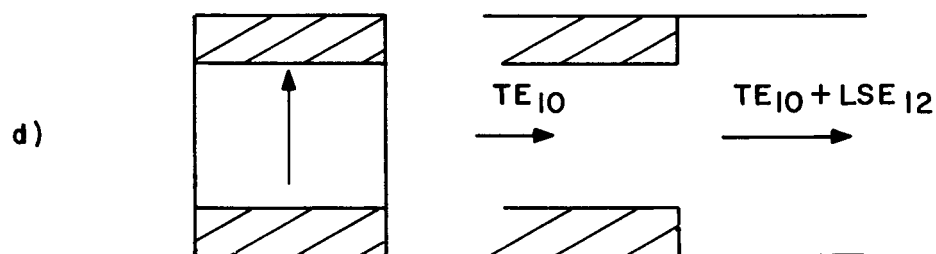
STEP GENERATOR

Figure 9.   LSE$_{12}$ Mode Generating Structures

Bisection of a waveguide propagating a TE_{10} and LSE_{12} mode by introduction of a thin conducting wall normal to the electric field does not affect the mode propagation characteristics. As can be seen in Figure 10(a) two half-sized waveguides result with each propagating a TE_{10} and LSE_{11} mode combination. The adjacent LSE_{11} modes are anti-phased. The bisection property is useful when considering a sectoral horn with large aspect ratio (b/a). A supporting center wall may be incorporated as shown in Figure 10(b) to reduce fabrication tolerance difficulties. The equivalence of an LSE_{11} mode pair to an LSE_{12} mode can also be obtained by a pair of sectoral horns each propagating a TE_{10}, LSE_{11} mode combination arranged as shown in Figure 10(c). This technique allows the use of shorter individual horns for the same bandwidth. The sectoral horn designs to be discussed later utilize the bisection property and provide for generation of the TE_{10} and LSE_{11} modes. Analysis of multimode performance is unaffected by this choice of modes.

Generation of the LSE_{11} mode in rectangular waveguide is accomplished by providing a single step discontinuity as shown in Figure 11. This discontinuity will launch odd modes (n = odd integer). TE_{10} and LSE_{11} propagation only is insured by having the output waveguide cut off all modes with $n \geq 3$.

When mode generation is accomplished at a step in rectangular waveguide and a flared horn termination is utilized, unwanted higher-order mode generation at the horn throat may be suppressed if the flare angle is not severe. The horn throat serves as a transition from rectangular waveguide to the sectoral horn. The mode electric field configurations in the sectoral horn are represented by modes with cylindrical wavefronts centered at the horn vertex.

Mode generation can be accomplished in the horn itself thereby eliminating the possible undesirable effect of a horn throat. This technique of cylindrical mode generation is practical when the mode phase difference from the generator to the horn aperture can be made correct for the modes involved, with the mode generator located in the region of the horn, which will support TE_{10} and LSE_{11} or LSE_{12} modes only. The

(a)

SPLIT-HORN
LINE SOURCE

(b)

DUAL - HORN
LINE SOURCE
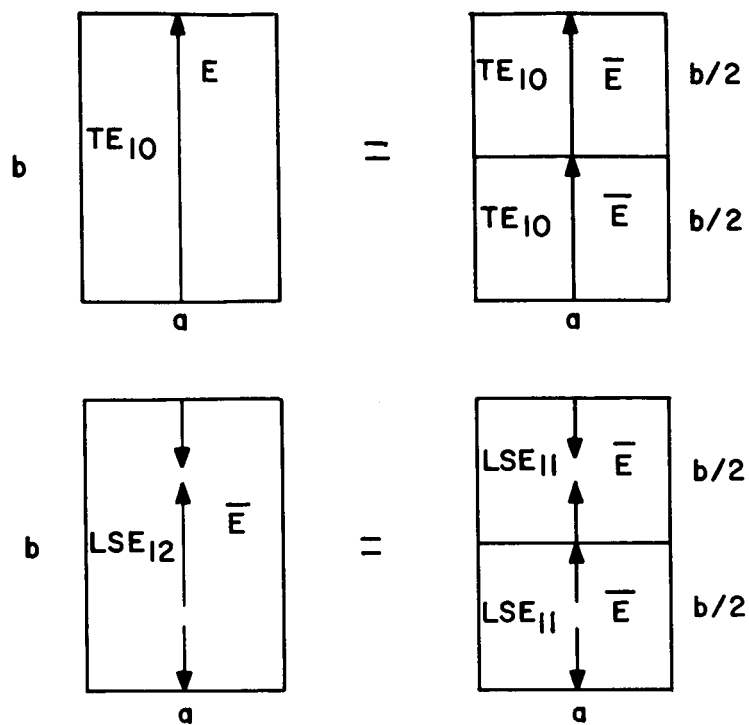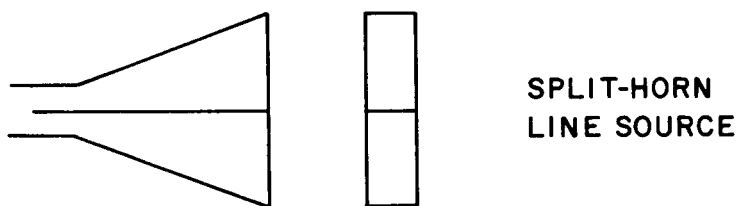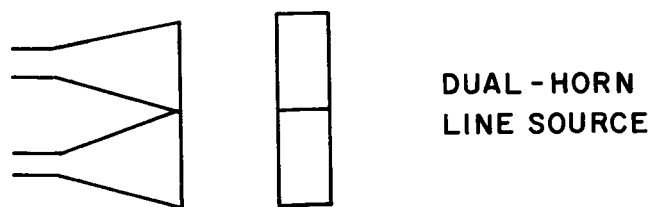
(c)

Figure 10.   Bisection of a Multimode Waveguide
Normal to $\overline{E}$

12

cylindrical mode generator is shown in Figures 12(a) and (b) for LSE_{12} and LSE_{11} mode generation respectively.
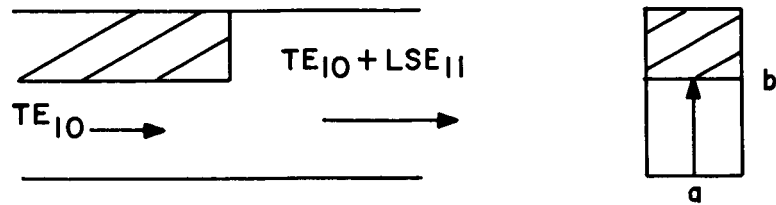
Figure 11. LSE_{11} Mode Generation in Rectangular Waveguide
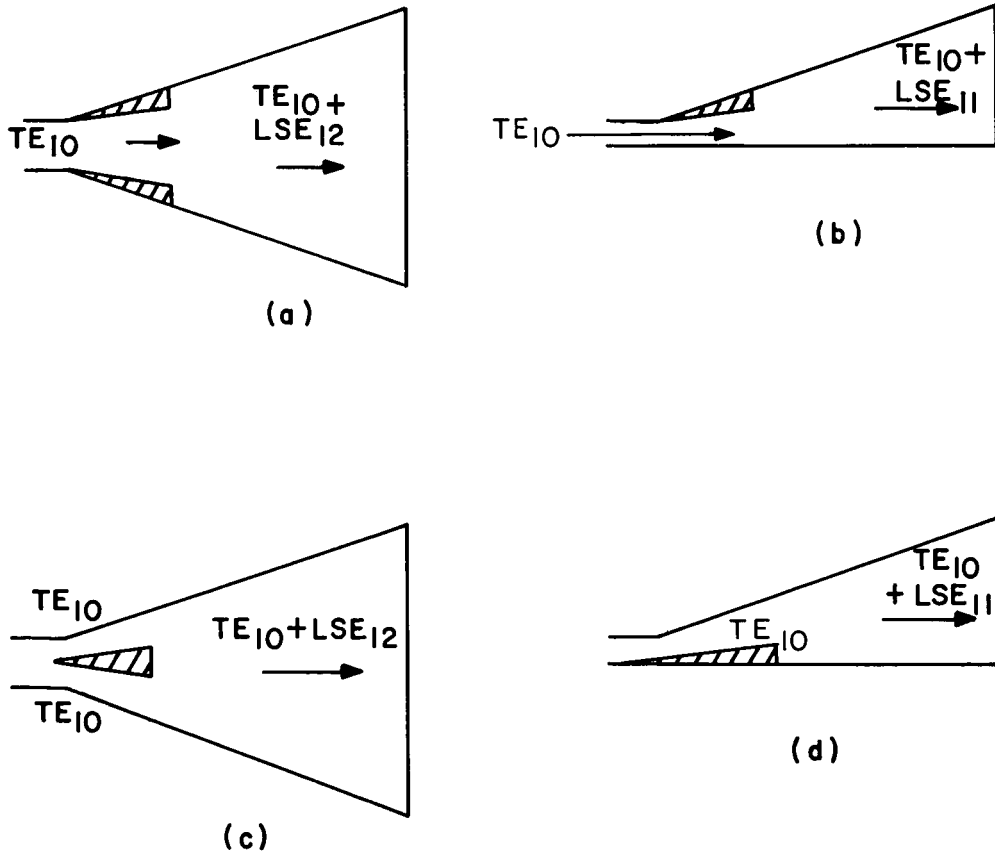
Figure 12. LSE_{11} Cylindrical Mode Launcher Configurations

The phase of the LSE_{12} mode at the plane of generation can be changed 180 degrees by providing the mode generating step at the center of the guide as shown in Figure 12(c) rather than at the edge as shown in Figure 12(a). The phase of the LSE_{11} mode at the plane of generation is changed 180 degrees by incorporating the mode generating step on the opposite wall as shown in Figure 12(d).

The choice of using LSE_{12} or LSE_{11} mode generation is usually determined solely by the horn geometry. The mode generator type selected is usually that which provides maximum bandwidth.

DESIGN DATA FOR MULTIMODE SECTORAL HORNS

The radiation characteristics of a multimode horn are dependent on the relative amplitude and phase of the modes involved. The design of a multimode horn to produce specific pattern beamwidth and sidelobe characteristics over some bandwidth requires a knowledge of the relationships between these parameters and the physical geometry of the mode generating and propagating structures.

As previously mentioned, the large-aperture multimode sectoral horn requires a lens to correct the inherent flared horn phase curvature. The lens also influences the radiation pattern and bandwidth of the multimode horn.

The basic data necessary for the design of a multimode sectoral horn-lens radiator will be presented in this section. Mode amplitude ratio and relative mode phase difference will be related to the horn geometry. Lens design considerations and the effect on pattern characteristics will be discussed. Computed multimode line source patterns including all the previous effects will be shown.

Mode Phase Difference

The electric and magnetic field components in an E-plane sectoral horn are derived from the radial waveguide configuration (Ref. 5) shown in Figure 13. The

rectangular waveguide TE_{10}, LSE_{11} and LSE_{12} mode equivalents in the sectoral horn waveguide are the H_{10}, H_{11} and H_{12} radial waveguide modes. The expression for the radiating transverse aperture field component, E_ϕ, of an H_{mn} sectoral horn mode is

$$E_{\phi_{mn}} = f(r) \sin \frac{n\pi}{b} Z \cos \frac{m\pi}{\Phi} \phi \tag{4}$$

The cutoff wavelength of the H_{mn} sectoral horn mode is

$$\lambda_{c_{mn}} = \frac{1}{\sqrt{\left(\frac{n}{2b}\right)^2 + \left(\frac{m}{2r\Phi}\right)^2}} \tag{5}$$

The transmission line behavior of an outwardly propagating H-type mode is expressed in terms of the Hankel function $H_m^{(2)}(Kr)$. In the asymptotic form of these functions for Kr large the Hankel function becomes (Ref. 6)

$$H_m^{(2)}(Kr) \approx \left(\frac{2}{\pi Kr}\right)^{1/2} e^{-j\left(Kr - \frac{2n+1}{4}\pi\right)} \tag{6}$$
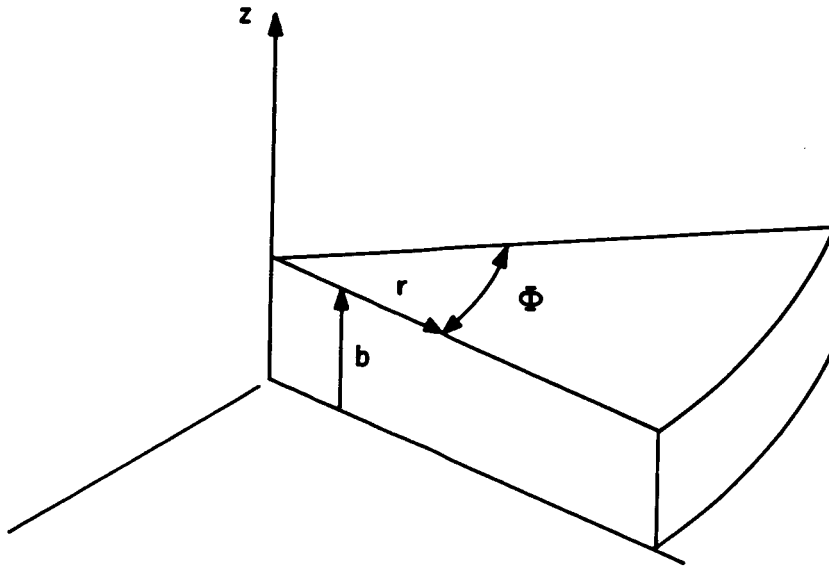
Figure 13. Radial Waveguide Coordinate System

where

$$K = \frac{2\pi}{\lambda_g}$$

The above expression represents a wave travelling in the direction of increasing r. The solution in sectoral waveguide for Kr large corresponds to a wave propagating along the longitudinal axis of a rectangular waveguide. The assumption is made, for simplicity of analysis, that Kr is large in the multimode region of the sectoral horn. This assumption is valid for a large portion of this region.

With the assumption that Kr is large, the guide wavelength for the H_{mn} sectoral horn mode can now be defined as

$$\lambda_{g_{mn}} = \frac{\lambda \lambda_{c_{mn}}}{\sqrt{\lambda_{c_{mn}}^2 - \lambda^2}} \tag{7}$$

and the phase difference between the H_{10} and H_{mn} modes through a section of sectoral horn waveguide can be determined. From equations (7) and (5)

$$\lambda_{g_{mn}} = \frac{2 r \Phi a \lambda}{\sqrt{(2r\Phi a)^2 - (mr\Phi\lambda)^2 - (na\lambda)^2}} \tag{8}$$

The incremental phase shift to the H_{mn} mode through a section Δr of a sectoral horn is

$$\Delta \ominus_{mn_s} = \frac{2\pi \Delta r}{\lambda_{g_{mn}}} \tag{9}$$

The total phase shift to the H_{mn} mode through a section of a sectoral horn from $r = R_o$ to $r = R$ is

$$\ominus_{mn_s} = 2\pi \int_{R_o}^{R} \frac{dr}{\lambda_{g_{mn}}} \tag{10}$$

16

Using equation (8) in equation (10) and integrating the following expression for $\bigodot_{mn_s}$, the phase shift of the mn^{th} mode, is obtained

$$\bigodot_{mn_s} = \frac{\pi}{\Phi} \left\{ \left[k_2^2 (4a_\lambda^2 - m^2) - n^2 \right]^{1/2} - n \tan^{-1} \frac{\left[k_2^2 (4a_\lambda^2 - m^2) - n^2 \right]^{1/2}}{n} \right. $$

$$\left. - \left[k_1^2 (4a_\lambda^2 - m^2) - n^2 \right]^{1/2} + n \tan^{-1} \frac{\left[k_1^2 (4a_\lambda^2 - m^2) - n^2 \right]^{1/2}}{n} \right\} \qquad (11)$$

where

$$k_2 = \frac{R_\lambda \Phi}{a_\lambda} \quad ; \quad k_1 = \frac{R_{o_\lambda} \Phi}{a_\lambda}$$

and

$$a_\lambda = \frac{a}{\lambda} \quad ; \quad R_\lambda = \frac{R}{\lambda} \quad ; \quad R_{o_\lambda} = \frac{R_o}{\lambda}$$

The phase difference between the H_{10} and H_{11} modes from the mode generator to the radiating aperture of the sectoral horn $(R_o - R)$ is a critical parameter in its design. As shown in Figure 7, the optimum low sidelobe line source design results when the H_{10} and H_{11} modes are in phase at the aperture center. Phase differences between these modes results in pattern degradation. The phase difference between two sectoral horn modes, $\bigodot_{MN_s}$, is

$$\bigodot_{MN_s} = \bigodot_{m_M n_{N_s}} - \bigodot_{M_N n_{N_s}}$$

$$\bigodot_{MN_s} = \left[\frac{180°}{\pi} A_{2_M} - A_{1_M} + n_M \tan^{-1} \frac{A_{1_M}}{n_M} - n_M \tan^{-1} \frac{A_{2_M}}{n_M} \right. \qquad (12)$$

$$\left. - A_{2_N} + A_{1_N} - n_N \tan^{-1} \frac{A_{1_N}}{n_N} + n_N \tan^{-1} \frac{A_{2_N}}{n_N} \right] \text{ degrees}$$

17

where

$$A_{i_M} = \left[k_i^2 (4a_\lambda^2 - m_M^2) - n_M^2 \right]^{1/2}$$

$$A_{i_N} = \left[k_i^2 (4a_\lambda^2 - m_N^2) - n_N^2 \right]^{1/2}$$

m_M, n_M = mode indices of Mth mode

m_N, n_N = mode indices of Nth mode

$$k_1 = \frac{R_{o_\lambda} \Phi}{a_\lambda} \quad ; \quad k_2 = \frac{R_\lambda \Phi}{a_\lambda}$$

$\widetilde{\bigcirc}_{MN_s}$ as seen in (12) is frequency dependent.

The multimode line source design procedure requires adjustment of $(R_o - R)$ to provide a phase differential of $360° n$ (where n = an integer) between the H_{10} and H_{11} modes at the horn aperture at a single design frequency. For low sidelobe considerations a phase difference of $\pm 25°$ is tolerable (maximum sidelobe below -25 dB) which determines an upper and lower band edge frequency.

The quantity $\dfrac{\widetilde{\bigcirc}_{MN_s} \Phi_r}{180}$ is plotted vs k_2 with k_1 as a parameter in Figures 14(a) and (b) for H_{10} and H_{11} mode propagation in a sectoral horn. The parameter k_1 in Figure 14 is $1.02 \, k_{co_{11}}$ where $k_{co_{11}}$ is the cut-off aspect ratio for the H_{11} mode.

In general

$$k_{co_{mn}} = \frac{n}{(4a_\lambda^2 - m^2)^{1/2}} \tag{13}$$

18
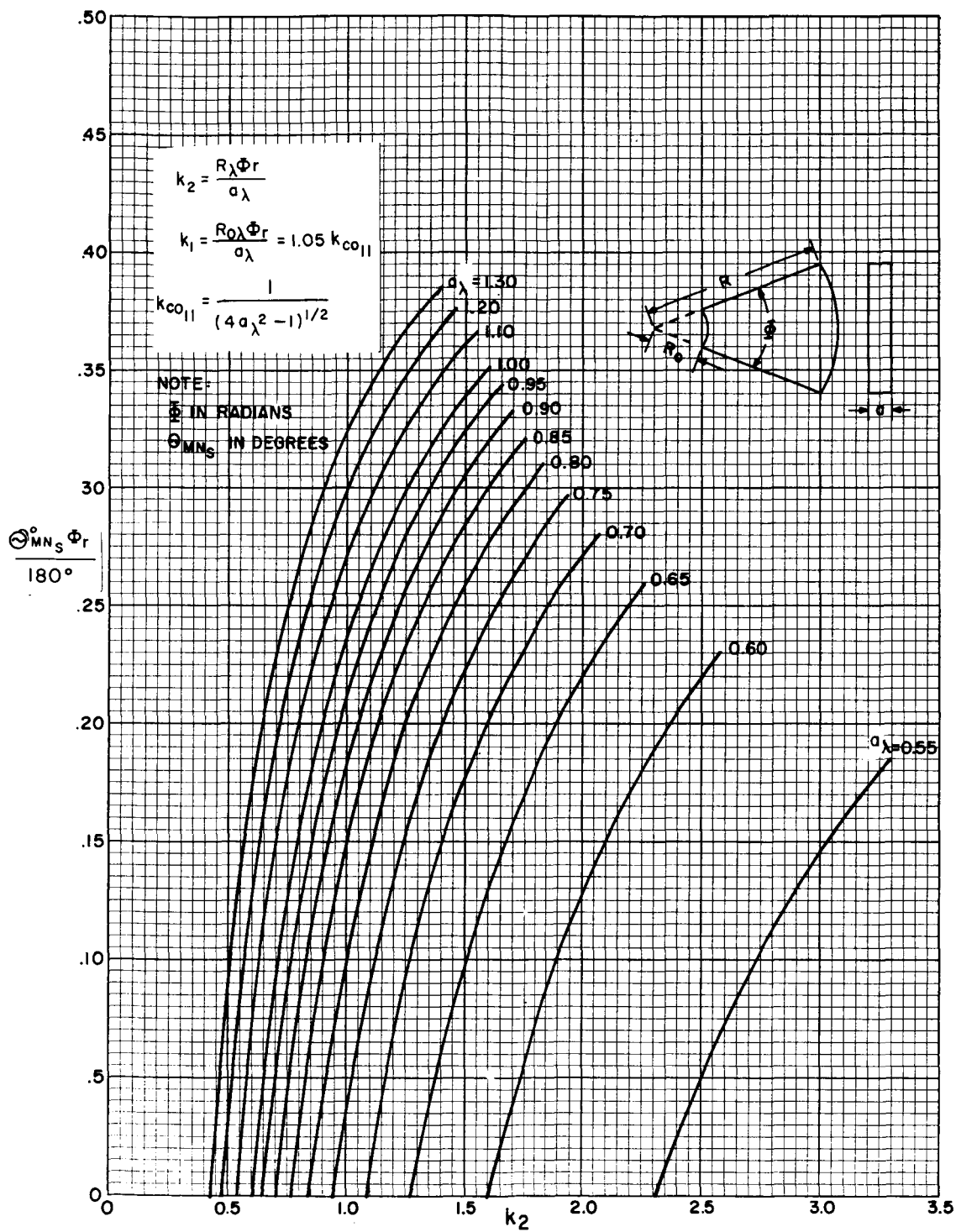
Figure 14(a). Design Curves for E-Plane Sectoral Horn with H_{10} and H_{11} Mode Utilization
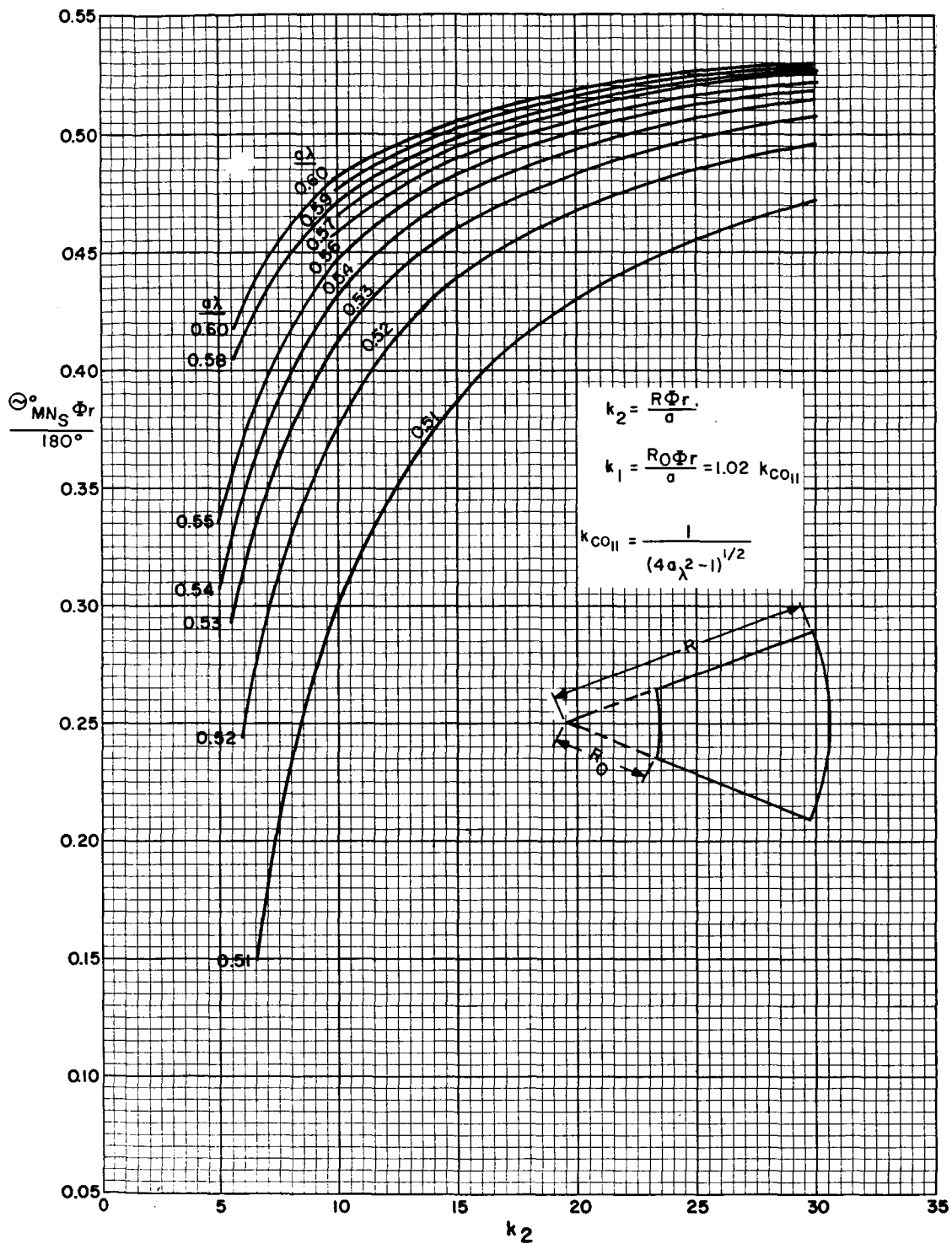
Figure 14(b). Design Curves for E-Plane Sectoral Horn with H_{10} and H_{11} Mode Utilization

and

$$k_{co_{11}} = \frac{1}{(4a_\lambda^2 - 1)^{1/2}}$$

The curves in Figure 14 permit determination of $\odot_{MN_S}$ if the horn flare angle Φ_r (radians), k_2 and k_1 are known.

A similar set of curves is plotted in Figure 15 (a) and (b) for H_{10} and H_{12} mode propagation. The cut-off aspect ratios $k_{co_{11}}$ and $k_{co_{12}}$ are plotted vs a_λ in Figure 16.

If mode generation is provided in a rectangular waveguide which in turn excites the sectoral horn, the phase difference between the dominant and higher mode in the rectangular waveguide section must be recognized. The phase difference between two modes propagating through a length "l" of rectangular waveguide is

$$\odot_{MN_R} = 360° \, l \left[\frac{1}{\lambda g_{m_M n_M}} - \frac{1}{\lambda g_{m_N n_N}} \right] \text{ degrees} \qquad (14)$$

$\lambda g_{11}/\lambda$ and $\lambda g_{12}/\lambda$ are plotted vs k_R ($k_R = b/a$) with a_λ as a parameter in Figures 17(a) and (b). For the case where rectangular waveguide mode generation is employed the total phase difference between modes is

$$\odot_{MN_{TOTAL}} = \odot_{MN_R} + \odot_{MN_S}$$

Mode Amplitude Ratio

The ratio of H_{11} mode amplitude to H_{10} mode amplitude provided by the sectoral-horn single-step mode-generating geometry of Figures 12 (b) and 12 (d) can be determined by equating the input and output transverse electric field at the plane of generation in terms of Fourier series components. The mode amplitudes are then the Fourier series coefficients. The results obtained from this analysis can be modified

The graph shows the vertical axis labeled $\dfrac{\Theta^{\circ}_{MN_S}\Phi_r}{180^{\circ}}$ ranging from 0 to 0.5, and the horizontal axis labeled k_2 ranging from 0 to 7.0.

Curves labeled: $a_\lambda = 1.00$, 0.95, 0.90, 0.85, 0.80, 0.75, 0.70, 0.65, 0.60, and $a_\lambda = 0.55$.

Inset equations:

$$k_2 = \frac{R\lambda\Phi_r}{a_\lambda}$$

$$k_1 = \frac{R_0\lambda\Phi_r}{a_\lambda} = 1.05\, k_{CO_{12}}$$

$$k_{CO_{12}} = \frac{2}{(4a_\lambda^2 - 1)^{1/2}}$$
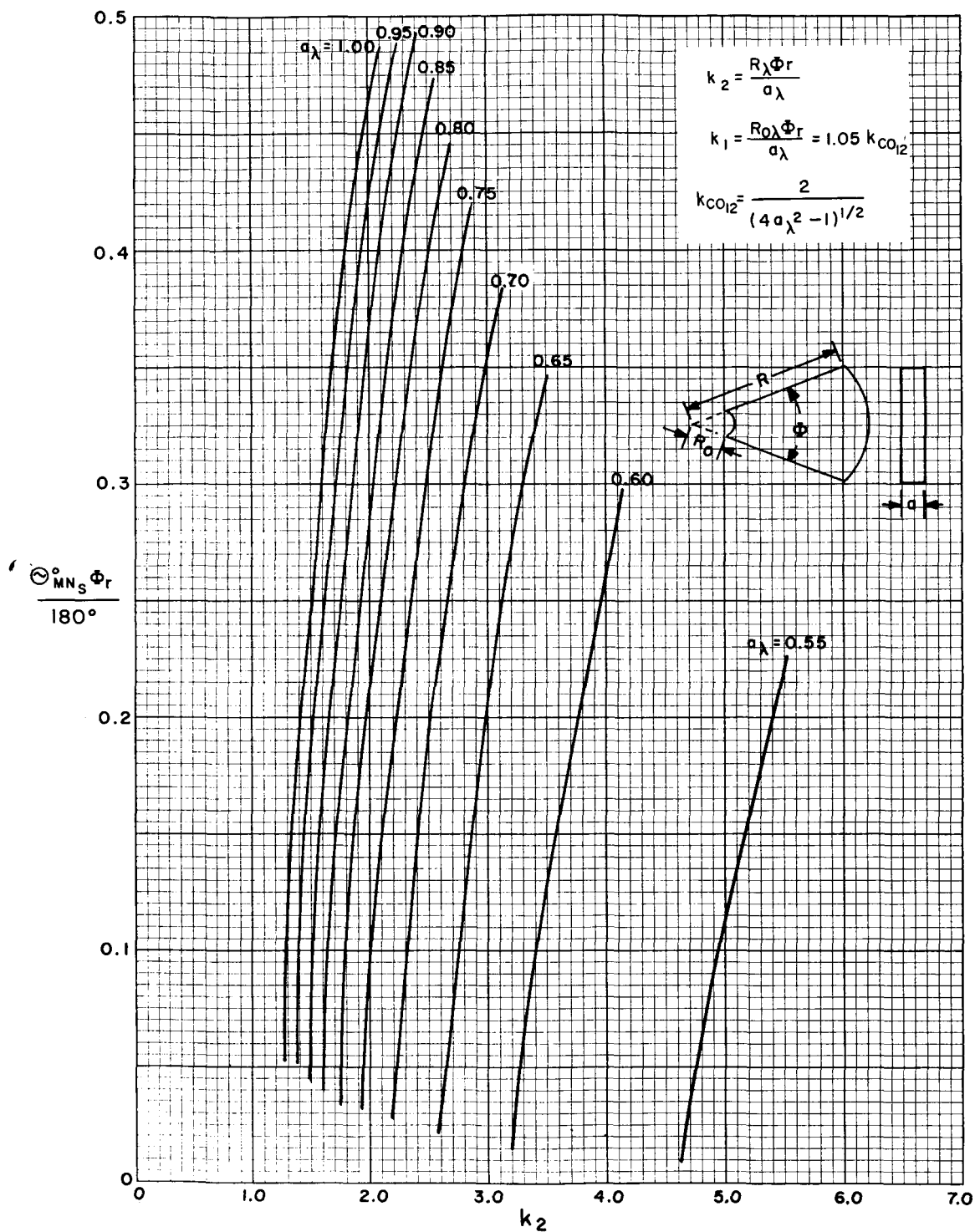
Figure 15(a). Design Curves for E-Plane Sectoral Horn with H_{10} and H_{12} Mode Utilization

22

$$k_2 = \frac{R\lambda \Phi r}{a\lambda}$$

$$k_1 = \frac{R_0\lambda \Phi r}{a\lambda} = 1.05\, k_{CO_{12}}$$

$$k_{CO_{12}} = \frac{2}{(4a_\lambda^2 - 1)^{1/2}}$$

$a\lambda = 1.00$
0.95
0.90
0.85
0.80
0.75
0.70
0.65
0.60

$a\lambda = 0.55$

$\dfrac{\Theta^\circ_{MN_S}\Phi r}{180^\circ}$

k_2
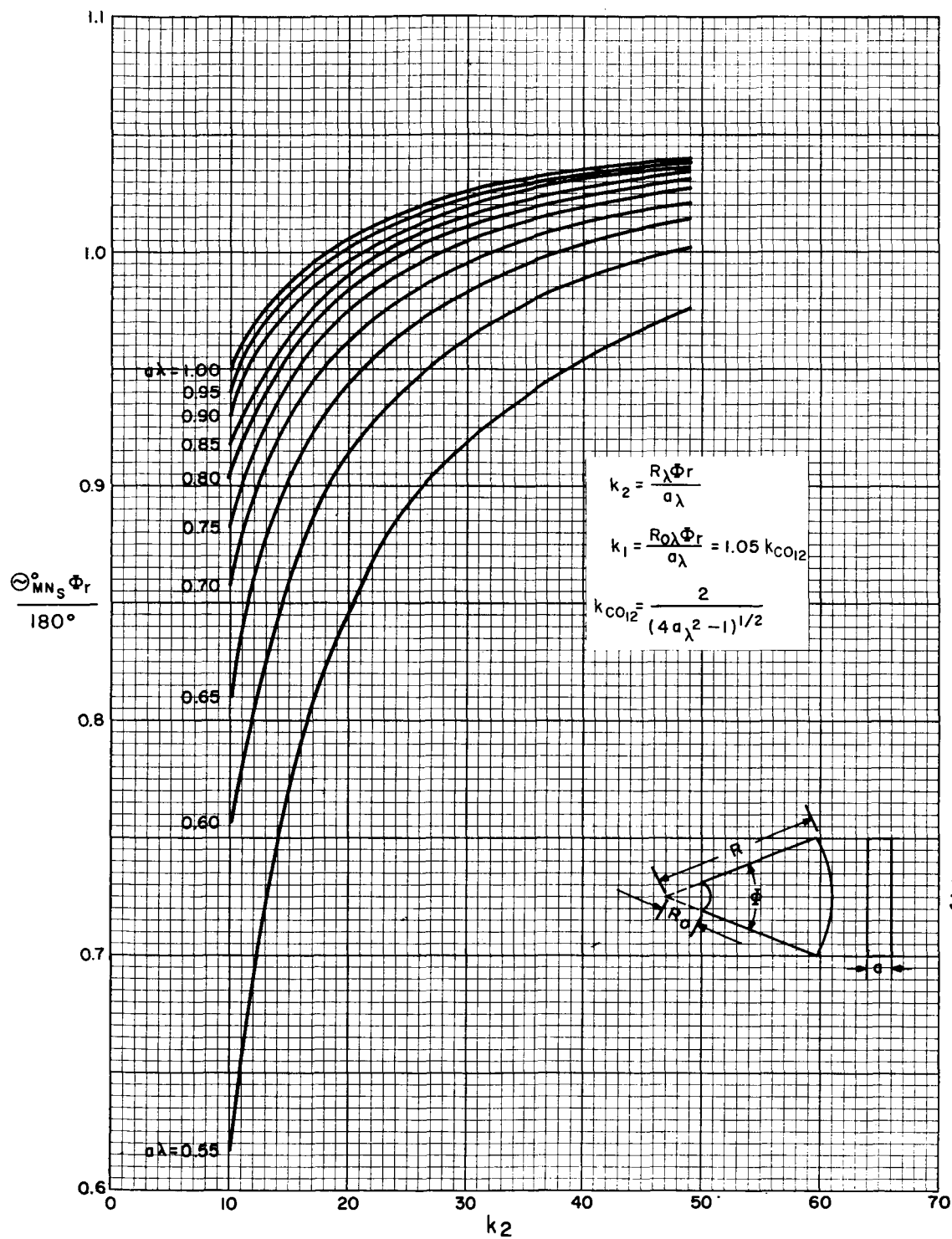
Figure 15(b). Design Curves for E-Plane Sectoral Horn with H_{10} and H_{12} Mode Utilization

The figure contains the equation:

$$k_{co_{mn}} = \frac{n}{(4a_\lambda^2 - m^2)^{1/2}} = \frac{b}{a} \text{ AT CUT-OFF OF } H_{mn} \text{ MODE}$$

REGION OF LSE$_{11}$ MODE PROPAGATION

REGION OF LSE$_{12}$ MODE PROPAGATION
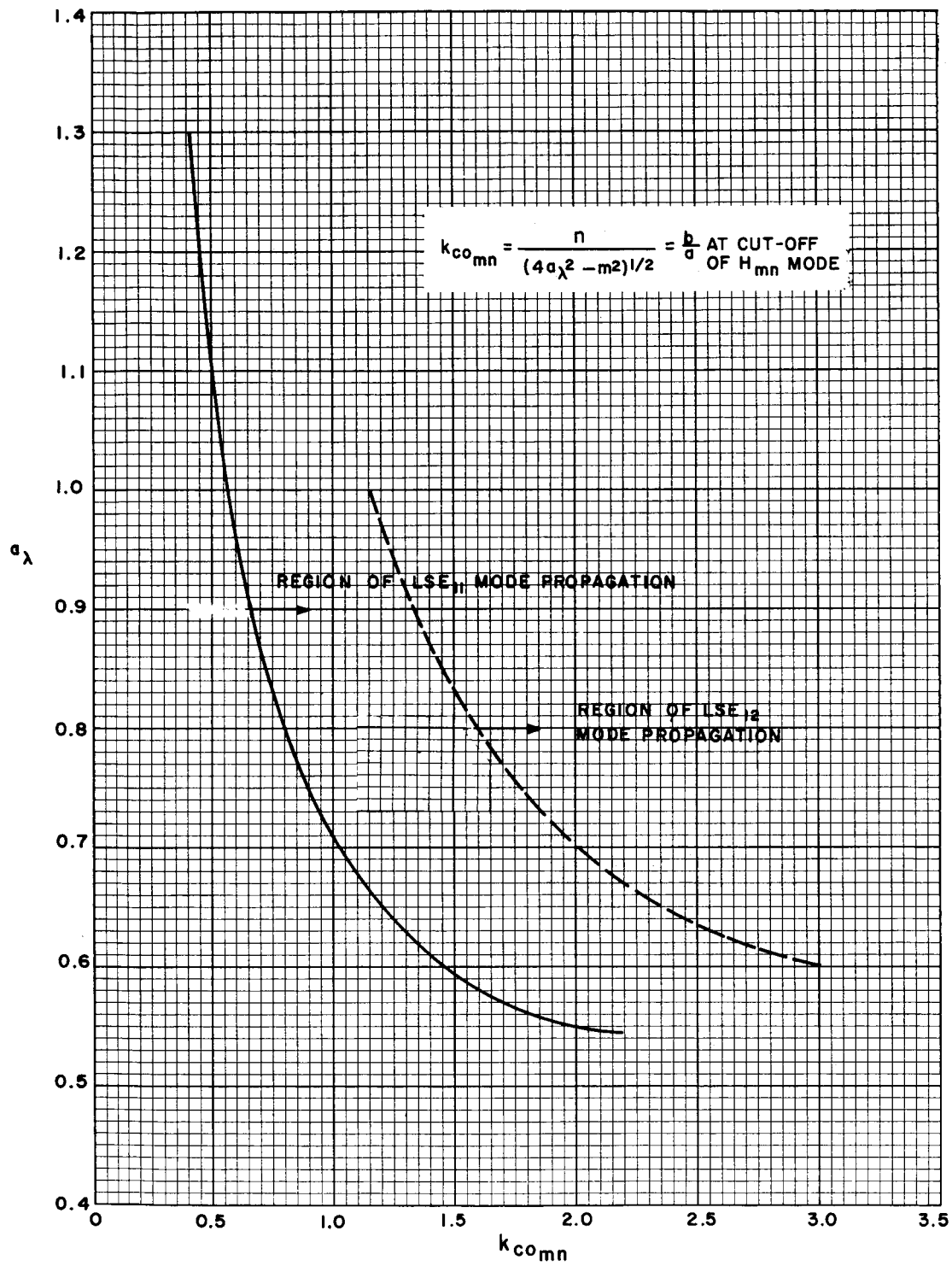
Figure 16. a_λ vs Cutoff Aspect Ratio for Rectangular Waveguide

Figure 17(a). Normalized Guide Wavelength vs Aspect
Ratio for Rectangular Waveguide
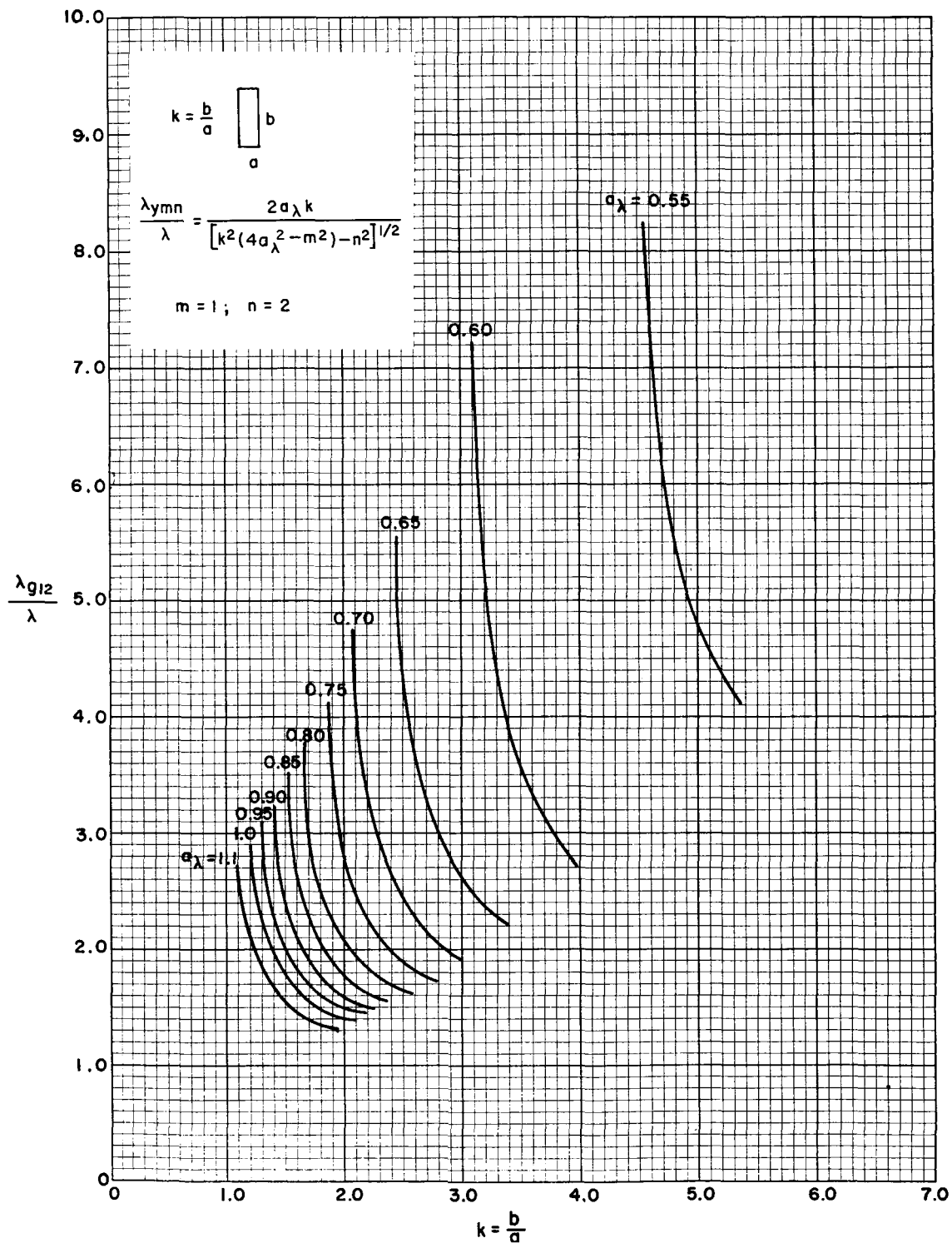
Figure 17(b).   Normalized Guide Wavelength vs Aspect
Ratio for Rectangular Waveguide

to relate H_{12} mode amplitude to H_{10} mode amplitude for the geometry in Figures 12 (a) and 12 (c) and both LSE_{11} and LSE_{12} mode generation to the rectangular waveguide geometry of Figures 11 and 9 (d).

Consider the waveguide geometry in Figure 18 as propagating and supporting only an H_{10} mode in the region $r < c$ and being large enough to support H_{11} mode propagation in the region $r > c$. At the cylindrical surface of discontinuity, $r = c$, the field is just that of the H_{10} mode in the smaller section since all tangential electric field components on the step must be zero.

Then

$$E_\phi(o, o, z) = \cos \frac{\pi z}{a}$$

$$E_\phi(o, \phi, o) = 1 \qquad\qquad -\delta/2 \leq \phi \leq (-\delta/2 + \delta') \tag{15}$$

$$E_\phi(o, \phi, o) = 0 \qquad\qquad (-\delta/2 + \delta') \leq \phi \leq \delta/2$$
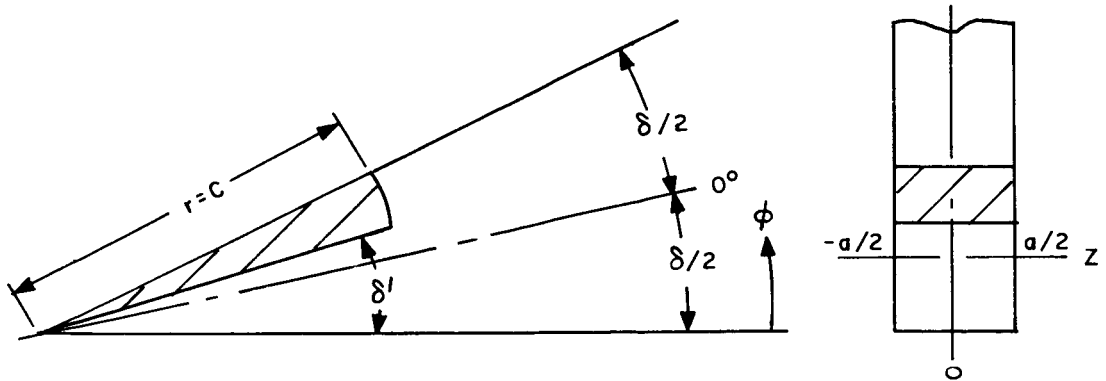
Figure 18. H_{11} Mode Sectoral Horn Geometry

In the larger horn section, for $r > c$, the field may be written as

$$E_{\phi_2}(r, \phi, z) = a_{10} \cos\left(\frac{\pi z}{a}\right) e^{-jK_{10}(r-c)} + a_{11} \cos\left(\frac{\pi z}{a}\right)\sin\left(\frac{\pi\phi}{\delta}\right) e^{-jK_{11}(r-c)} \tag{16}$$

which is the sum of an H_{10} and H_{11} mode generated in phase with amplitudes a_{10} and a_{11} and propagation constants K_{10} and K_{11} respectively. All higher order modes are assumed to be cut off in this section.

At $r = c$

$$E_{\phi_1} (\phi, c) = E_{\phi_2} (\phi, c)$$

$$\quad (17)$$

$$E_{\phi_1} (\phi, c) = a_{10} + a_{11} \cdot \sin \left(\frac{\pi \phi}{\delta} \right)$$

The above represents the first two terms of the Fourier series expansion of $E_\phi (\phi, C)$. The mode amplitudes, which are the Fourier coefficients are

$$a_{10} = \frac{1}{2\pi} \int_{-\delta/2}^{(-\delta/2 + \delta')} d\phi = \frac{\delta'}{2\pi} \quad (18)$$

$$a_{11} = \frac{1}{\pi} \int_{-\delta/2}^{(\delta/2 + \delta')} \sin \left(\frac{\pi \phi}{\delta} \right) d\phi = -\frac{\delta}{\pi^2} \sin \frac{\pi \delta'}{\delta} \quad (19)$$

The mode amplitude ratio is then

$$\frac{a_{11}}{a_{10}} = - \frac{2 \sin \left(\pi \frac{\delta'}{\delta} \right)}{\pi \delta'/\delta} \quad (20)$$

The above equation is identical, except for sign, to that obtained for the mode generating geometry of Figure 19. For rectangular waveguide mode generation in the geometries of Figure 20, δ and δ' in (20) are replaced by b and b' respectively.

The mode amplitude ratio a_{11}/a_{10} from equation (20) is plotted against step ratio δ'/δ in Figure 21. This curve is generally used to determine the mode generating step geometry when the desired mode amplitude ratio is known.

28

Figure 19. H_{12} Mode Sectoral Horn Geometry

LSE$_{11}$ GEN.

LSE$_{12}$ GEN.

Figure 20.   Rectangular Waveguide Mode
Generating Geometries
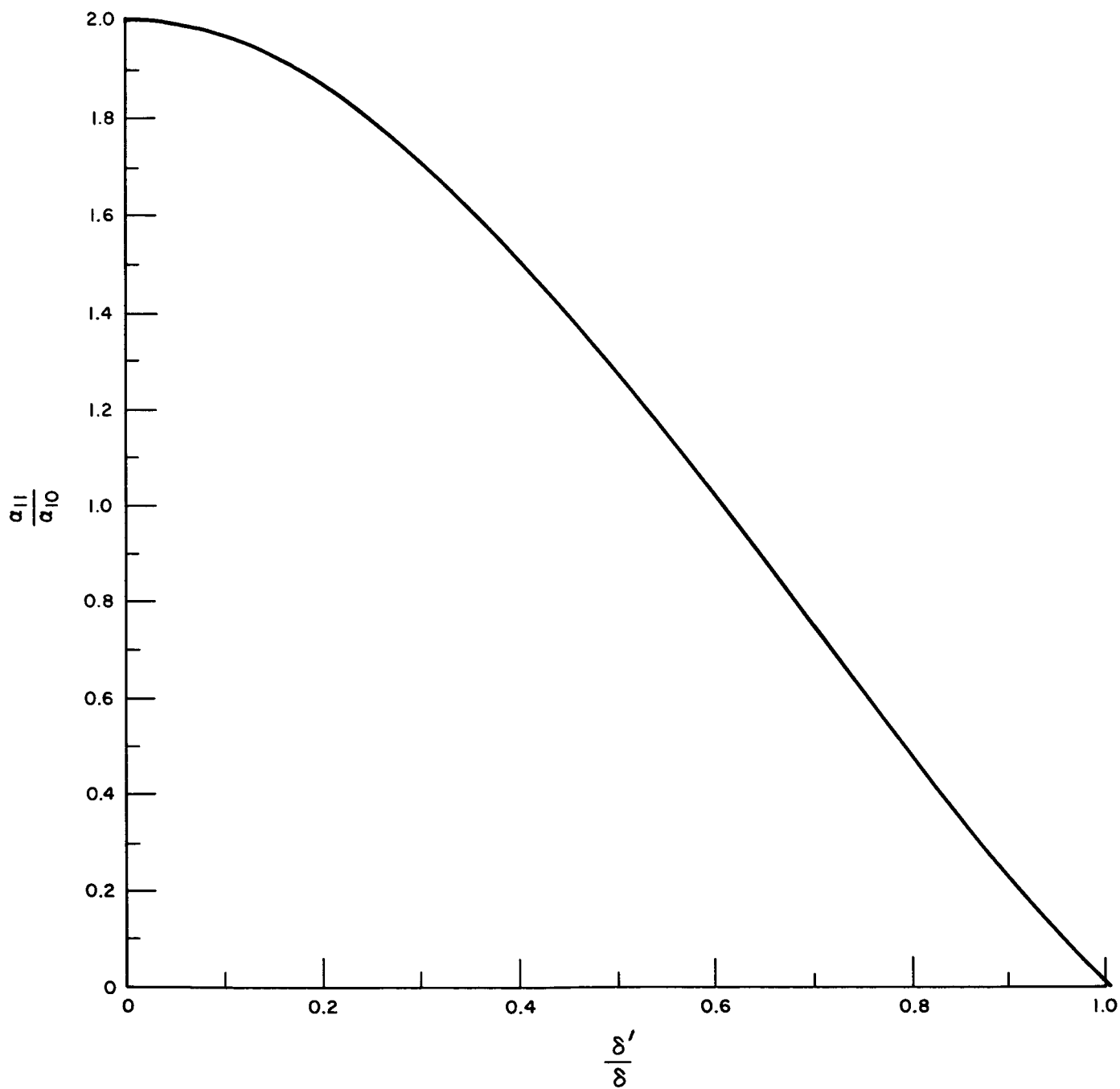
Figure 21. Mode Amplitude Ratio a_{11}/a_{12} vs Cylindrical Mode
Generator Step Ratio δ'/δ

LENS DESIGN CONSIDERATIONS

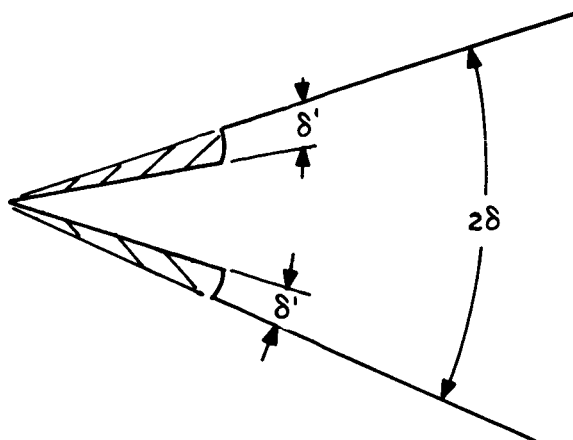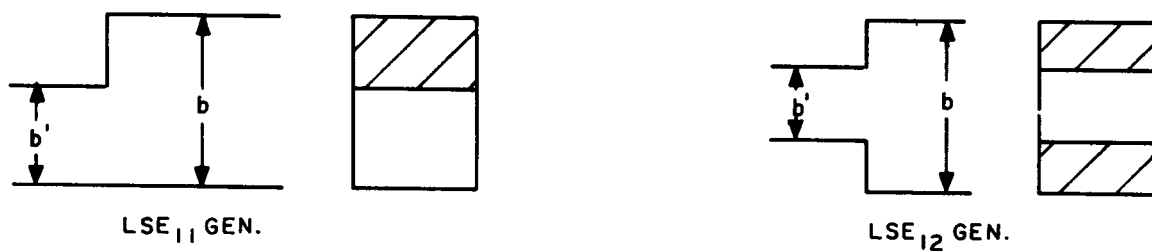The multimode sectoral horn requires a cylindrical aperture lens as shown in Figure 22 if the horn focal length to aperture ratio (f/d) is to be kept small. The lens design must convert both the dominant H_{10} and higher order H_{11} cylindrical waves to plane waves at the horn aperture. The normalized cutoff wavelength $\lambda_{c_{mn}}/a$ is plotted vs k (where $k = r\Phi/a$ in the sectoral horn or b/a in rectangular waveguide) in Figure 23 for H_{10}, H_{11} and H_{12} modes. The normalized cutoff wavelength of the H_{11} and H_{12} modes asymptotically approaches the normalized cutoff wavelength of the H_{10} mode as k is increased. For narrow-beamwidth horns where k is large at the horn aperture, $\lambda_{c_{10}}$, $\lambda_{c_{11}}$ and $\lambda_{c_{12}}$ will be essentially equal. The guide wavelengths $\lambda_{g_{10}}$, $\lambda_{g_{11}}$ and $\lambda_{g_{12}}$ will also be essentially equal so that a simple dominant mode lens design can be employed. For the multimode sectoral horns studied, k was greater than 14 where H_{10} and H_{11} modes were utilized.

Two basic lens designs exist. These are classified by the index of refraction "n", which is defined as the ratio of the wavelength in the propagating structure preceding the lens λ_{g_1} to the wavelength in the lens medium λ_{g_2}. The index of refraction is either greater or less than 1.

The lens designs considered for the multimode line source utilized a single refracting surface only. This restriction was imposed to simplify impedance matching at the sectoral horn aperture. The cylindrical lens equation for the single refracting surface lens in Figure 22 is

$$R = L + n (R \cos \theta - L) \tag{21}$$

in polar coordinates and

$$x = \frac{L}{n+1} \left\{ \left[1 + \frac{y^2 (n+1)}{L^2 (n-1)} \right]^{\frac{1}{2}} - 1 \right\} \tag{22}$$

in Cartesian coordinates.
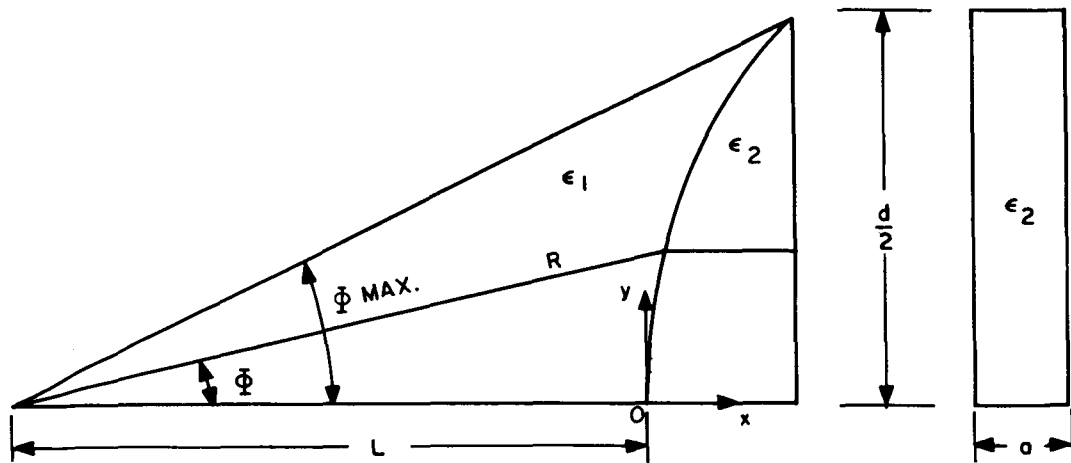
Figure 22. Horn-Lens Geometry

In a bounded medium, n is frequency dependent. The lens design procedure then requires an exact lens design at a specified frequency and an evaluation of bandwidth effects.

The phase deviation from uniform at the lens planar surface is

$$\Delta \phi = \frac{360°}{\lambda_{g_1}} \left[R - L - n \left(R \cos \Phi - L \right) \right] \quad \text{degrees} \tag{23}$$

The aperture phase distribution produced at some frequency other than the design frequency is quadratic. The maximum phase error occurs at the lens edge and is found by substituting R_{max} for R in (23).

Zoned lenses were also considered but discarded due to sidelobe producing aperture shadowing at the zone boundaries.

The lens shape also influences the aperture amplitude distribution of the multimode line source. For the single refracting surface cylindrical lens, the aperture distribution tapering effect of the lens alone is (Ref. 7)

$$T(y) = \left[\frac{(n \cos \Phi - 1)^2}{(n - 1)(n - \cos \Phi)} \right]^{\frac{1}{2}} = L \left[\frac{1}{(L + nx) \left[L + x (n + 1) \right]} \right]^{\frac{1}{2}} \tag{24}$$

32
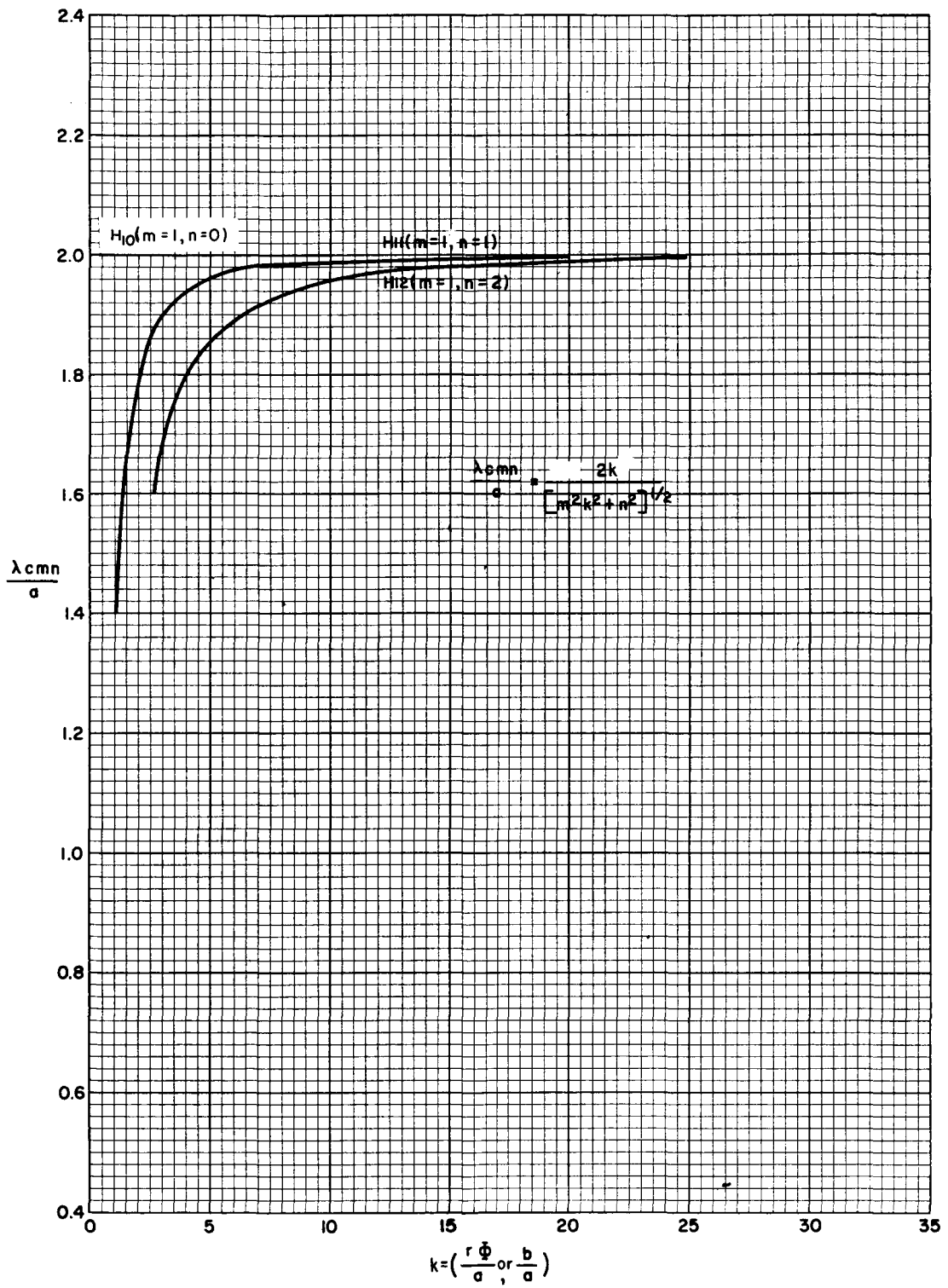
Figure 23. Normalized H_{11} and H_{12} Mode Cutoff Wavelength vs K for Sectoral Horn

33

For the case of a multimode horn-lens radiator where n > 1, the lens acts to decrease the illumination at the aperture edge and does not cause any increase in sidelobe levels. When n < 1, the effect is reversed and may result in a composite distribution with a central "dimple". This effect increases alternate sidelobe levels, which is undesirable in a low-sidelobe multimode horn design. For this reason and bandwidth advantages, a dielectric lens with n > 1 was chosen for the experimental models. The dielectric material chosen for the lens is Emerson and Cuming Stycast 0005 (polystyrene) with a measured dielectric constant of 2.55 at K_u band and loss tangent less than .0005.

## Lens Impedance Matching Considerations

The cylindrical dielectric lens chosen for the multimode sectoral horn is characterized by reflection losses at both the refracting and planar surfaces. The reflection coefficient produced at the refracting surface is a function of the angle of incidence and therefore affects the intended aperture distribution differently at different aperture locations. The incident rays on the planar surface are essentially normal to that surface so that its reflection coefficient is constant at any point in the aperture.

Surface reflections for a dielectric lens with ϵ_r = 2.55 will have a pronounced effect on the radiation pattern characteristics. The low sidelobe levels required of the multimode line source would be difficult to obtain, if at all possible. For this reason the lens surface reflection coefficients must be reduced by incorporation of suitable impedance matching devices.

A simple method of obtaining a good surface impedance match utilizes a quarter-wave transformer section on both the refractive and planar surfaces of the lens as shown in Figure 24.

An impedance match is obtained when the quarter-wave surface layer produces a waveguide impedance Z_2 defined by

$$Z_2 = \sqrt{Z_1 Z_3} \tag{25}$$

34
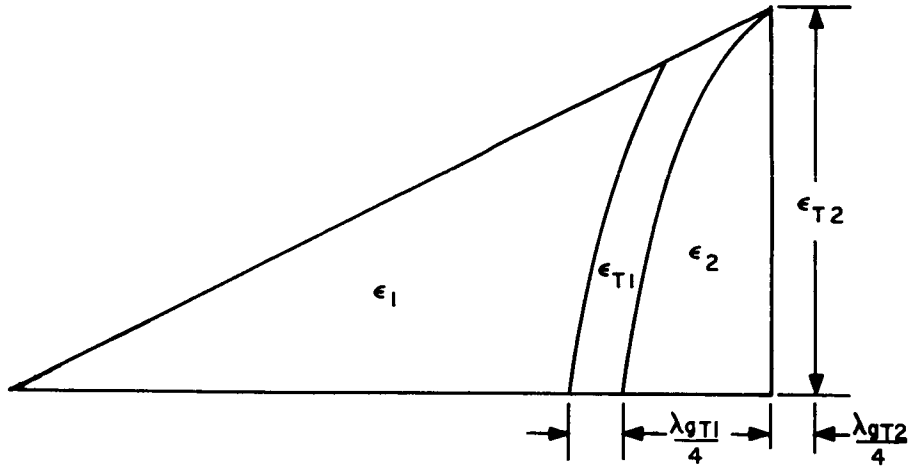
Figure 24. Lens Matching with Quarter-Wave Transformers

where

Z_1 = unloaded waveguide impedance

Z_3 = impedance of waveguide completely filled with dielectric.

Waveguide characteristic impedance is defined as

$$Z = \eta \frac{K}{\beta}$$ (26)

where

$$\eta = \sqrt{\frac{\mu_o}{\epsilon_o}} = 377 \, \Omega$$

$$K = \frac{2\pi}{\lambda} ; \quad \beta = \frac{2\pi}{\lambda_g}$$

λ = free space wavelength

λ_g = guide wavelength in waveguide filled medium

The intermediate characteristic impedance Z_2 may be obtained by choosing a dielectric material for the transformer section with dielectric constant ϵ_{r2} between ϵ_{r1} and ϵ_{r3}. An impedance transformer can be designed for the planar surface using the above techniques. A more practical solution for the transformer utilizes the lens dielectric material in a partially filled waveguide configuration. Two quarter-wave

35

dielectric matching structures in waveguide are shown in Figure 25. By adjusting the thickness of the "tongue" or "groove" in Figures 25 (a) and (b) respectively, Z_2 can be varied between Z_1 and Z_3. This technique can be used to match both the refractive and planar lens surfaces.
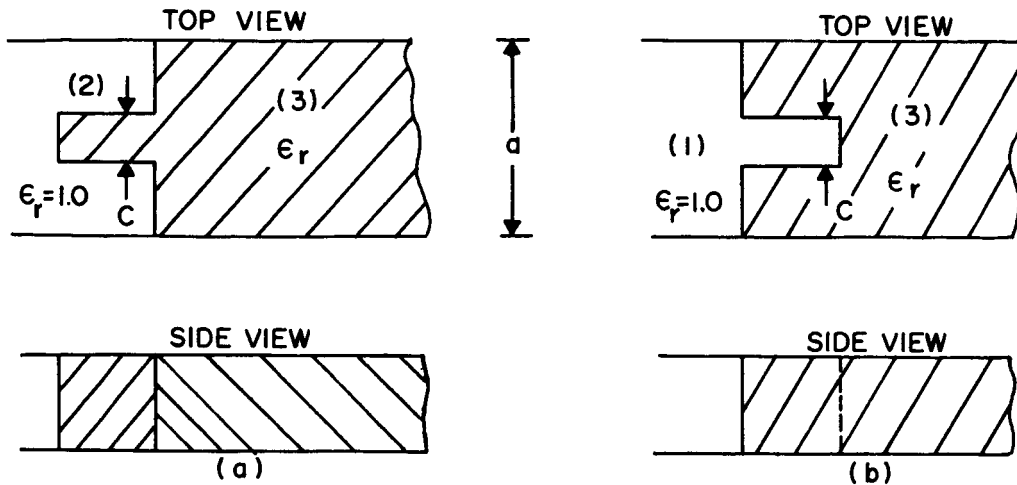
Figure 25. Quarter-Wave Dielectric Matching Structures

The properties of slab-dielectric-loaded waveguides are analyzed in the literature (Ref. 8). Z_2 can be determined for the waveguide configurations in Figure 25 as a function of dielectric constant, slab width "c", waveguide width "a" and frequency. Guide wavelength in the slab-loaded waveguide λ_{g2} is also determined from the same parameters. Hence the slab width and guide wavelength can be determined for a required Z_2 in a given waveguide geometry.

Multimode Line Source Pattern Computation

A computer program was written for the IBM 7090 to calculate the pattern of a hypothetical line source with a multimode illumination function. For the case where lens effects are neglected the resulting pattern characteristics of mode amplitude and

phase effects are identical to those in Figure 7. This, however, is an incomplete representation of actual multimode line source performance. A more complete representation is obtained by including lens amplitude, phase and loss effects.

The pattern of the continuous aperture multimode line source including the previously mentioned effects was obtained by dividing the line source into a finite array of Huygens sources, incorporating the mode and lens influence on the Huygens source pattern and vectorially summing the contributions of all such sources over the entire length of the line source.

The complete expression for the pattern of the line source geometry in Figure 26 is

$$E(\theta)_{db} = 20 \log_{10} \left[\left| \frac{F_1 + j F_2}{F_1{}' + j F_2{}'} \right| \left(\frac{1 + \cos \theta}{2} \right) \right] \qquad (27)$$

where

$$F_1 = \left\{ 2 \sum_{y=m}^{\ell/2} T(y) \left[A \cos \xi + B \cos \left(\frac{2\pi y}{\ell} \right) \cos \left(\alpha_M + \xi \right) \right] \frac{V_y}{V_o} \cos \left(\frac{2\pi y}{\lambda} \sin \theta \right) \right.$$
$$\left. + T(0) \left[A \cos \xi + B \cos \left(\alpha_M + \xi \right) \right] \right.$$

$$F_2 = \left\{ 2 \sum_{y=m}^{\ell/2} T(y) \left[A \sin \xi + B \cos \left(\frac{2\pi y}{\ell} \right) \sin \left(\alpha_M + \xi \right) \right] \frac{V_y}{V_o} \cos \left(\frac{2\pi y}{\ell} \sin \theta \right) \right.$$
$$\left. + T(0) \left[A \sin \xi + B \sin \left(\alpha_M + \xi \right) \right] \right.$$

$$F_1{}' = F_1 (\theta = 0)$$

$$F_2{}' = F_2 (\theta = 0)$$

$$T(y) = L \left[\frac{1}{(L + nx) \ [L + x (n + 1)]} \right]^{\frac{1}{2}} \qquad = \text{lens amplitude taper term}$$
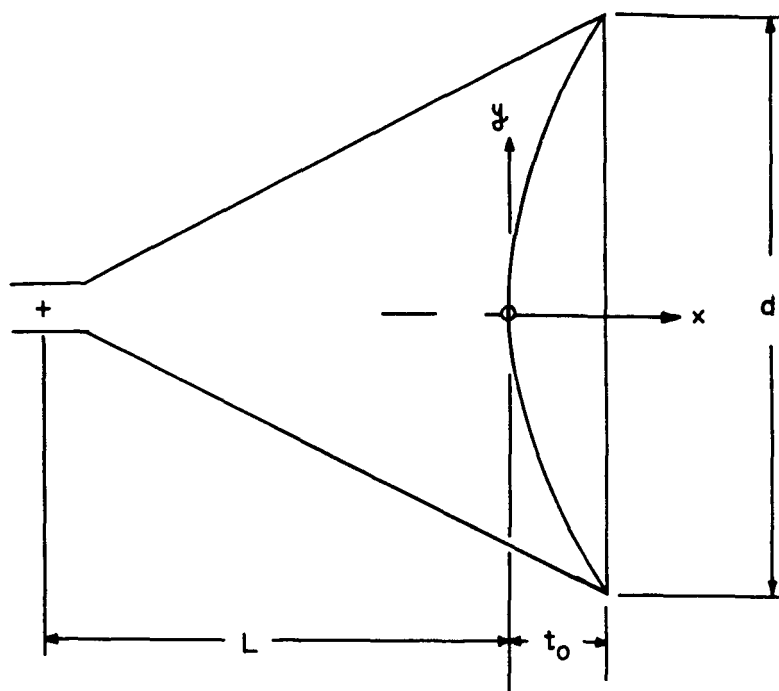
Figure 26. Horn Geometry for Pattern Computation

$$\xi = \frac{360°}{\lambda_{g_1}} (n_o - n)\, x \qquad\qquad = \text{lens phase error term}$$

$$\frac{V_y}{V_o} = 10^{3.47}\,\frac{n \tan \delta}{\lambda}\, (t_o - t) \qquad\qquad = \text{lens loss term}$$

$$B = a_{11}/a_{10}$$

α_M = mode phase difference at aperture

t_o = lens thickness at $y = 0$

t = lens thickness at $y = y$

Equation (27) was used to compute the patterns for the various multimode line source configurations investigated. The results of these computations will be discussed in the following section.

38

LINE SOURCES FOR TWO PROPOSED ARRAY DESIGNS

E-plane multimode sectoral horns can be arranged in an H-plane array to provide an H-plane electronic scan capability and array antenna patterns characterized by low sidelobes and high beam efficiency.

In consideration of the grating lobe problem, characteristic of most electronically scanned arrays, two array configurations requiring independent line source designs were studied and evaluated. The first, as shown in Figure 27 (a) utilizes two staggered arrays of half horns for the purpose of eliminating grating lobes in the scan plane. The second, a more conventional parallel array of restricted-width horns shown in Figure 27 (b) provides an element-to-element separation consistent with the scan requirement. Configurations studied were compatible with a scan capability of ±30 degrees to ±60 degrees and half-power beamwidth of 3 degrees.

The staggered array concept was later found to have grating lobes outside of the scan plane as shown in the Appendix A and was abandoned in favor of the parallel array.

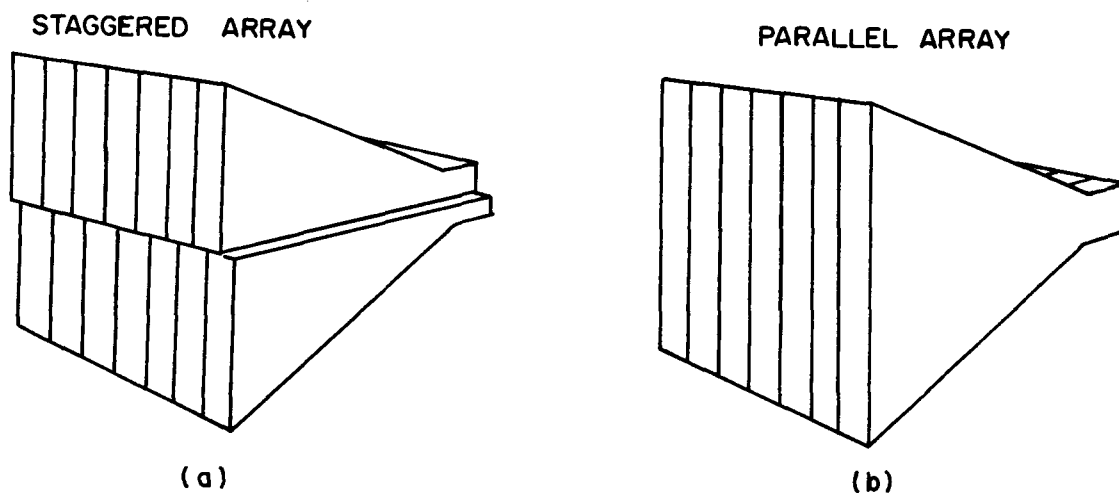STAGGERED ARRAY

PARALLEL ARRAY

(a)

(b)

Figure 27. H-Plane Arrays

Line Sources for the Staggered Array

An array of sectoral horns as shown in Figure 27 (a) can be designed to eliminate grating lobes in the scan plane for a wide range of scan angles. To provide a scan capability to $\pm\theta_m$ for this configuration, the spacing between adjacent line sources S_λ must satisfy the following relationship

$$S_\lambda \leq \frac{1}{1 + \sin \left| \theta_M \right|} \tag{29}$$

To provide a ±60 degree scan capability with no grating lobes in the scan plane

$$S_\lambda \leq 0.536$$

The inter-element spacing S_λ is

$$S_\lambda = \frac{a_\lambda + t_\lambda}{2} \tag{30}$$

where

a_λ = sectoral horn inside width

t_λ = wall thickness between adjacent elements.

To prevent H_{2n} mode generation in the horn, a_λ must be less than unity. Since a_λ is less than unity and t_λ very small, S_λ will satisfy equation (29).

The initial step in the design of a multimode line source for the staggered array configuration is determination of the line source dimensions.

The line source length "d" for the multimode horn in Figure 28 is determined by the half-power beamwidth requirement. For an optimum low-sidelobe multimode line source the half-power beamwidth is

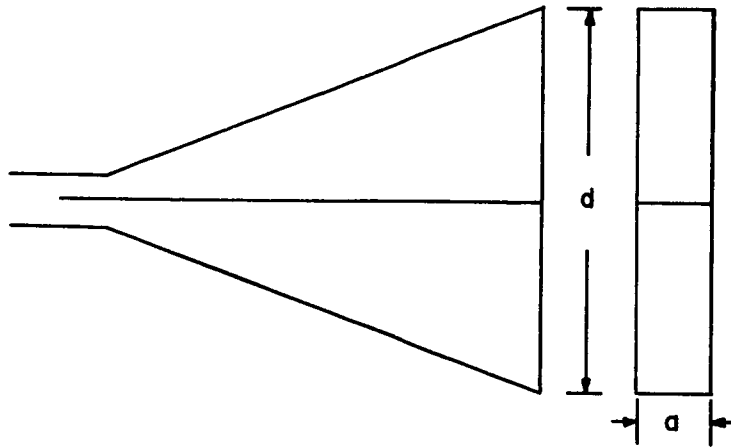$$HPBW = \frac{71\lambda}{d} \text{ degrees} \tag{31}$$

Figure 28.   Split Horn

For a 3-degree HPBW

$$d_\lambda = \frac{71}{3} = 23.7$$

At a design frequency of 16 GHz

$$d = 23.7 \ (0.738) = 17.5 \ \text{in.}$$

The width "a" was selected as 0.622 inches, which is the long inside dimension of standard K_u band (WR-62) waveguide. This dimension satisfies the requirements previously discussed and provides for ease of interfacing with standard K_u band test equipment.

Two line source designs were considered. These are the split-horn and dual-horn types pictured in Figure 10. The horn design for mode amplitude and phase considerations assumes a continuous aperture over the length d. Offsetting the half apertures as required in a staggered array, does not affect these considerations.

The mode generating step dimensions are common to both designs if horn input dimensions are constant. When a fixed horn input dimension is specified, as was done initially, mode generation is accomplished in the rectangular waveguide section feeding

the horn. Lengths of waveguide are incorporated between the mode generator and horn input to provide for adjustment of aperture mode phase difference α_M. A cross-section of a multimode horn employing this technique is shown in Figure 29.

To obtain an optimum mode amplitude ratio a_{11}/a_{10}, of 0.8, the ratio as determined from Figure 21 must be 0.68. Hence $b_p = 1.47\ b_f$. For a design based on a ±5% band-width centered about $f_o = 16$ GHz, $a_{\lambda_{HI}} = 0.887$ which is a_λ at the highest frequency. From Figure 16 it is found that $k_{co_{11}} = 0.67 = b_{f_{max}}/a$. To prevent propagation of higher order modes in b_f, $b_{f_{max_1}} = 0.417$ inches. Then $b_{p_{min}} = 1.47\ (0.417) = 0.614$ inches. The horn input dimension for this configuration was chosen to be $b_{p_{min}}$.
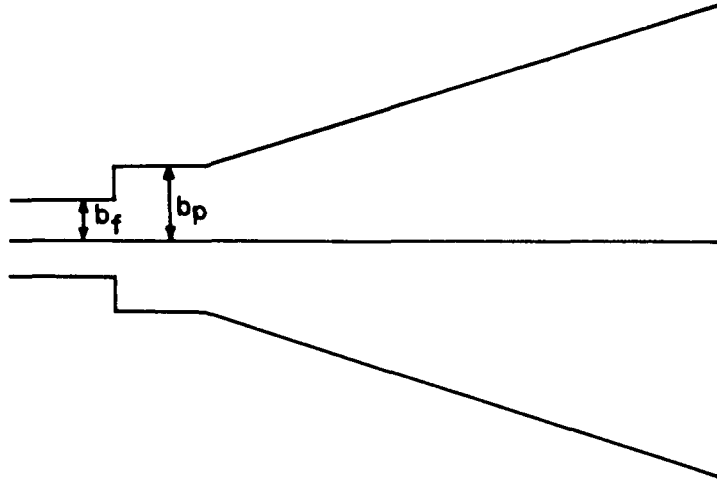

Figure 29. Multi-Mode Sectoral Horn with Rectangular Waveguide
Mode Generating and Phasing Structure

The optimum line source focal-length-to-aperture ratio was determined from analysis of computed multimode sectoral horn patterns. Line source patterns were computed for the sectoral horns previously discussed using equation (27) at a design frequency of 16 GHz ($\alpha_M = 0$) with horn flare angle Φ $\{ \Phi = \Phi\ (f/d) \}$ as a parameter. Curves of maximum sidelobe level vs focal length "f" are plotted in Figure 30 for both the split- and dual-horn types with $a_{11}/a_{10} = 0.8$, $\alpha_M = 0°$ and $20°$ and d = 17.5". Sidelobe levels of the single horn line source were relatively independent of f/d. For this reason a horn with f/d = 1.0 and a horn with f/d = 0.5 were considered.

42

Figure 30. Summary of Lens Effect on Multi-Mode Line Source
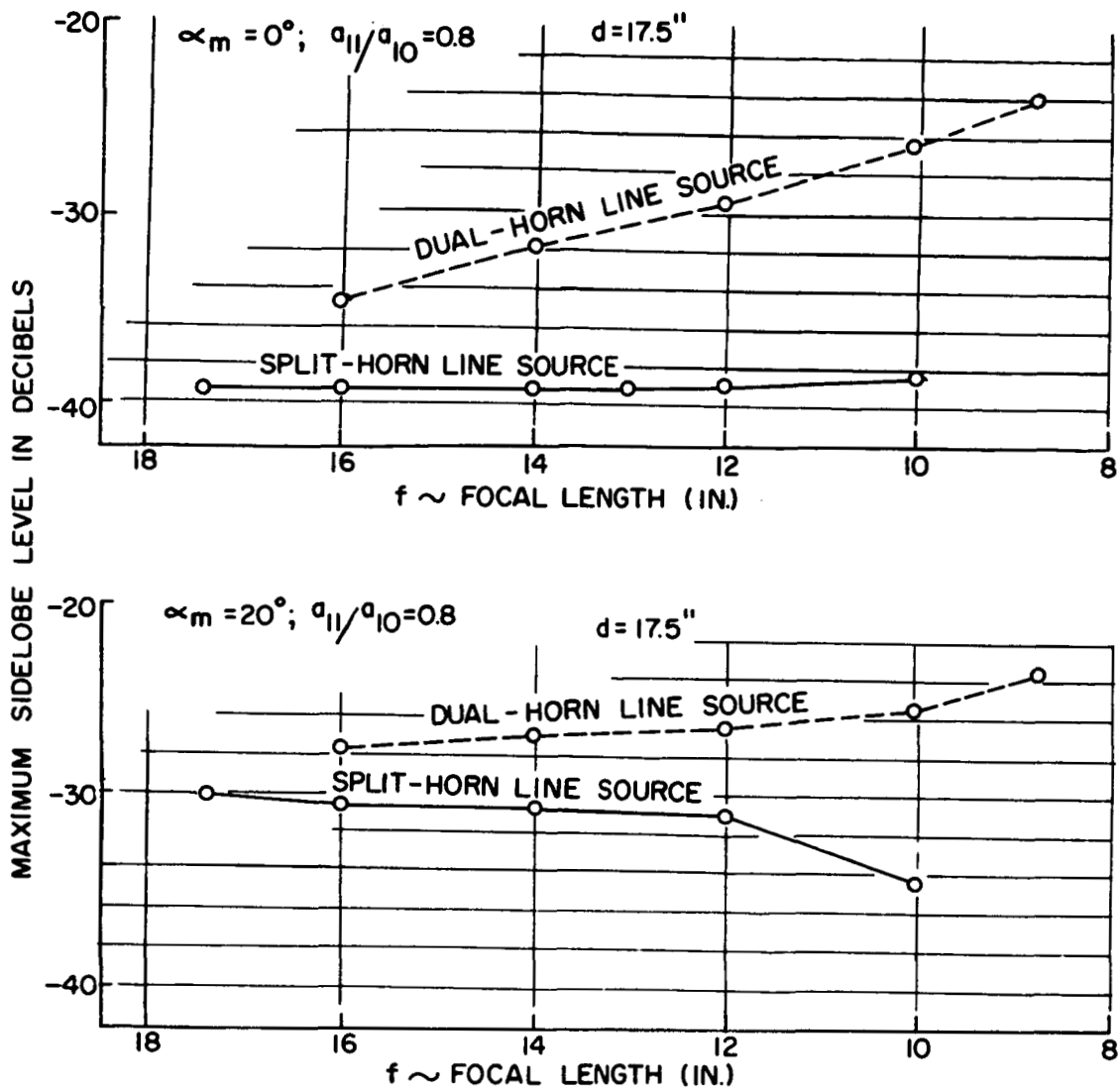Patterns (n > 1)

The dual-horn pattern maximum sidelobe level showed a definite dependence on f/d.
For the configurations considered, an f/d near unity gave best results and was considered for experimental model design.

Dimensions of the three horn configurations considered for the experimental model are given in Table I for the horn geometries shown in Figure 31.

TABLE I

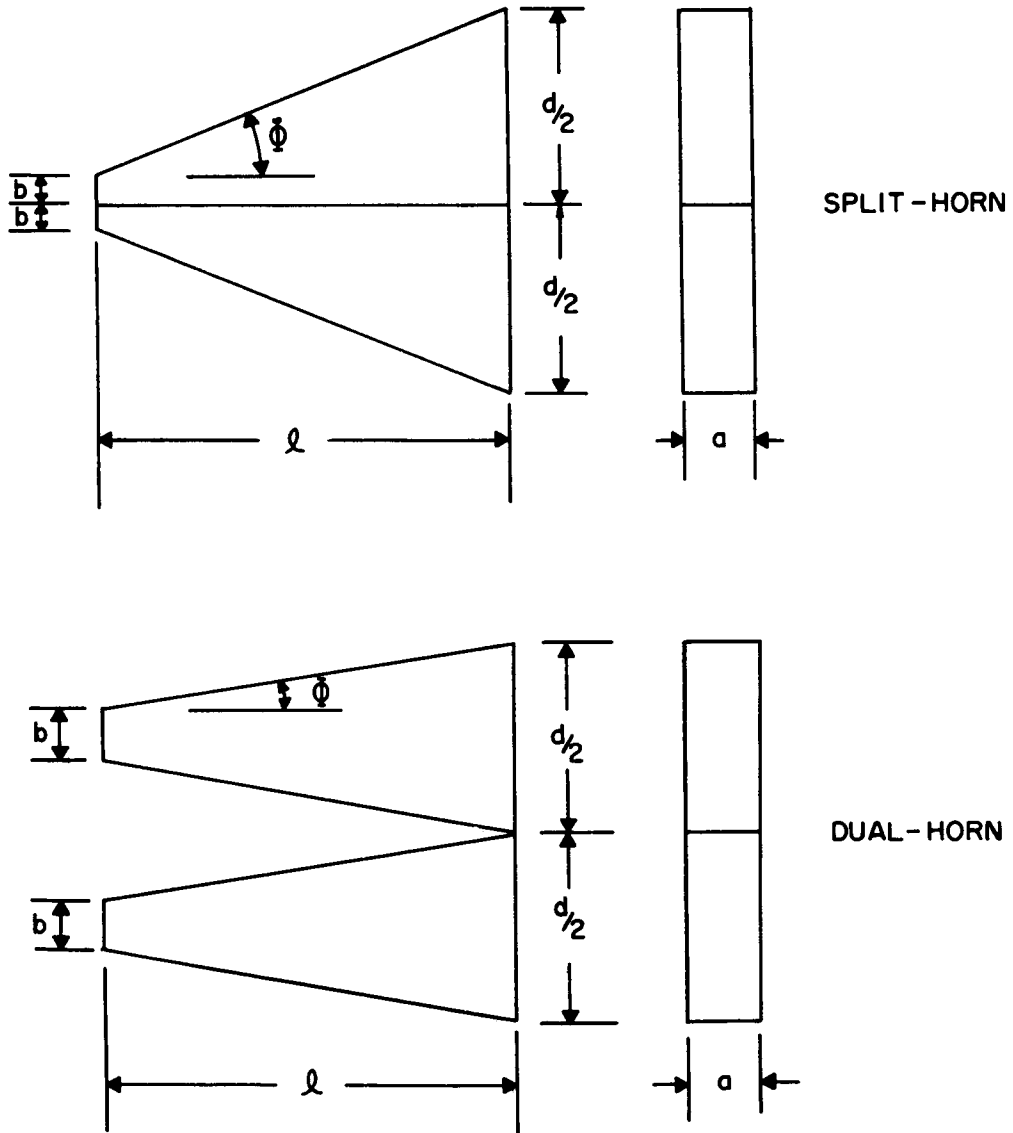| Line Source Type	Horn–Lens Model No.	f/d	d	b	ℓ	a	Φ
Single Horn	1	1.0	17.5"	.614"	16.25"	.622	26.6°
Single Horn	2	0.5	17.5"	.614"	8.13"	.622	45°
Dual Horn	3	0.93	17.5"	.614"	15.18"	.622	15°

Figure 31. Split-Horn and Dual-Horn Line Sources

The phase difference between the H_{10} and H_{11} modes and the lens phase errors are plotted vs frequency in Figure 32 for the horn geometries above. From these data the maximum value of α_m is determined and used in calculating line source patterns at the frequency band edge. The computed line source pattern characteristics at the band edge and center are given in Table II for the three configurations.

TABLE II

Horn-Lens No.	15.2 GHz		16.0 GHz		16.8 GHz	
	dBMax.S.L.	HPBW	dBMax.S.L.	HPBW	dBMax.S.L.	HPBW
1	29.3	3.3°	40.3	3.1°	30.7 dB	3.1°
2	32.3	4°	42.3	3.7°	33	3.3°
3	27.1	3.2°	33.9	3°	28.1	2.8°

The above pattern characteristics include lens amplitude tapering, phase error and loss. The three multimode horn configurations discussed above were fabricated for experimental evaluation.

Generation of the sectoral horn H_{10} and H_{11} modes by a discontinuity solely within the horn eliminates the need for an external rectangular waveguide mode generating and phasing structure. This technique of cylindrical H_{mn} mode generation is useful when the required mode phase difference at the horn aperture can be achieved without need for external phasing and H_{10} and H_{11} mode purity is retained.

Cylindrical mode generation was considered for horn number one since it satisfies the above requirements. The phase difference between the H_{10} and H_{11} modes for this configuration determines α_m and is plotted in Figure 33. The mode phase difference vs frequency response for cylindrical mode generation is essentially equal to that obtained from the horn configuration in Figure 29. In practice the cylindrical mode generating technique is desirable because it eliminates the rectangular waveguide sectoral horn junction discontinuity which gives rise to unwanted mode generation.
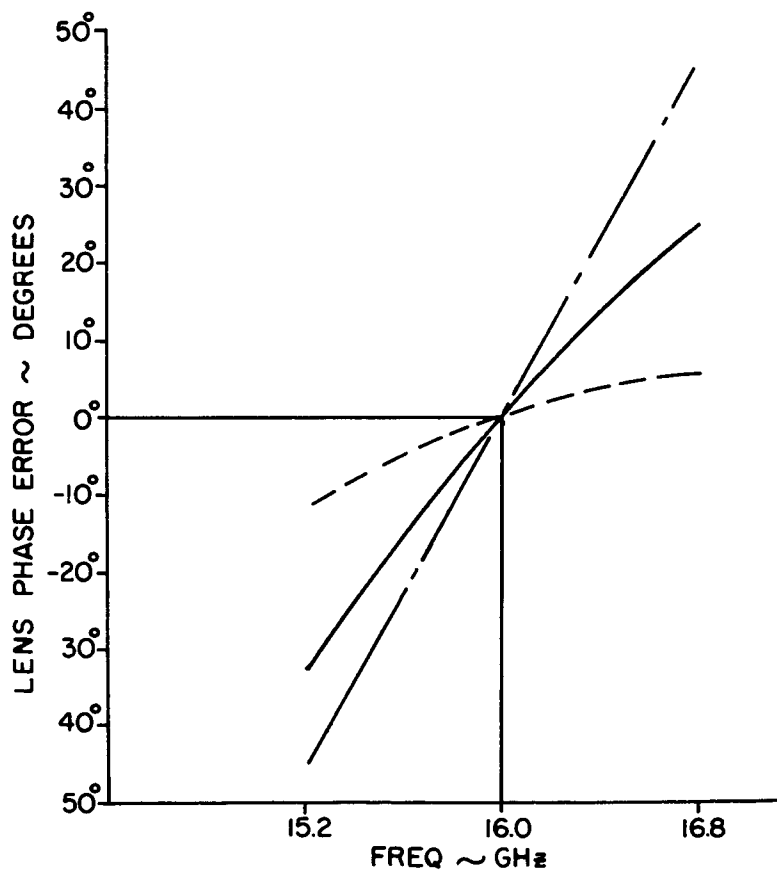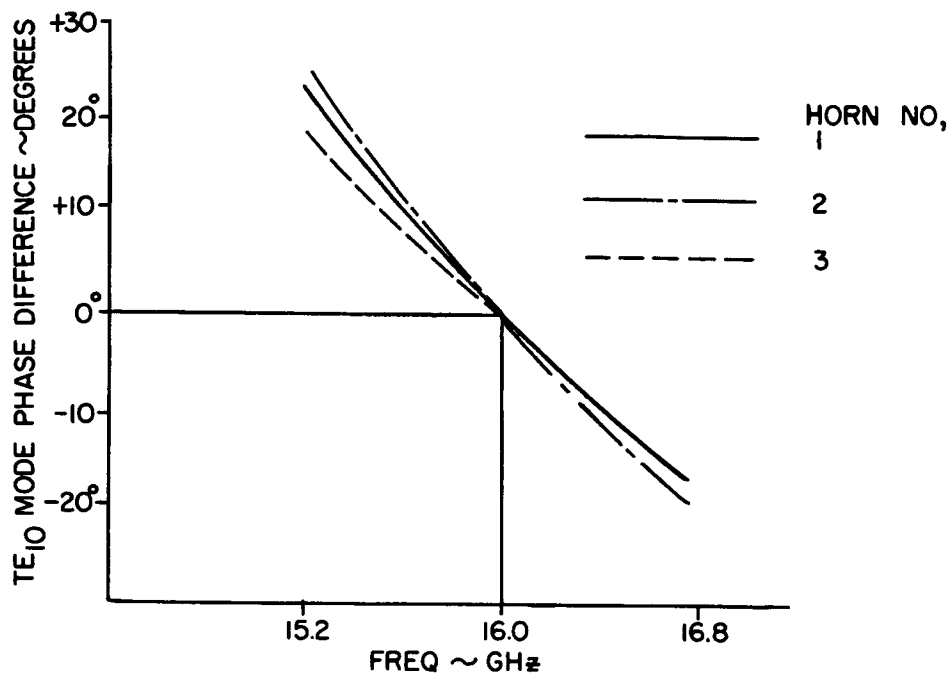
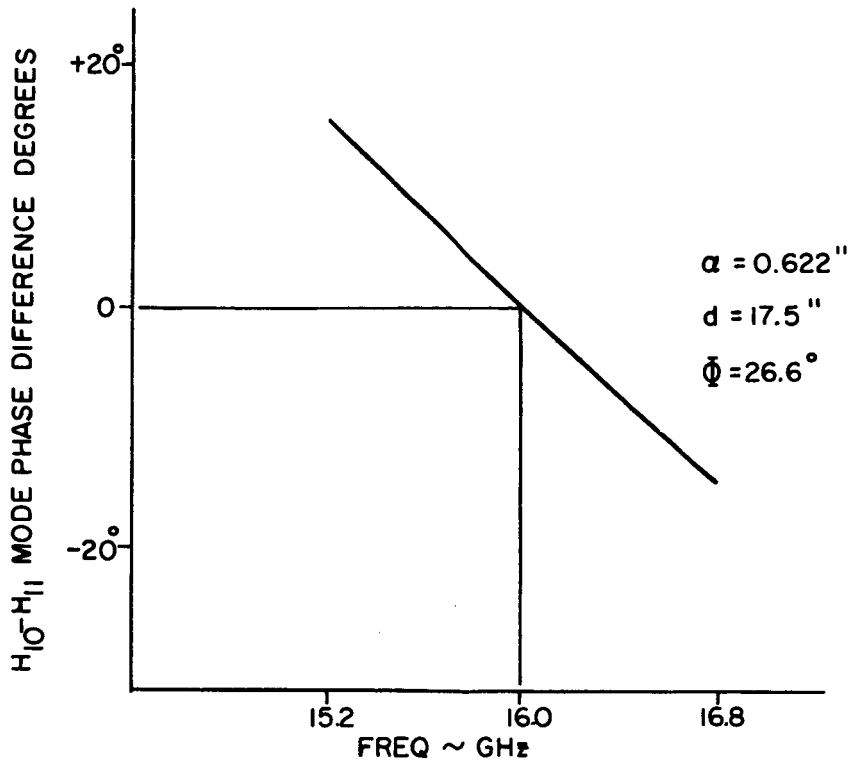Figure 32. Mode and Lens Phase Effects for Three Multimode Horns

Figure 33. Mode Phase Difference vs Frequency, Horn #1 Cylindrical
Mode Generation

Line Source for Parallel Horn Array

The second array configuration evaluated in terms of line source requirements
was the parallel horn array of Figure 27 (b). The scan requirement imposed on this
array is ±30 degrees. This limit was chosen to prevent the horn width from becoming
prohibitively close to cut-off. For the configuration in Figure 27 (b) the spacing between
adjacent horns must satisfy equation (29) and is

$$S_{\lambda HI} \leq 0.667 \tag{32}$$

where

$$S_\lambda = a_\lambda + t_\lambda$$

The horn width a_λ will be approximately 0.6 for a ±30 degree scan capability. To prevent operation of the multimode horn at frequencies close to cut-off, a design bandwidth change to ±2.5% was made.

To satisfy the ±30 degree scan requirement and account for wall thickness the inside "a" dimension of the horn is 0.430 inches. Cylindrical mode generation was provided in the flared horn. The mode phase difference θ_{mn} between the H_{10} and H_{11} modes is plotted against frequency in Figure 34. This data determines α_m for the pattern computation. Lens phase error versus frequency is plotted in Figure 35. Computed pattern characteristics for a reduced width split horn with f/d = 1.0 are given in Table III.
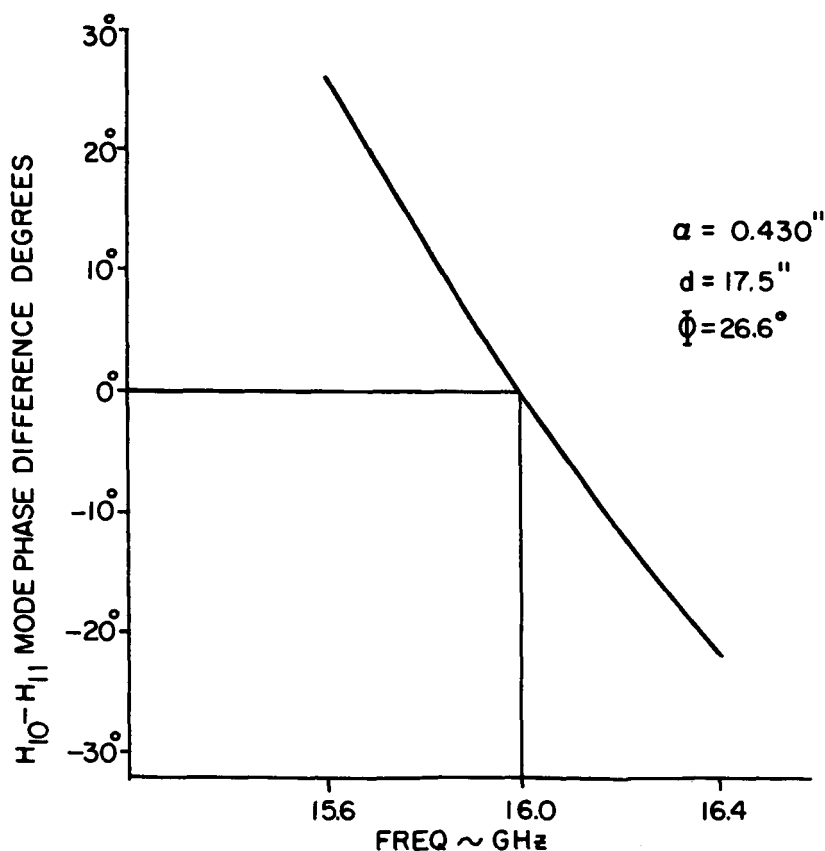

Figure 34. Mode Phase Difference vs Frequency, Horn #4 Cylindrical Mode Generation
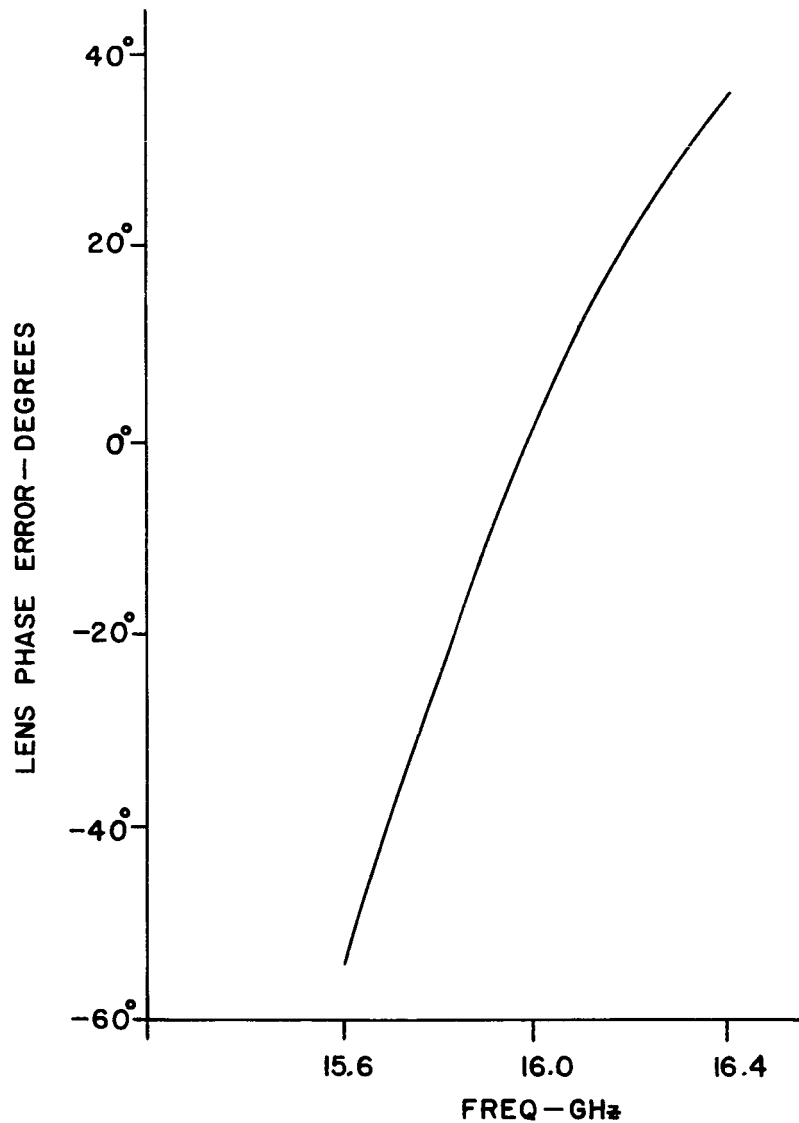
Figure 35. Lens Phase Error vs Frequency, Horn #4

TABLE III

Horn-Lens No.	Line Source Type	15.6 GHz		16.0 GHz		16.4 GHz	
		Max. S. L.	HPBW	Max. S. L.	HPBW	Max. S. L.	HPBW
4	Split Horn (Reduced Width) f/d = 1.0	-25.0 dB	2.9°	-39.6 dB	3.1°	-26.4 dB	2.8°

As before, the above characteristics include all mode phasing and lens effects. Sidelobes are somewhat higher at the band edge due to increased mode phase difference and lens phase error relative to the wider horn design.

EXPERIMENTAL PROGRAM

The multimode line source models discussed in the previous section were fabricated for experimental evaluation. The initial task to be performed required determination of the lens surface impedance matching structures, since a small lens reflection coefficient is required to insure low sidelobe line source patterns. Once this was accomplished, multimode sectoral horn patterns were measured. The horn pattern characteristics were then measured for the horn in an array environment and compared to the isolated horn characteristics.

Line Source Simulators

The impedance mismatch produced by the lens-to-free-space interface was determined using an infinite E-plane line source simulator. Simulator techniques were employed to reduce the complexity and cost that would result if this data were taken on actual lens models. This technique provides for rapid investigation of a variety of interface matching structures, significantly reducing the time otherwise required.

The infinite E-plane line source simulator shown in Figure 36 consists of a rectangular waveguide radiating into a parallel-plate waveguide whose conducting walls are normal to the electric field vector and whose wall-to-wall separation is equal to the waveguide height. When the paralllel-plate waveguide is terminated with suitable lossy material, the rectangular waveguide source is imaged as an infinite E-plane array of waveguide elements with zero thickness walls. Hence an infinite continuous aperture E-plane line source radiating into free space is simulated. The propagation characteristics of the H_{10} and H_{11} sectoral horn modes are essentially equal at the radiating aperture of a narrow-beam multimode sectoral horn. As a result the simulator may be
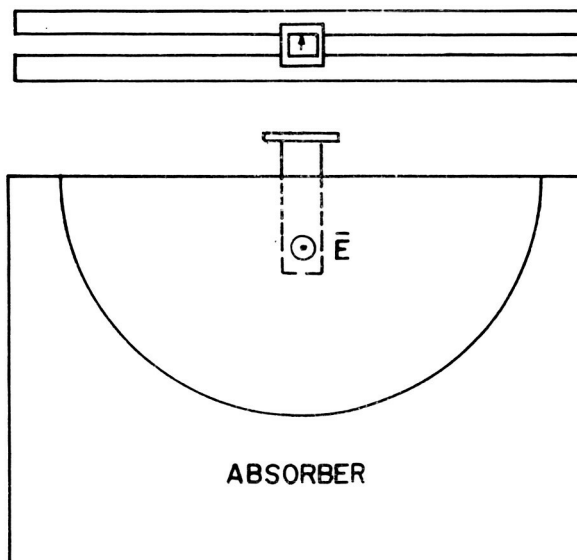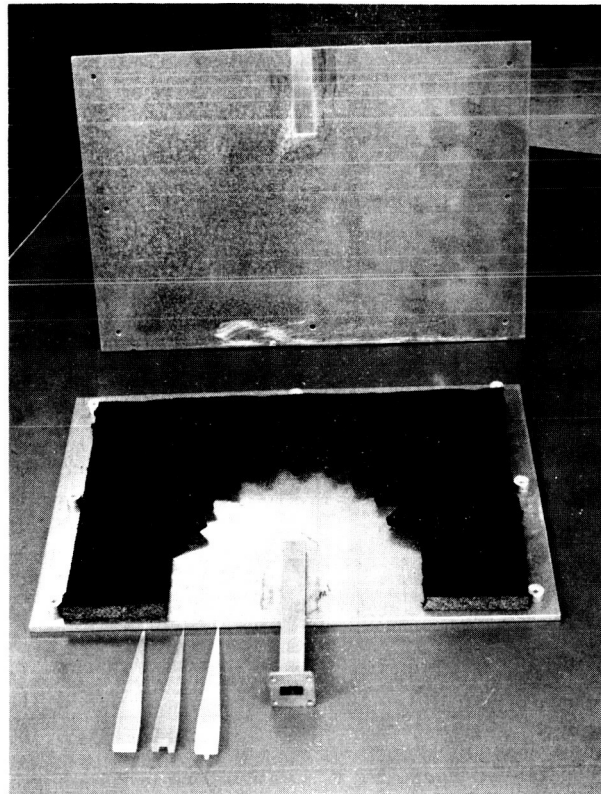
Figure 36.   Line Source Simulator

excited in dominant mode only to give accurate information concerning the interface impedance characteristics for multimode propagation. The rectangular waveguide aperture is completely filled with the lens dielectric material to simulate a radiating horn-lens model.

The impedance characteristics of the horn-lens interface at the refractive lens surface were investigated in a simple waveguide simulator. The simulator consists of a single waveguide section containing a tapered dielectric plug whose incident surface is normal to the direction of wave propagation as shown in Figure 37. Terminating the waveguide in a matched load simulates the horn-lens interface for normal angles of incidence. For polarization parallel to the plane of incidence, which is an inherent property of the E-plane sectoral horn, the reflection coefficient decreases with increasing angle of incidence until the Brewster angle is reached. The Brewster angle occurs beyond the angular limit of typical horn-lens designs, hence normal incidence produces the worst case reflection coefficient.
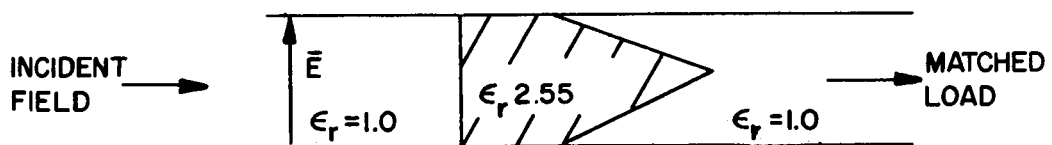

Figure 37. Horn Lens Interface Simulator

The waveguide simulator provides an efficient method for investigating matching transformer structures for the horn-lens interface at normal incidence. The matching structure for normal incidence will provide an effective match for other angles of incidence.

Lens for staggered array. - The normalized impedance vs frequency plot for the lens-free space interface in the infinite array simulator is shown in Figure 38

over the 15. 2 to 16. 8 GHz frequency band for a = 0. 622 inches and $\epsilon_{r_{lens}}$ = 2. 55. Impedance data obtained after incorporation of a matching transformer section are shown in Figure 39. This matching section was utilized on the planar lens surface for the 0. 622-inch wide horns.
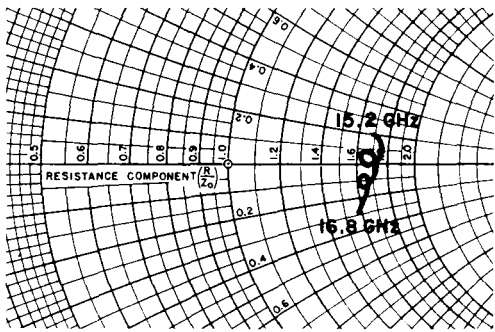

Figure 38. Simulator for Horn-Lens Models #1, 2 and 3, Lens-Free Space Interface
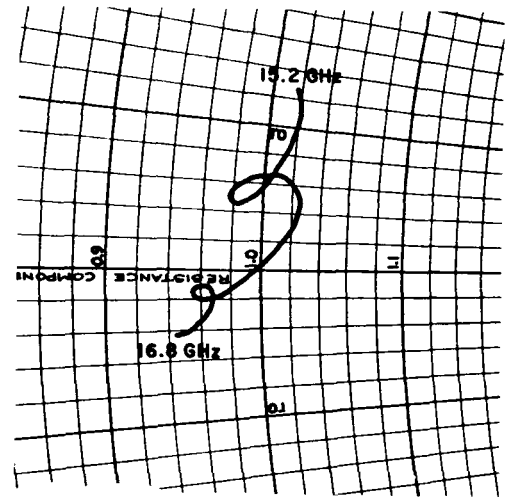
Figure 39. Simulator for Horn-Lens Models #1, 2 and 3, Interface with Matching Transformer

The normalized impedance vs frequency plot for the horn-lens interface in the waveguide simulator is shown in Figure 40 for a = 0. 622 inches and $\epsilon_{r_{lens}}$ = 2. 55. Impedance data obtained after incorporation of a matching transformer section is shown in Figure 41. This matching section was utilized on the hyperbolic refractive lens surface for the 0. 622-inch wide horn.

The matched half lens for horn number 1 is shown in Figure 42. VSWR vs frequency for this horn-lens model excited in H_{10} and H_{11} modes with $\frac{a_{11}}{a_{12}}$ = 0. 8 is also
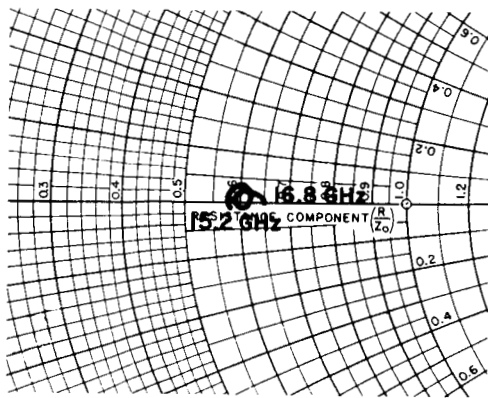
Figure 40. Simulator for Horn-Lens
Models #1, 2 and 3, Horn-
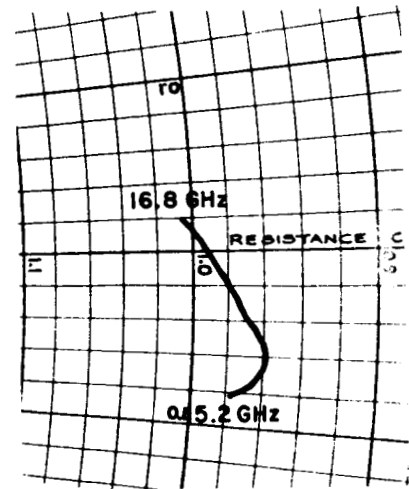Lens Interface

Figure 41. Horn-Lens Interface with
Matching Section

shown in Figure 42. The matching configuration in Figure 42 was also utilized on

horns number 2 and 3. VSWR vs frequency data for $H_{10} + H_{11}$ mode propagation are

shown for these horn-lens models in Figure 43.

Lens for parallel array. - The normalized impedance vs frequency plots for the

lens-to-free-space and horn-lens interfaces are shown in Figure 44 over the 15.6 to

16.4 GHz frequency band for a = 0.430 and $\epsilon_{r_{lens}}$ = 2.55. Impedance data obtained

after incorporation of matching sections is shown in Figure 45.

VSWR vs frequency is plotted in Figure 46 for matched horn-lens model number 4.

Antenna Pattern Range

The antenna test site used for multimode sectoral horn pattern measurements

consists of a test building and 10-foot tower located at a distance of approximately 90

feet. The test building is divided into an open-ended anechoic room with protective

dielectric sheet at the open end and a separate test equipment room. A K_u-band wave-

guide run installed between the test building and tower provides for transmission to a
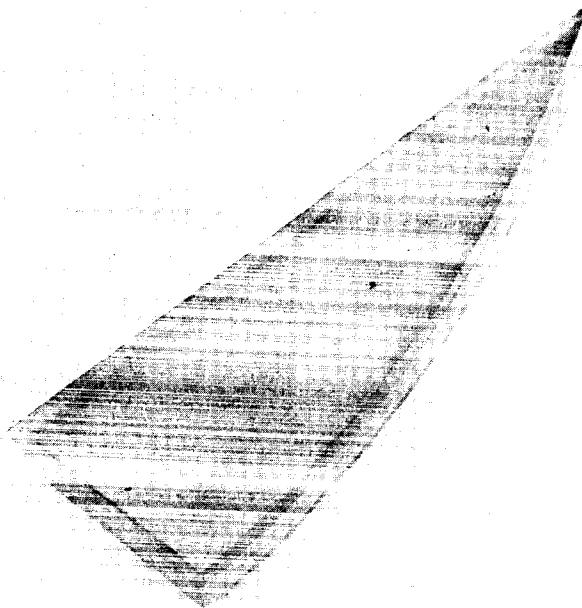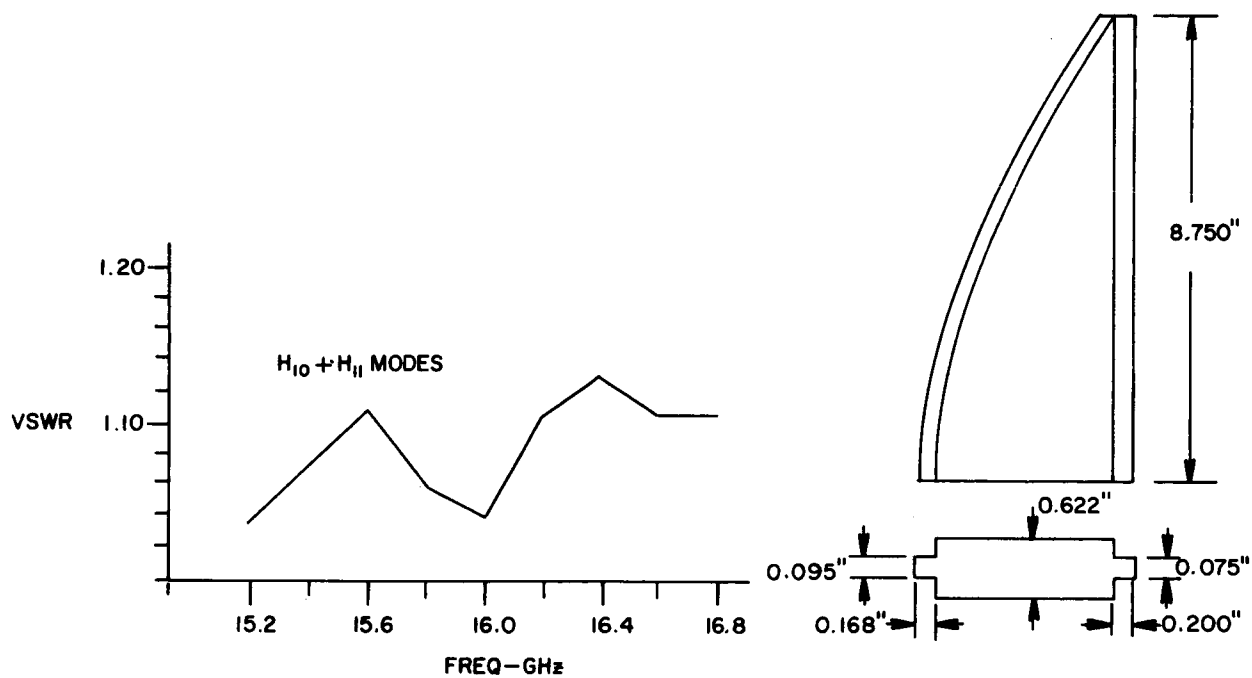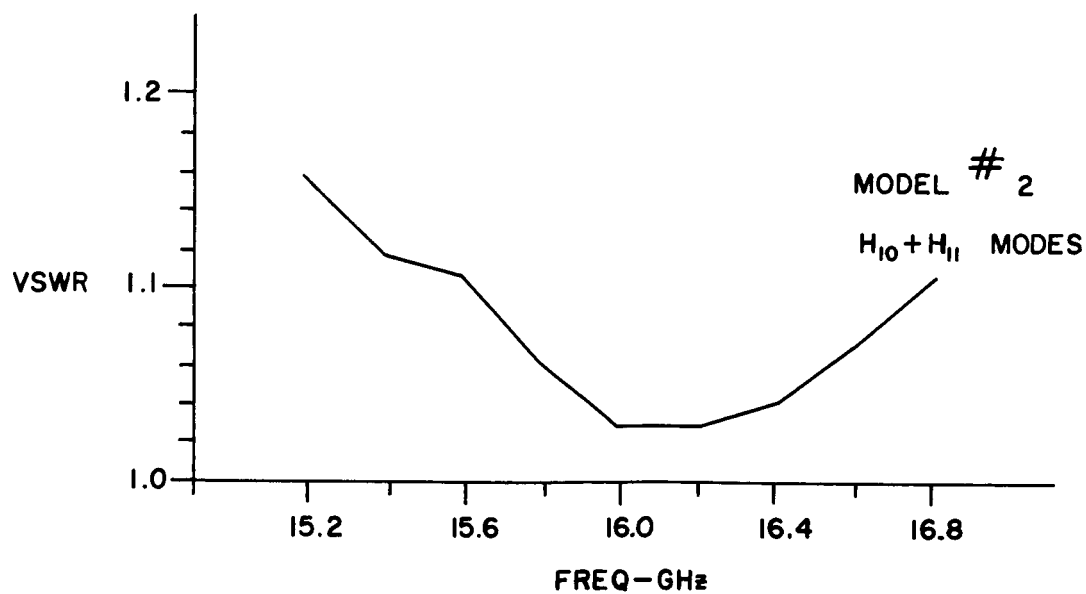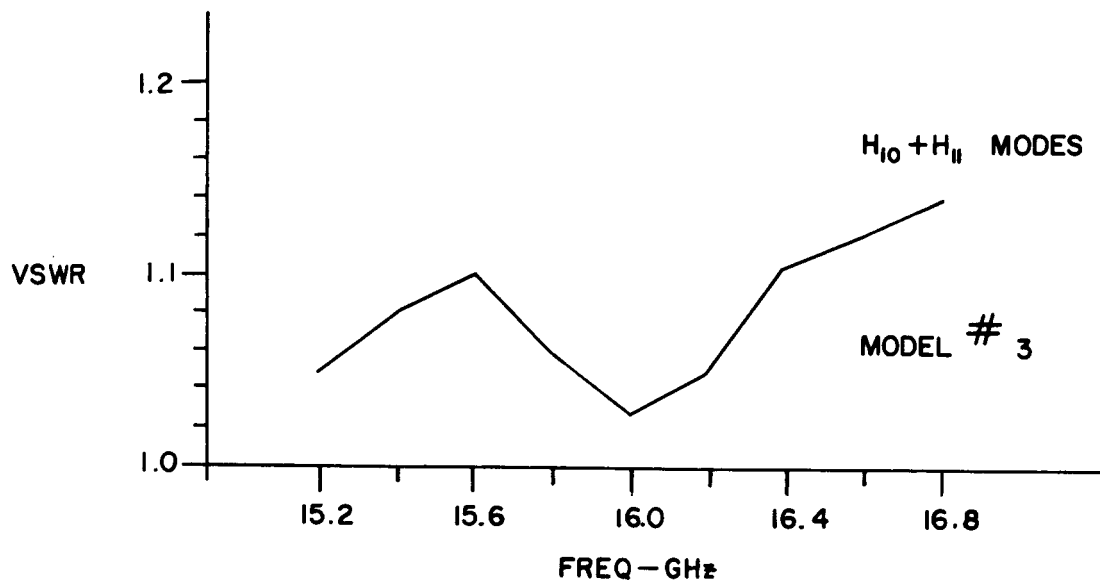
54

Figure 42. Half-Lens for Horn #1, VSWR vs Frequency

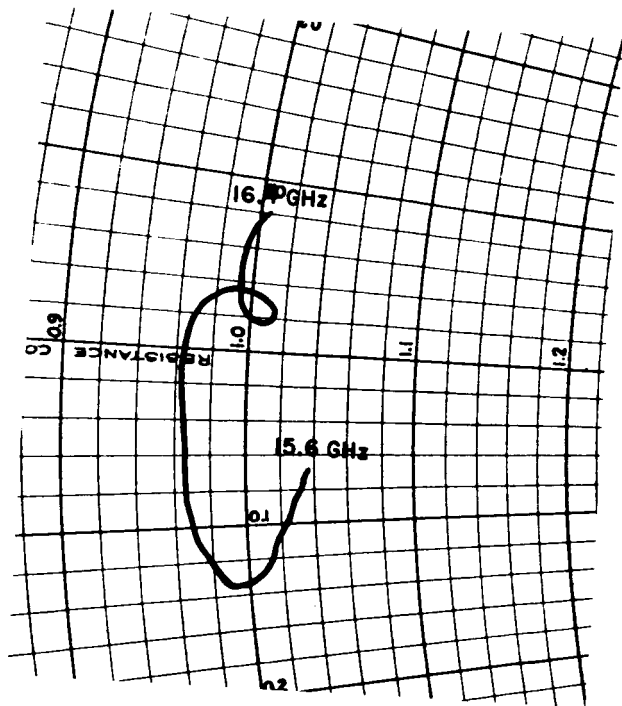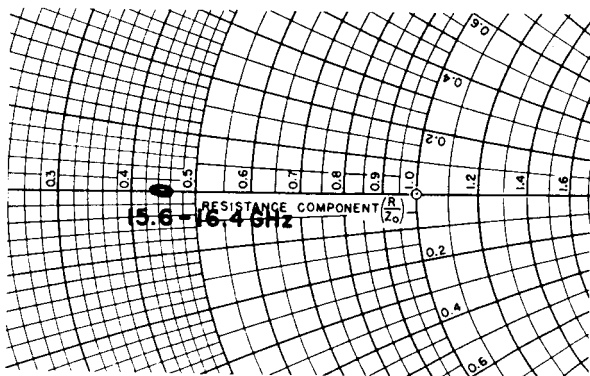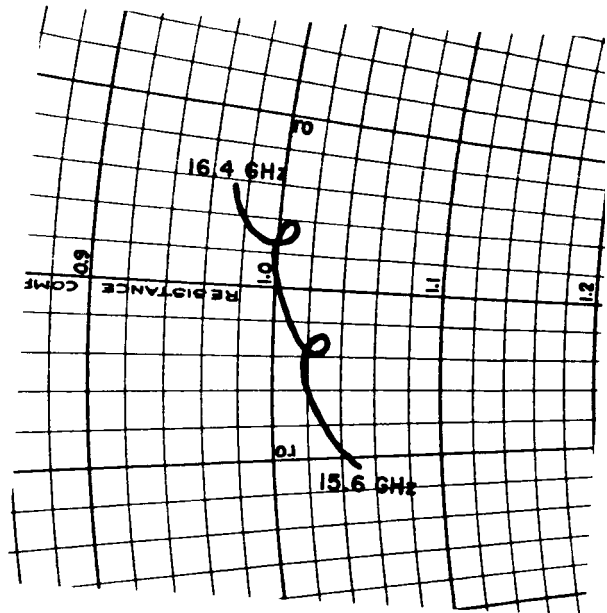Figure 43.   Horn-Lens Models #2 and #3, VSWR vs Frequency
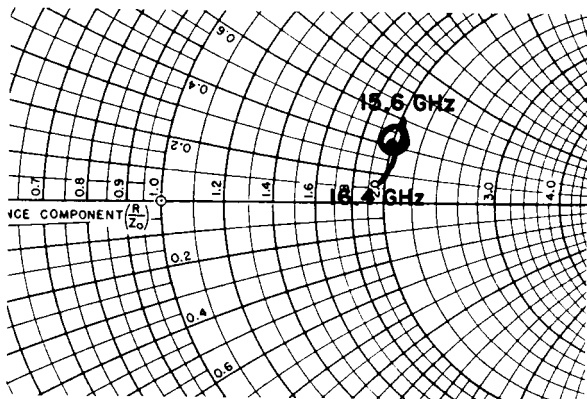
Figure 44. Simulator for Horn-Lens
Model #4, Reduced-Width
Design

Figure 45. Simulator for Horn-Lens
Model #4, Reduced-Width
Design

57
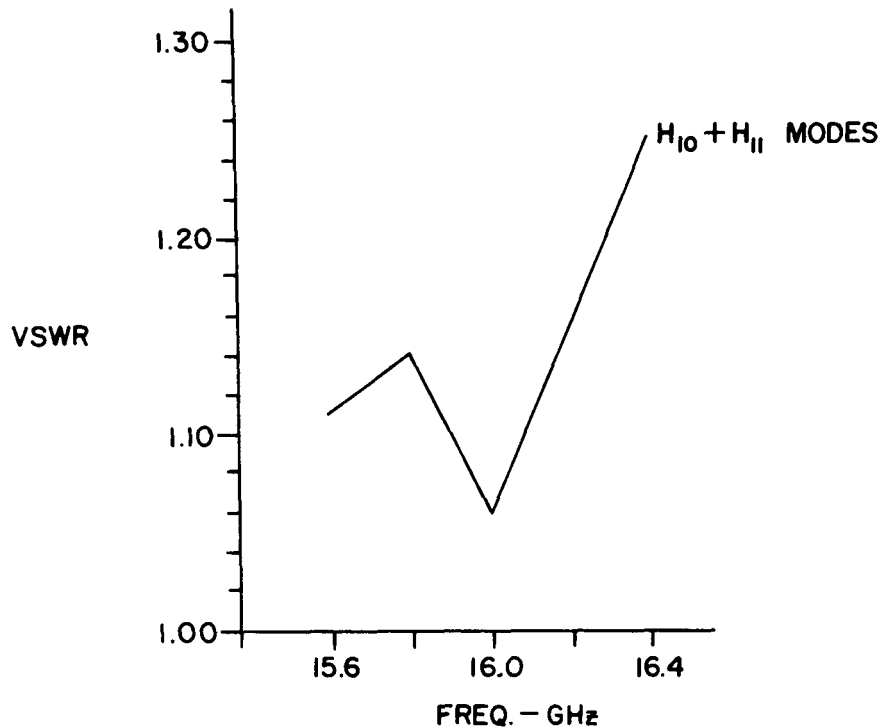
Figure 46. Horn-Lens Model #4, VSWR vs Frequency, Lens in Place

16-inch K_u-band reflector antenna at the tower. A reflecting screen located between the tower and anechoic room eliminates ground reflections and provides an incident field across the line source aperture that is uniform to within ±0.3 dB. A photograph of the antenna test site is shown in Figure 47.

A block diagram of the antenna pattern test equipment is shown in Figure 48. A dynamic range of 60 dB was provided with this equipment.

Line Source Pattern Measurements

Horn-lens models for staggered array. - The first multimode line source fabricated was the split-horn model, horn number one. This model, illustrated in Figure 29, utilized the technique of mode generation in the rectangular waveguide preceding the horn. A series of patterns were recorded on the model to experimentally

Figure 47. Antenna Test Facility

59

Figure 48. Block Diagram of Antenna Pattern Test Equipment

determine the mode generating step dimensions required to obtain patterns like those computed for $a_{11}/a_{10} = 0.8$. Several measured patterns are shown in Figure 49 for calculated values of a_{11}/a_{10}. The actual mode amplitude ratio, determined from 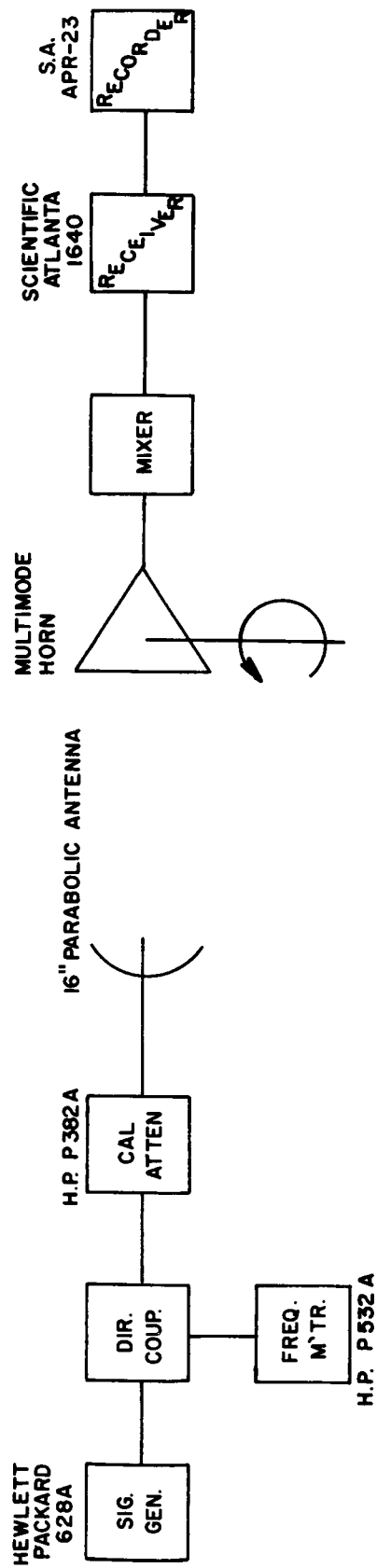the measured beamwidths is also shown in Figure 49. In all cases the actual mode amplitude ratio exceeded the calculated. To obtain a mode amplitude ratio of 0.8, a step whose calculated mode amplitude ratio is less than 0.4, was required. In addition to this discrepancy, maximum measured sidelobes could not be reduced below -27 dB. The lack of correlation between measured and calculated mode amplitude ratio and sidelobe levels was attributed partially to unwanted mode generation at the horn throat which is a region of H_{10} and H_{11} mode propagation. Mode generation results because of the discontinuity existing at the horn throat between the horn and connecting rectangular waveguide.

The first horn-lens model was later modified to provide cylindrical mode generation and phasing totally within the horn, as shown in Figure 12. The horn throat for this configuration terminates in standard rectangular waveguide in a region where the horn can support H_{10} mode only. Any higher order modes generated at the horn throat are cut-off and will attenuate very rapidly into the horn. A pattern measured at center frequency 16 GHz for calculated mode amplitude ratio a_{11}/a_{10} of 0.8 is shown in Figure 50; the measured value of a_{11}/a_{10} is indicated. A much closer agreement between predicted and measured patterns results using the cylindrical mode generation technique.

Dominant H_{10} mode patterns of horn-lens model number one with cylindrical mode generation are shown in Figure 51 along with computed H_{10} mode patterns. The unsymmetrical sidelobe structure of the measured H_{10} mode patterns is the result of a phase difference between halves of the horn model. A series of horn width measurements indicated an average difference of 1 mil between halves resulting in an approximate 7-degree phase difference. A small compensating foam dielectric ($\epsilon_r = 1.05$) phase shifter incorporated into one half horn in the region of H_{10} propagation, improved symmetry resulting in the pattern shown in Figure 52. Multimode pattern sidelobe

Figure 49a. $H_{10} + H_{11}$ Mode Pattern for Horn #1 (Sheet 1 of 3)

62

Figure 49b. $H_{10} + H_{11}$ Mode Pattern for Horn #1 (Sheet 2 of 3)

The figure contains the following labels:

DESIGN VALUE
$\frac{a_{11}}{a_{10}} = 0.9$

ACTUAL VALUE
$\frac{a_{11}}{a_{10}} > 1.4$

FREQ. = 16 GHz

HPBW = 6°

RELATIVE POWER ONE WAY (db)

ANGLE

63

Figure 49c. $H_{10} + H_{11}$ Mode Pattern for Horn #1 (Sheet 3 of 3)

64

Figure 50. $H_{10} + H_{11}$ Modes, Cylindrical Mode Generation

65

Figure 51. H_{10} Mode Pattern for Horn #1

FREQ.=16 GHz
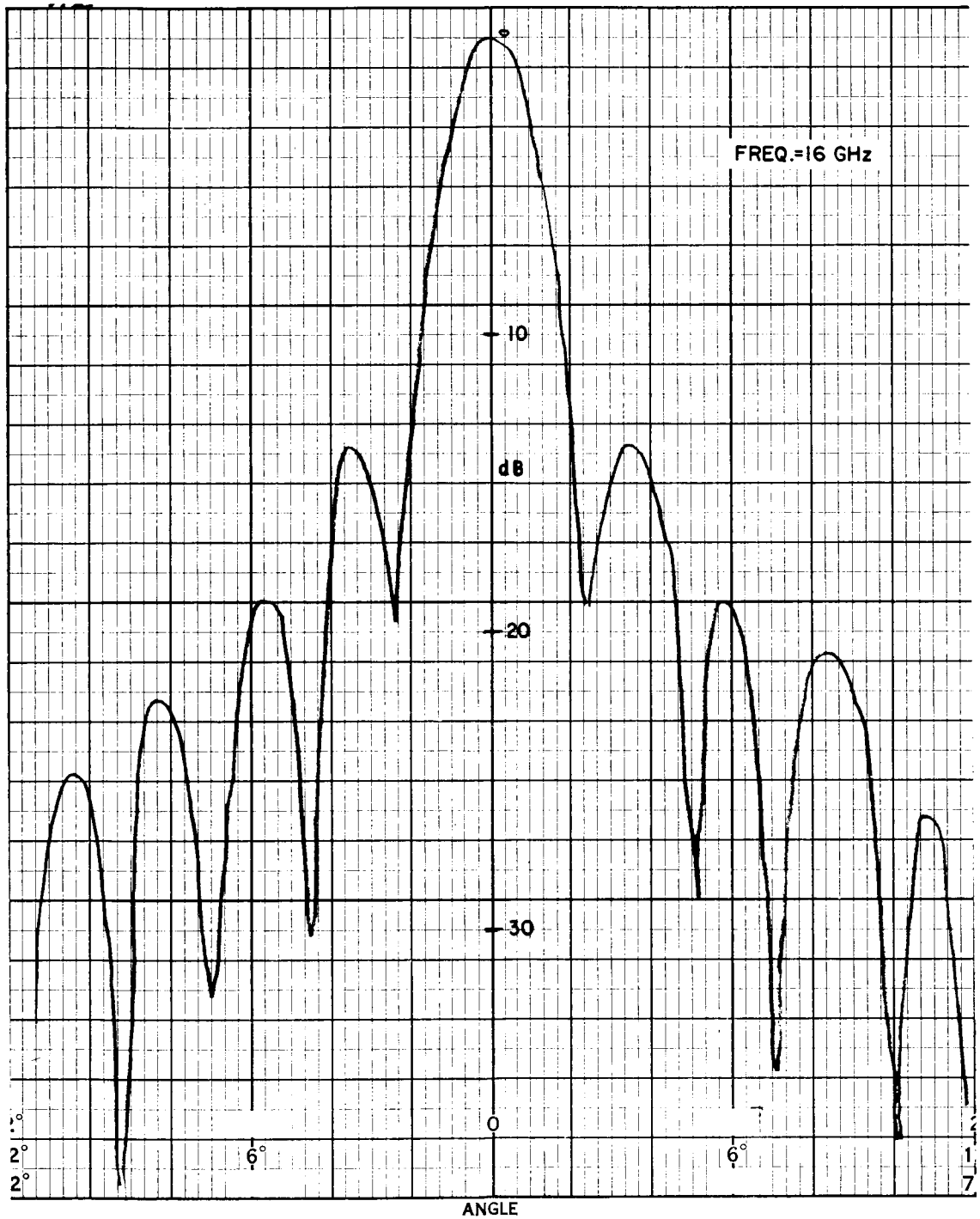
Figure 52. Compensated H_{10} Mode Pattern for Horn #1

levels were reduced approximately 3 dB by eliminating the macroscopic air gaps between the lens and horn walls. This was accomplished by applying a thin coating of silicon grease to the lens surfaces which contacted the horn walls. $H_{10} + H_{11}$ mode patterns of the compensated horn measured over the 15.2- to 16.8-GHz frequency band are shown in Figure 53. Over at least half the frequency band no sidelobes exceed -30 dB. Sidelobe levels are consistently low over the full frequency band. Beam efficiency calculations were performed for the patterns in Figure 53 with the pessimistic assumption that the array pattern formed will be a figure of revolution of these patterns. Beam efficiency vs frequency for a square array of these line sources is plotted in Figure 54. Calculated beam efficiencies in excess of 95% result over approximately half the frequency band.

Multimode patterns of horn number 3 were measured over the 15.2- to 16.8-GHz frequency band. Sidelobe levels were consistently between -20 and -25 dB, somewhat higher than expected. These levels are partially attributable to the "hole" which exists at the center of the aperture field distribution caused by the lens taper.

Dominant mode patterns of the shorter split-horn line source, horn number 2, were measured. Measured patterns showed evidence of excessive aperture phase error. This is primarily due to difficulties which arise in attempting to generate the required cylindrical wave in this short horn. The large horn flare angle, ($\Phi = 45°$), is responsible. A tapered transition from rectangular waveguide to the flared horn was tried with little success.

Horn-lens model number one, although having desirable line source pattern characteristics, was not suitable for use in a scanned array because of the grating lobe problem associated with the "staggered" array discussed in Appendix A. All work on the staggered array concept was discontinued after evaluation of the associated line source models. Work continued on the line source model for the parallel array.
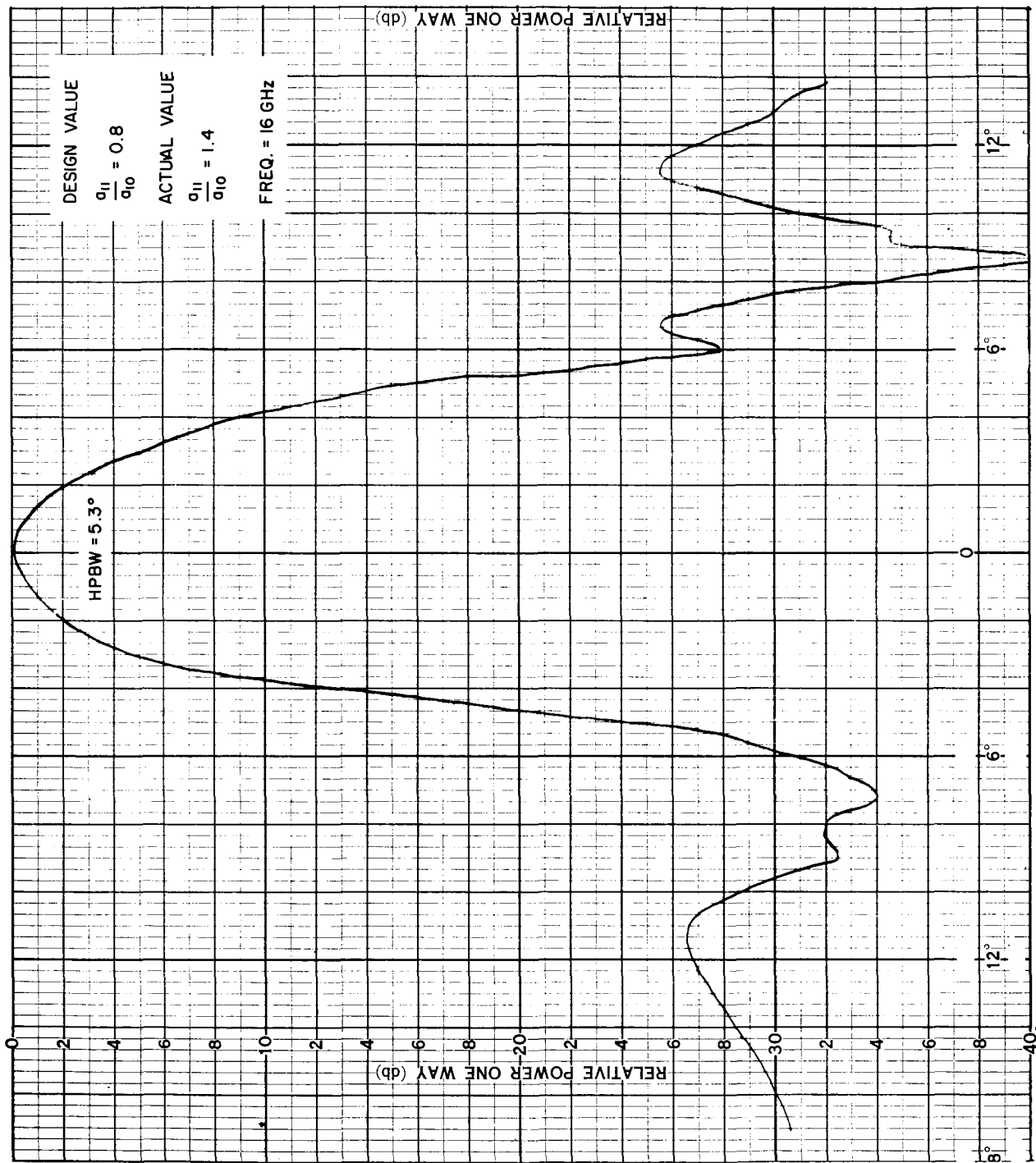
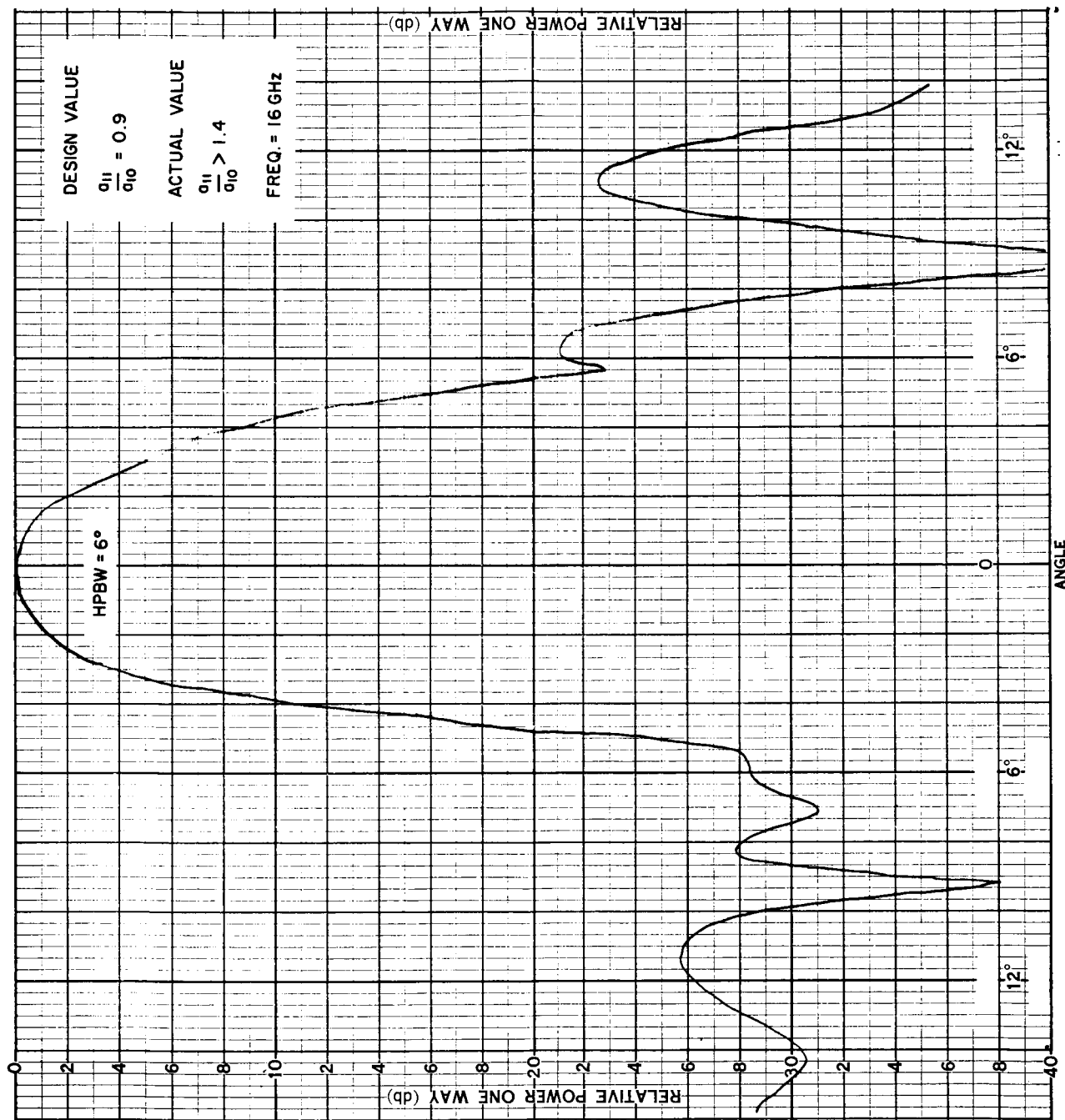Figure 53a. $H_{10} + H_{11}$ Mode Pattern for Horn #1 (Sheet 1 of 5)

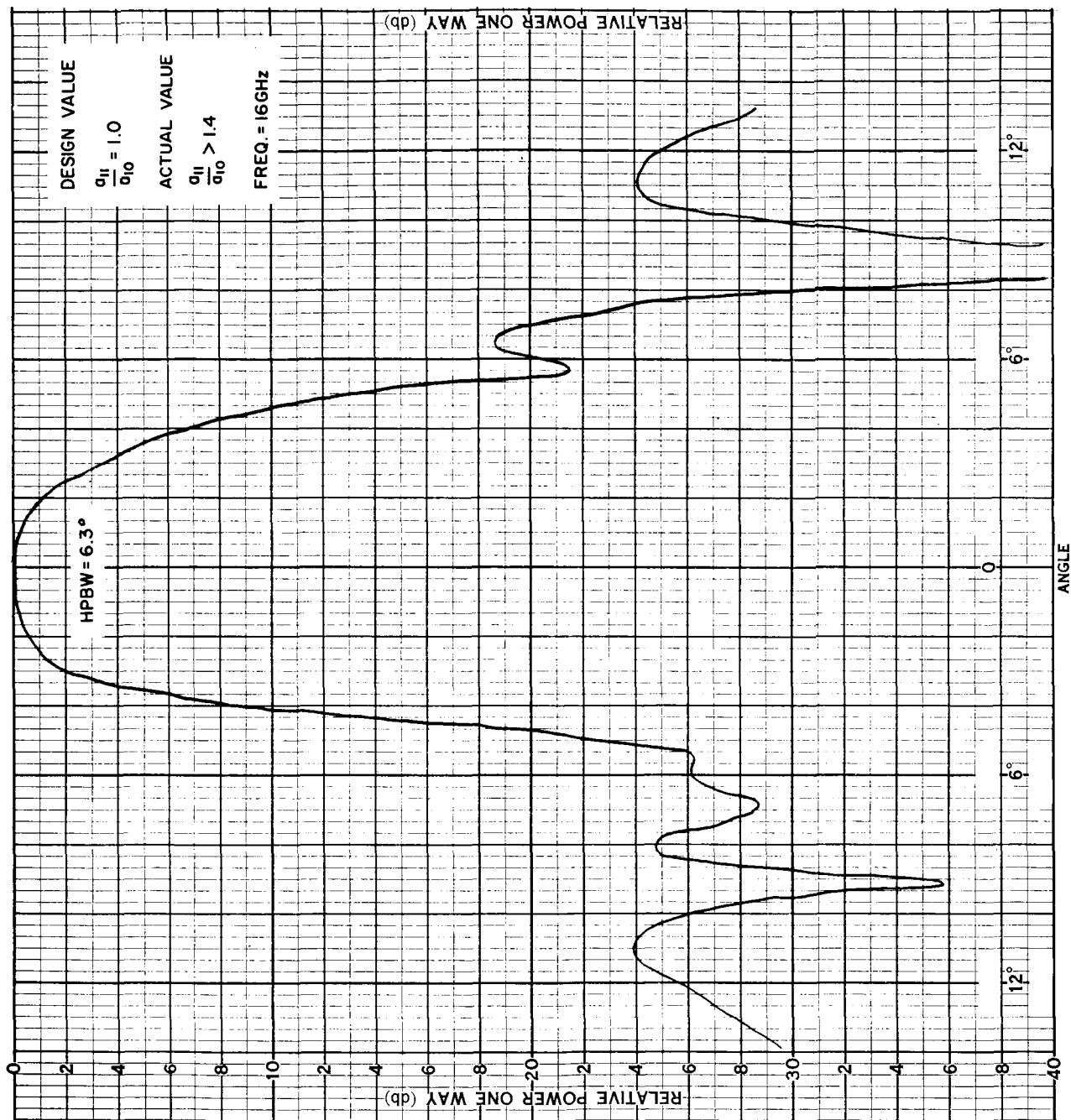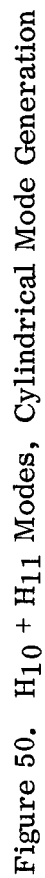Figure 53b. $H_{10} + H_{11}$ Mode Pattern for Horn #1 (Sheet 2 of 5)

70

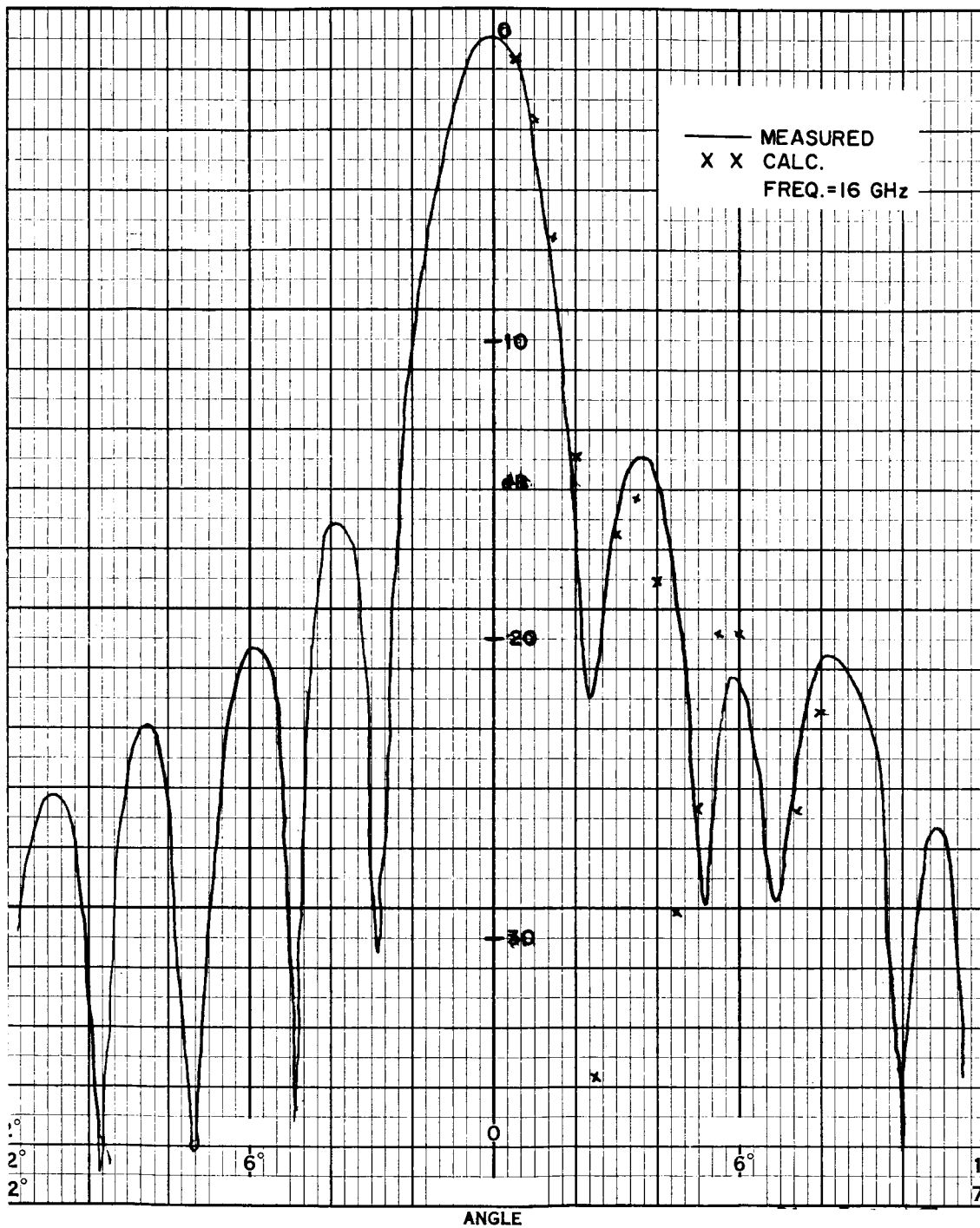Figure 53c. $H_{10} + H_{11}$ Mode Pattern for Horn #1 (Sheet 3 of 5)

71

FREQ = 16.4 GHz

Figure 53d. $H_{10} + H_{11}$ Mode Pattern for Horn #1 (Sheet 4 of 5)

Figure 53e. $H_{10} + H_{11}$ Mode Pattern for Horn #1 (Sheet 5 of 5)
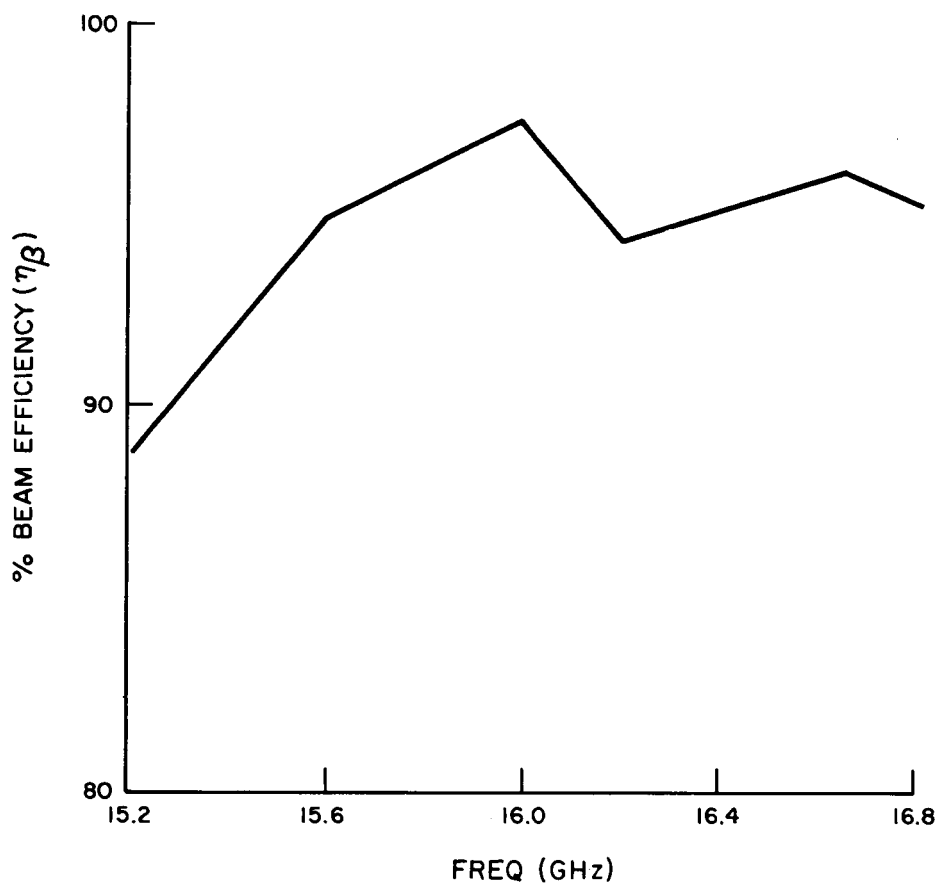
Figure 54. Calculated Beam Efficiency vs Frequency for
17. 5" x 17. 5" Square Multimode Array

Horn-Lens model for parallel array. - After complete evaluation of horn number
one for the staggered array, modifications were made resulting in a reduced width de-
sign with 17. 500 x 0. 430-inch inside dimensions.   This new model horn number four
was designed for use in the parallel array arrangement previously discussed.   Cylin-
drical mode generation and phasing were provided totally within the horn as shown in
Figure 12.

74

Dominant H_{10} mode patterns of horn-lens model number four are shown in Figure 55. The unsymmetrical sidelobe structure can again be attributed to a phase difference between halves of the horn model. Because of the reduced horn width, fabrication tolerances are extremely critical. Analysis indicates that a phase difference on the order of 25 degrees can produce the observed effect. Compensating foam-dielectric phase shifters and reactive-post phase shifters were employed to compensate for the difference.

$H_{10} + H_{11}$ mode patterns were measured over the 15.6- to 16.4-GHz band. These patterns are shown in Figure 56. The best patterns have maximum sidelobes of approximately -26 dB, which is 4 to 5 dB higher than the best obtained from the wider single-horn line source. Calculated maximum beam efficiency is 89%. Slight changes were made to both the lens refractive surface and impedance matching transformer surface in an attempt to improve performance. Maximum sidelobe levels increased 2 to 4 dB. Development of the reduced-width line source was stopped at this point to proceed to the next phase of the program requiring incorporation of an active line source into a prototype array.

<div align="center">Prototype Array</div>

A program was initiated to determine the effect of an array environment on the properties of a single multimode sectoral horn. In order to provide a real array environment to the multimode sectoral horn, it was decided that adjacent horns should be real multimode horn-lens models and all other horns dummy elements. The dummy elements are rectangular waveguides with line source aperture dimensions terminated in suitable matched loads.

An array of three multimode sectoral horns based on design parameters of horn number four were designed along with two five-element dummy arrays. At the time of writing of this report the three real-element array is being fabricated. Fabrication of the dummy elements has been completed.
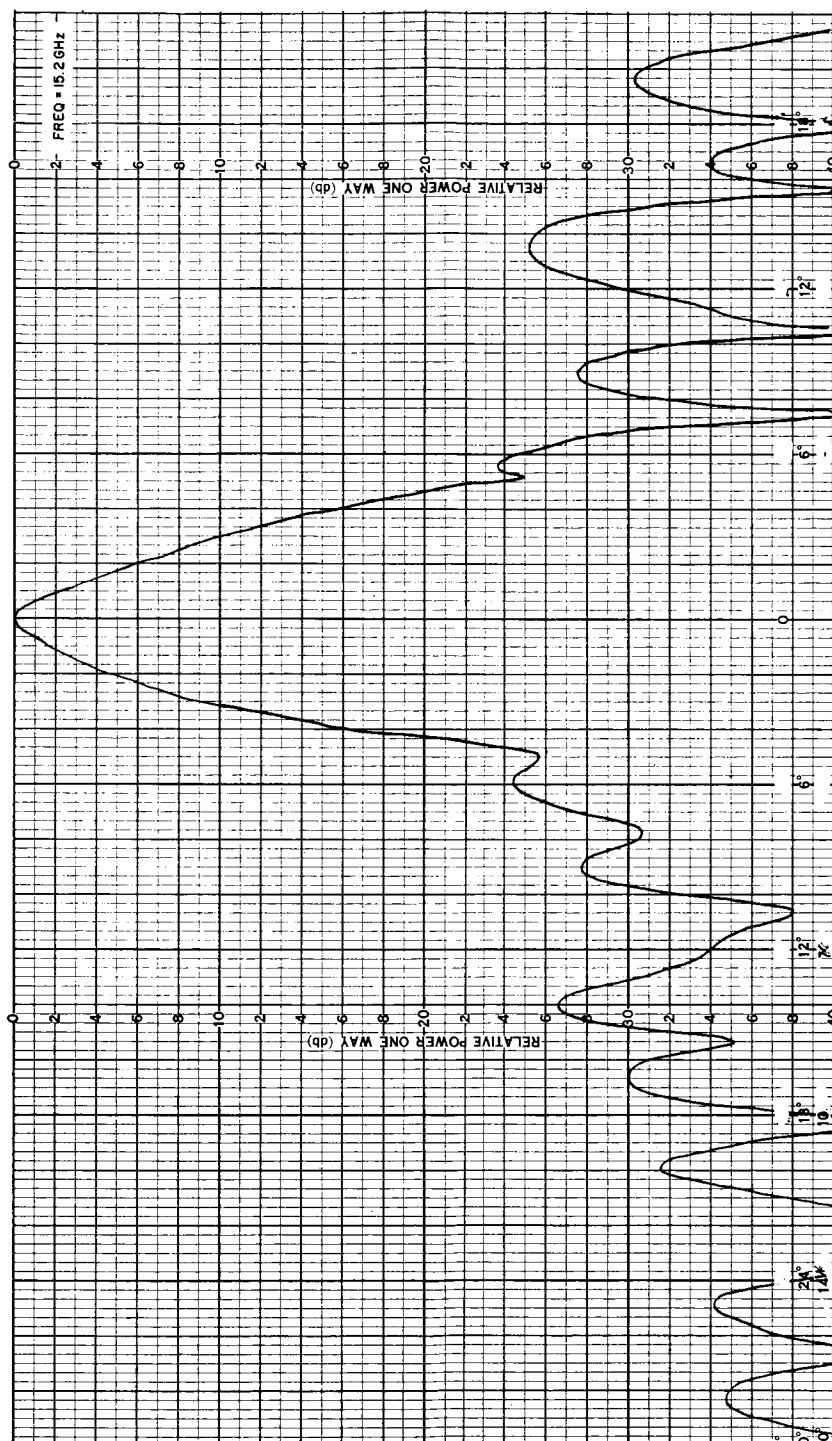
Figure 55. H_{10} Mode Pattern for Horn #4

Figure 56a. $H_{10} + H_{11}$ Mode Pattern for Horn #4 (Sheet 1 of 5)
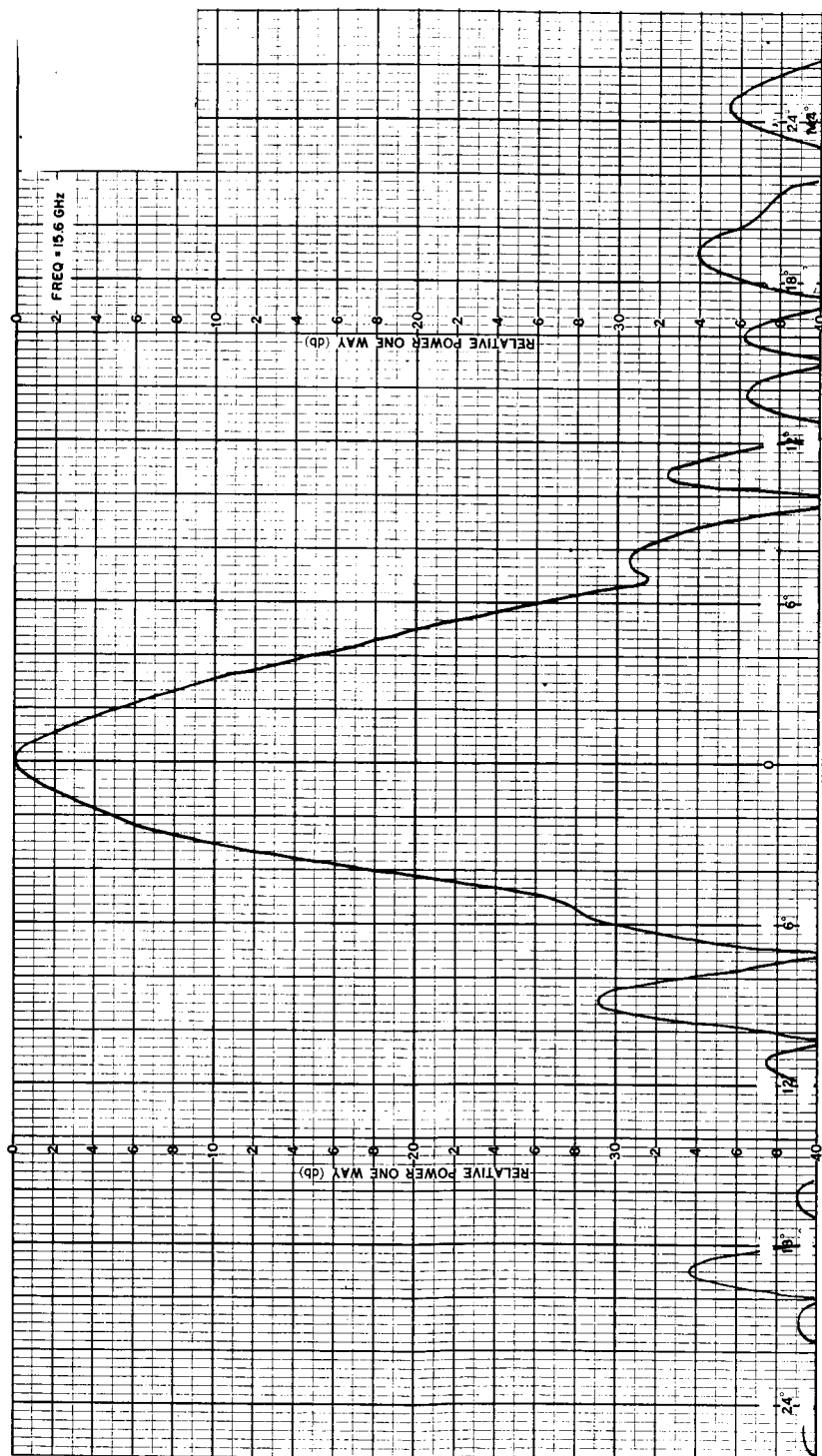
77

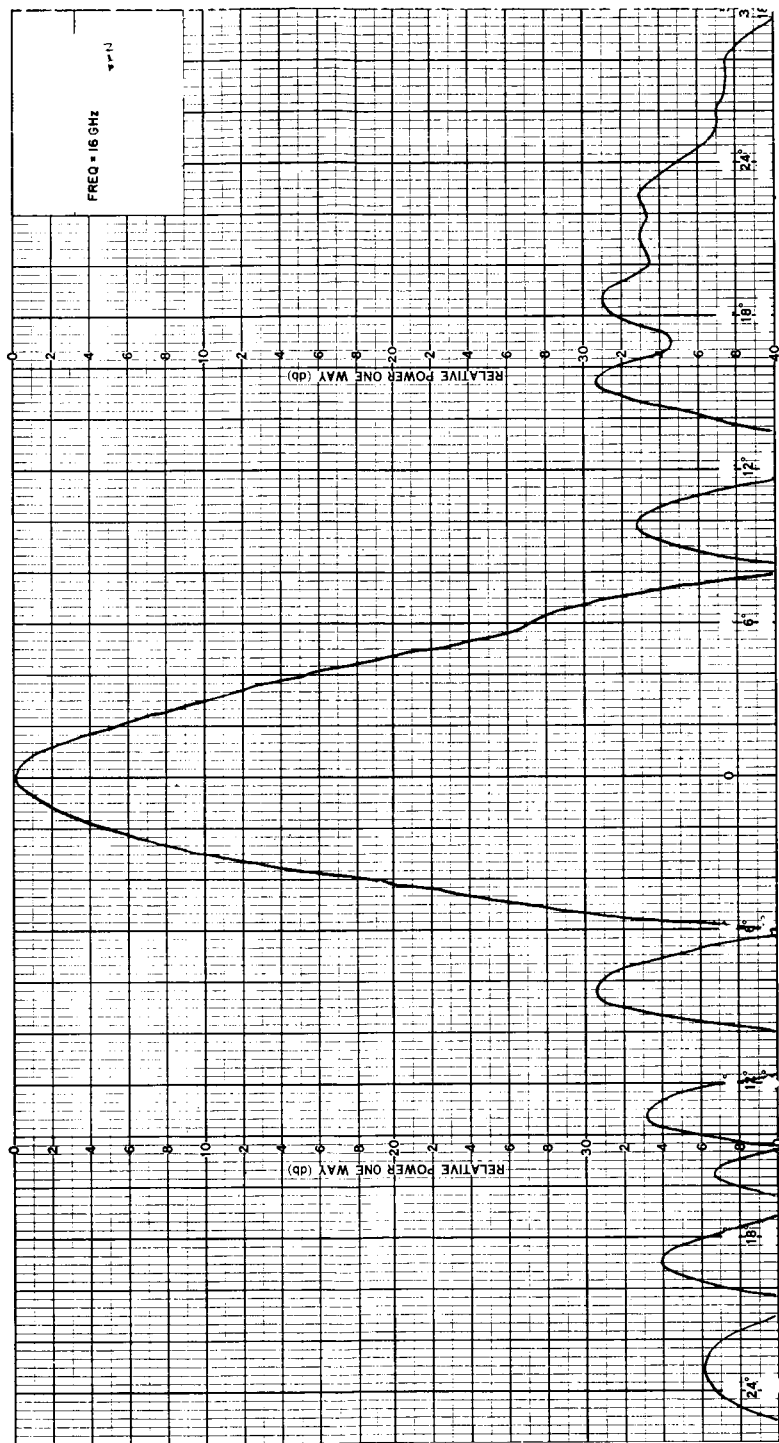Figure 56b. $H_{10} + H_{11}$ Mode Pattern for Horn #4 (Sheet 2 of 5)

78
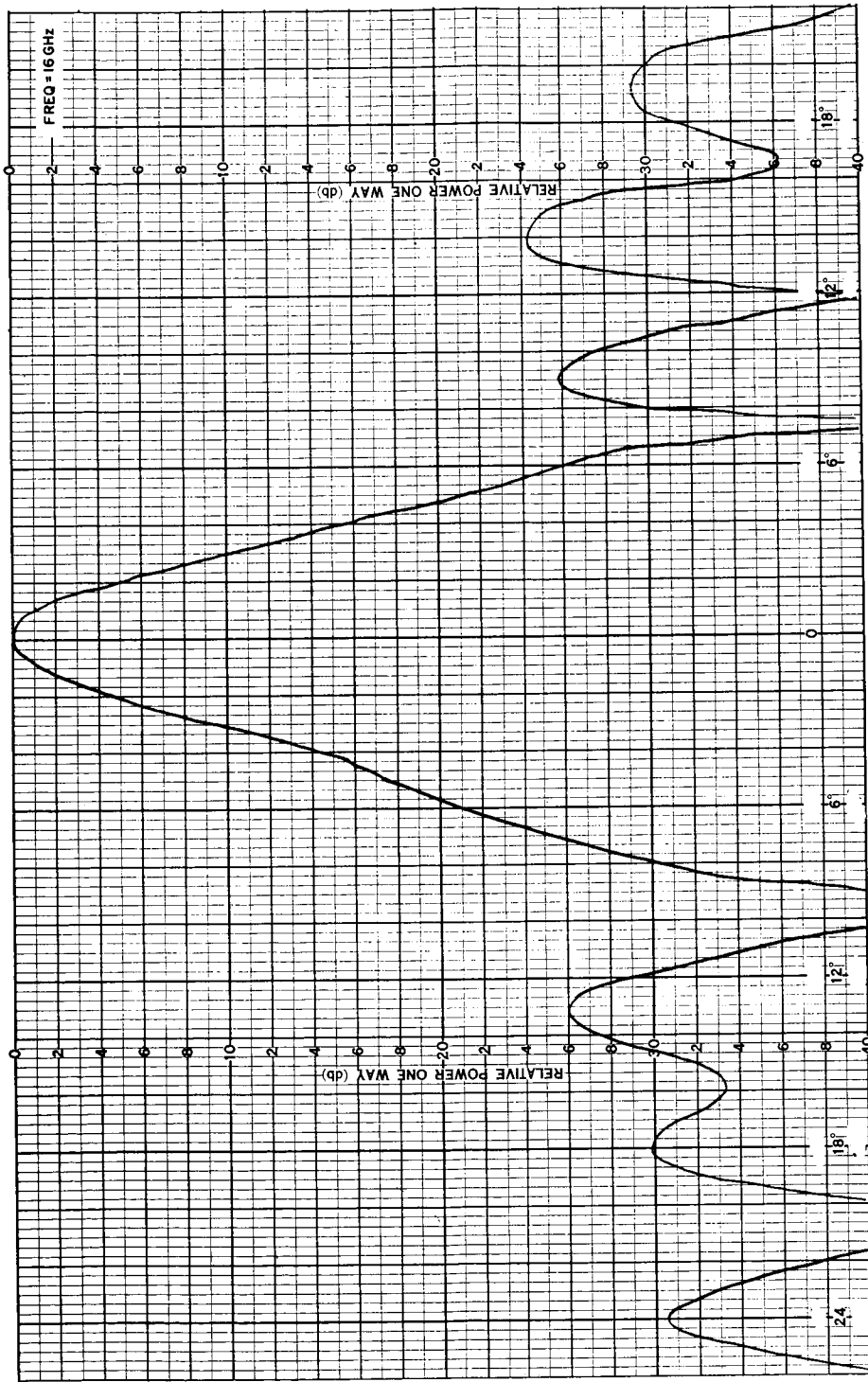
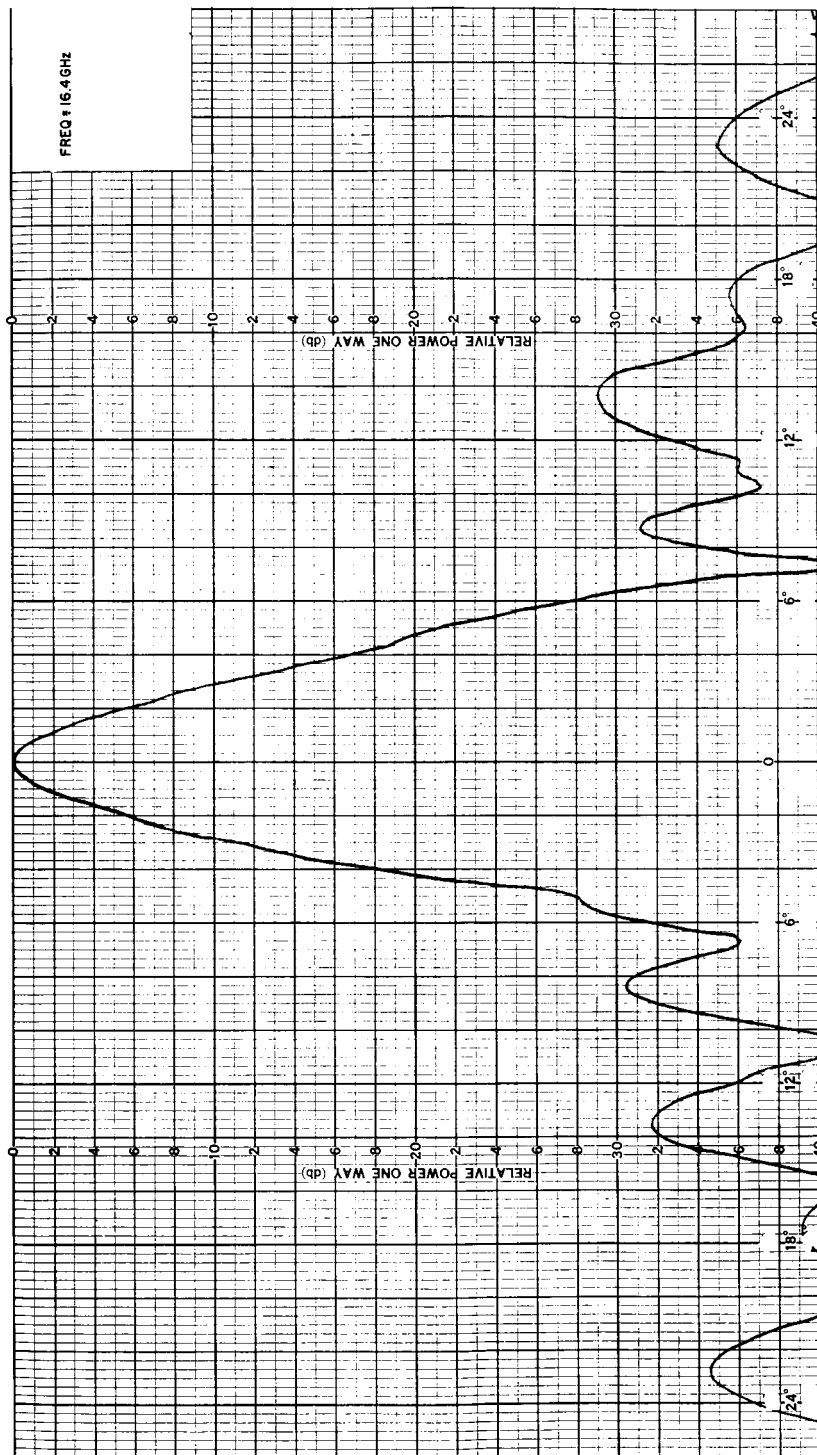Figure 56c. $H_{10} + H_{11}$ Mode Pattern for Horn #4 (Sheet 3 of 5)
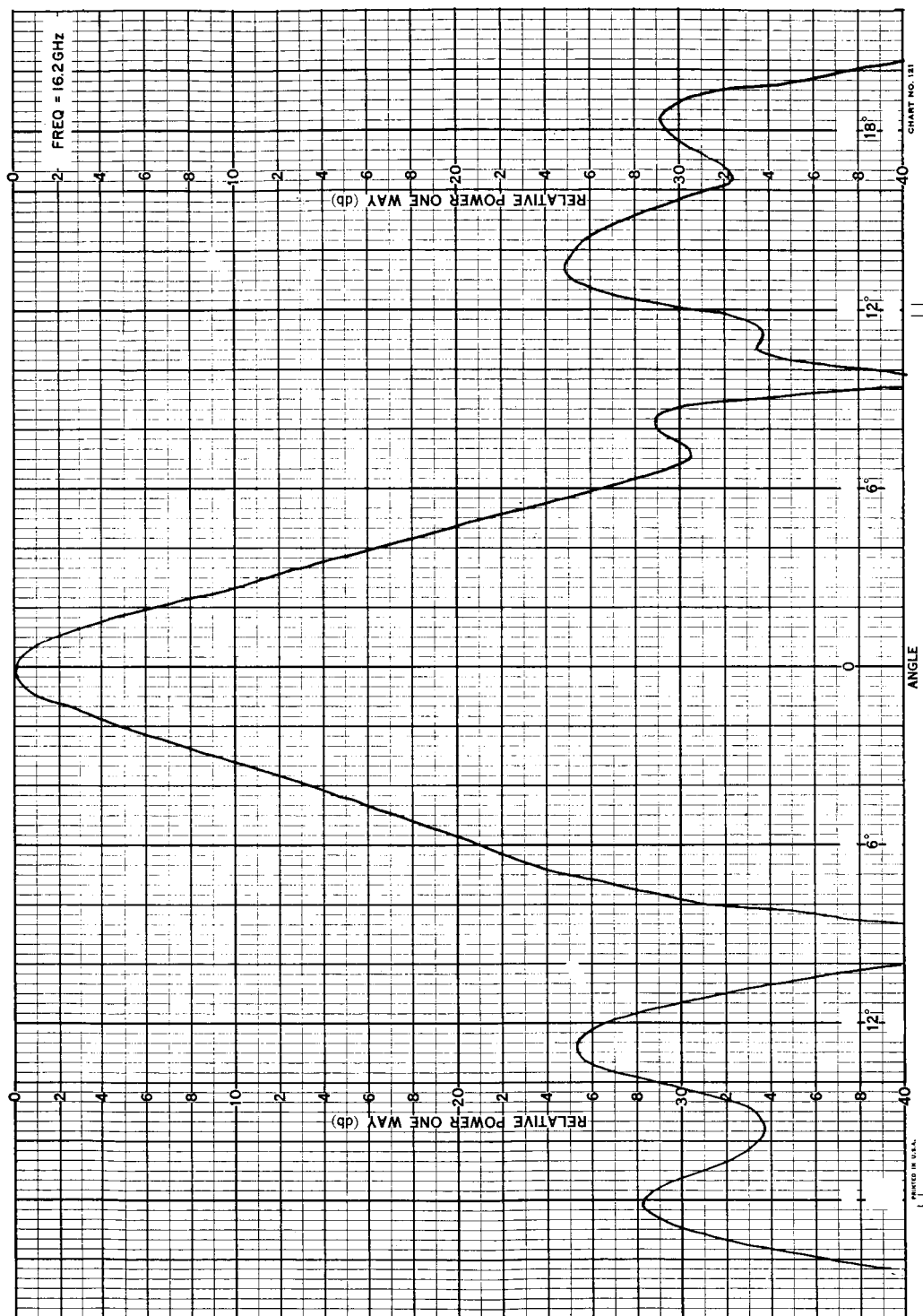
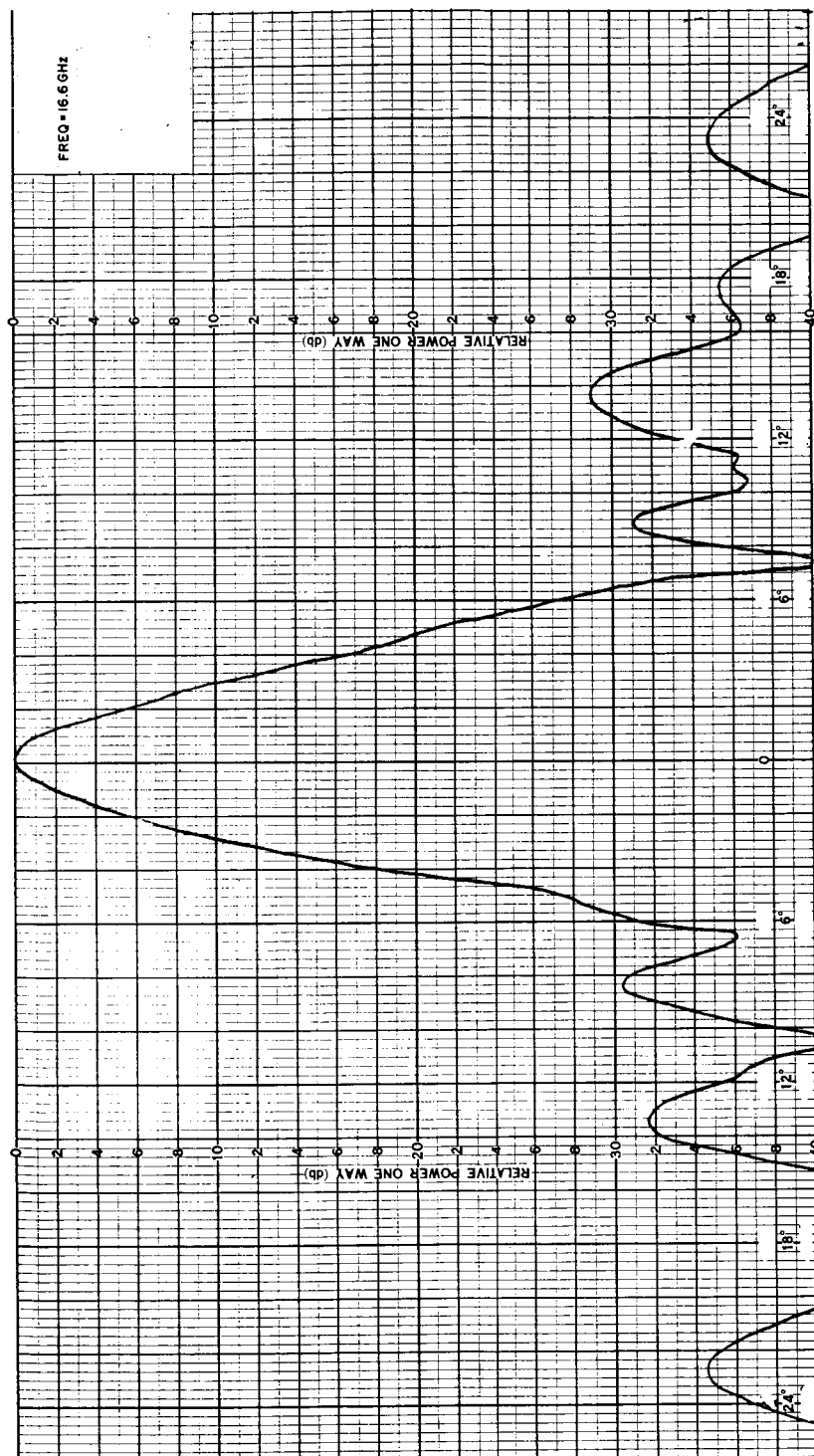Figure 56d. $H_{10} + H_{11}$ Mode Pattern for Horn #4 (Sheet 4 of 5)

80

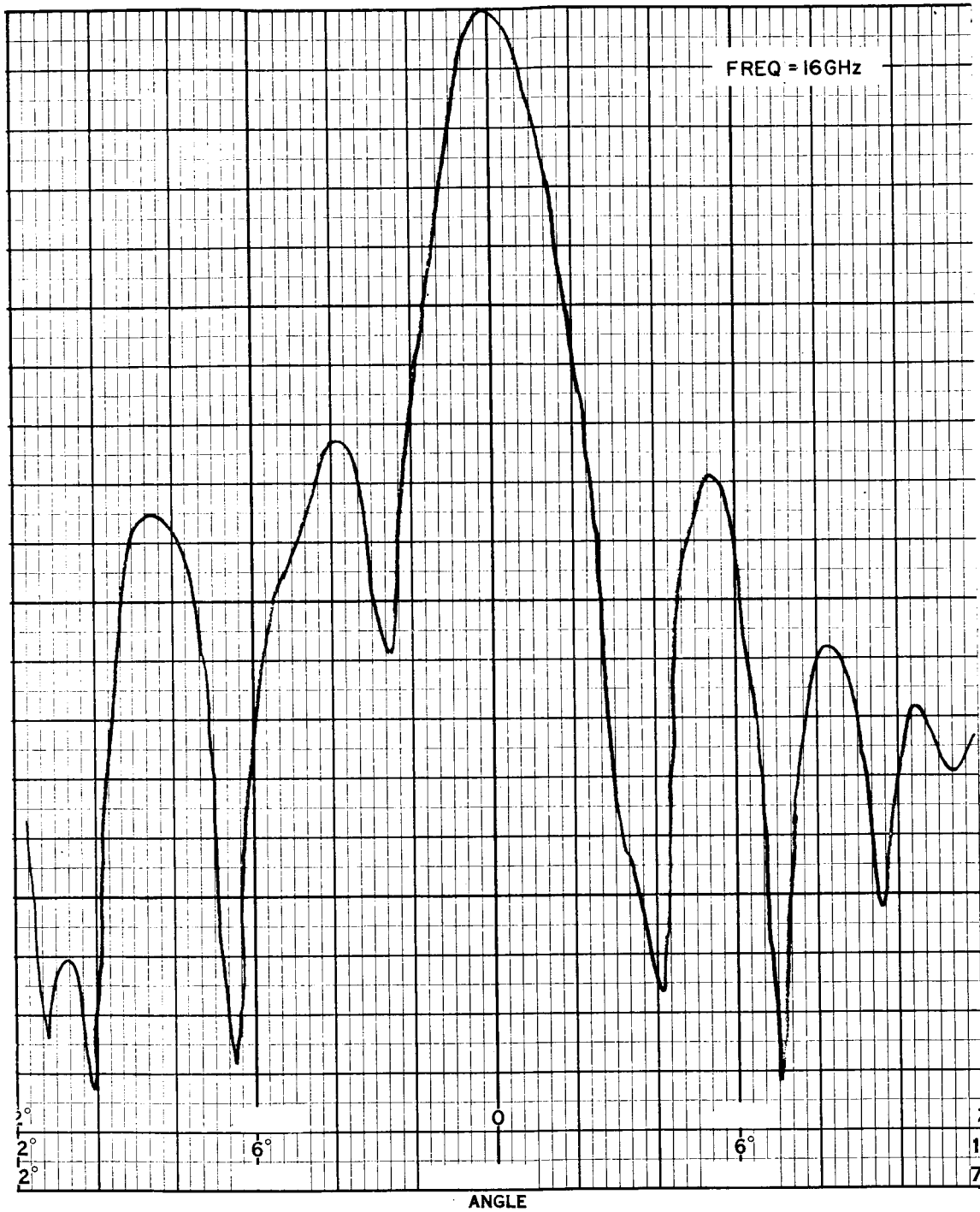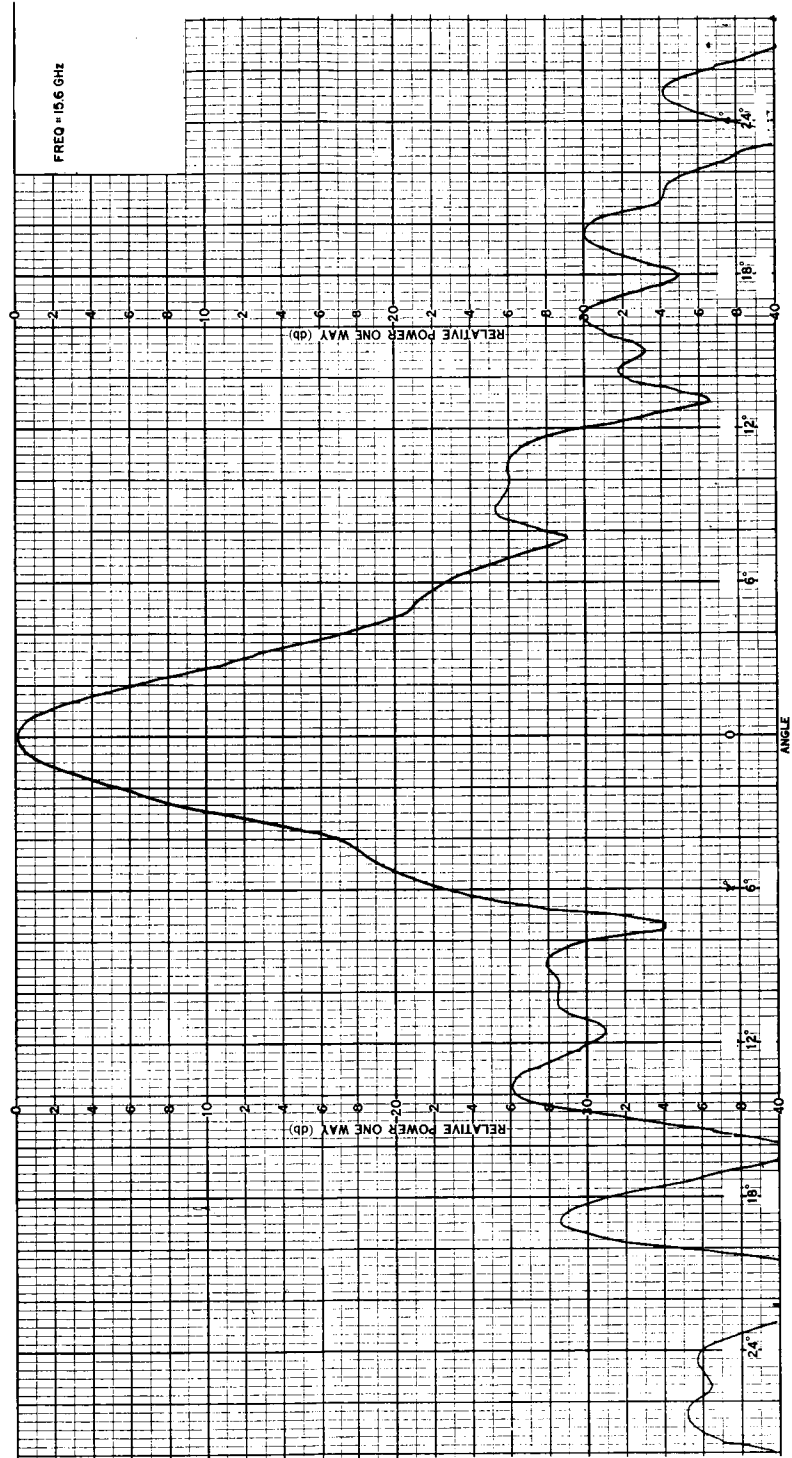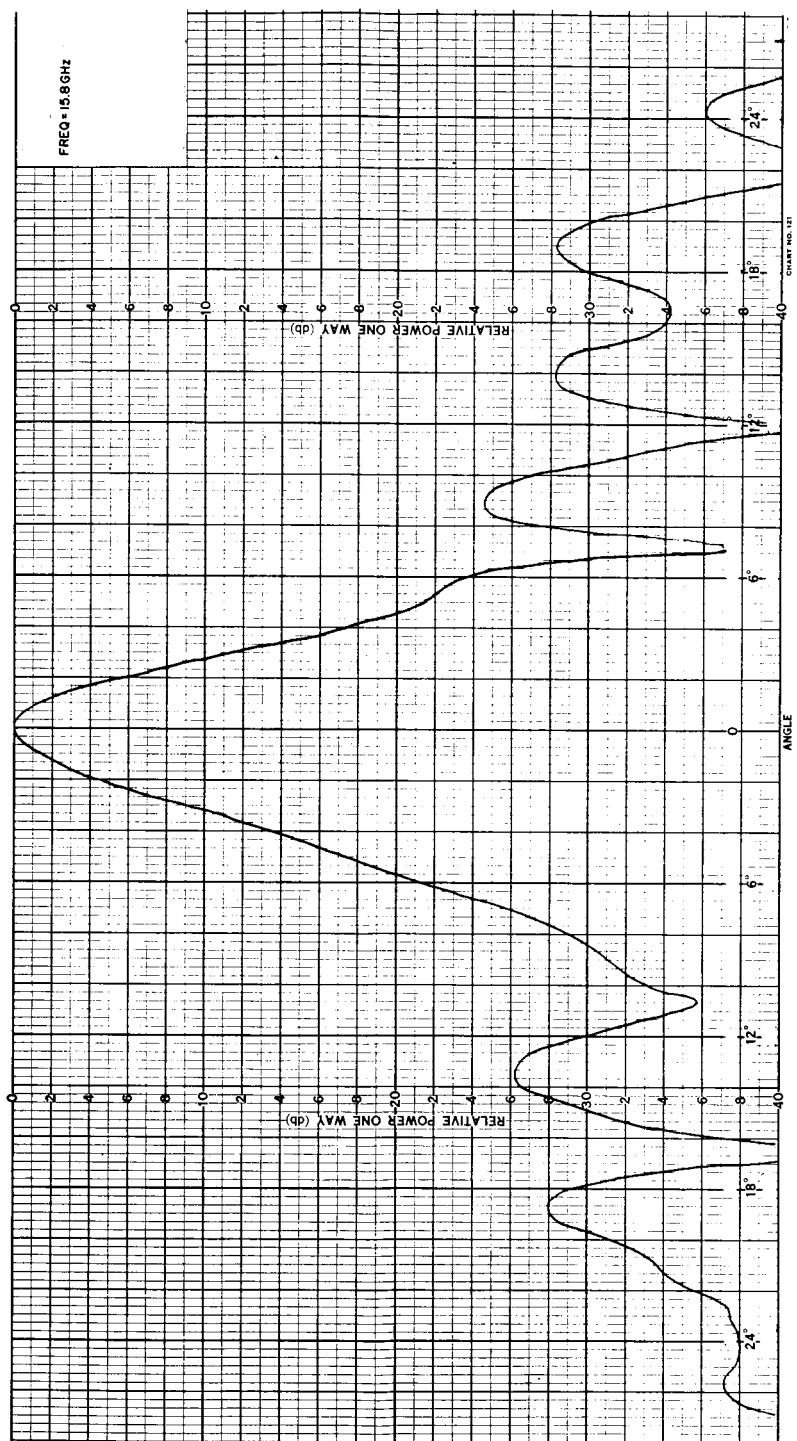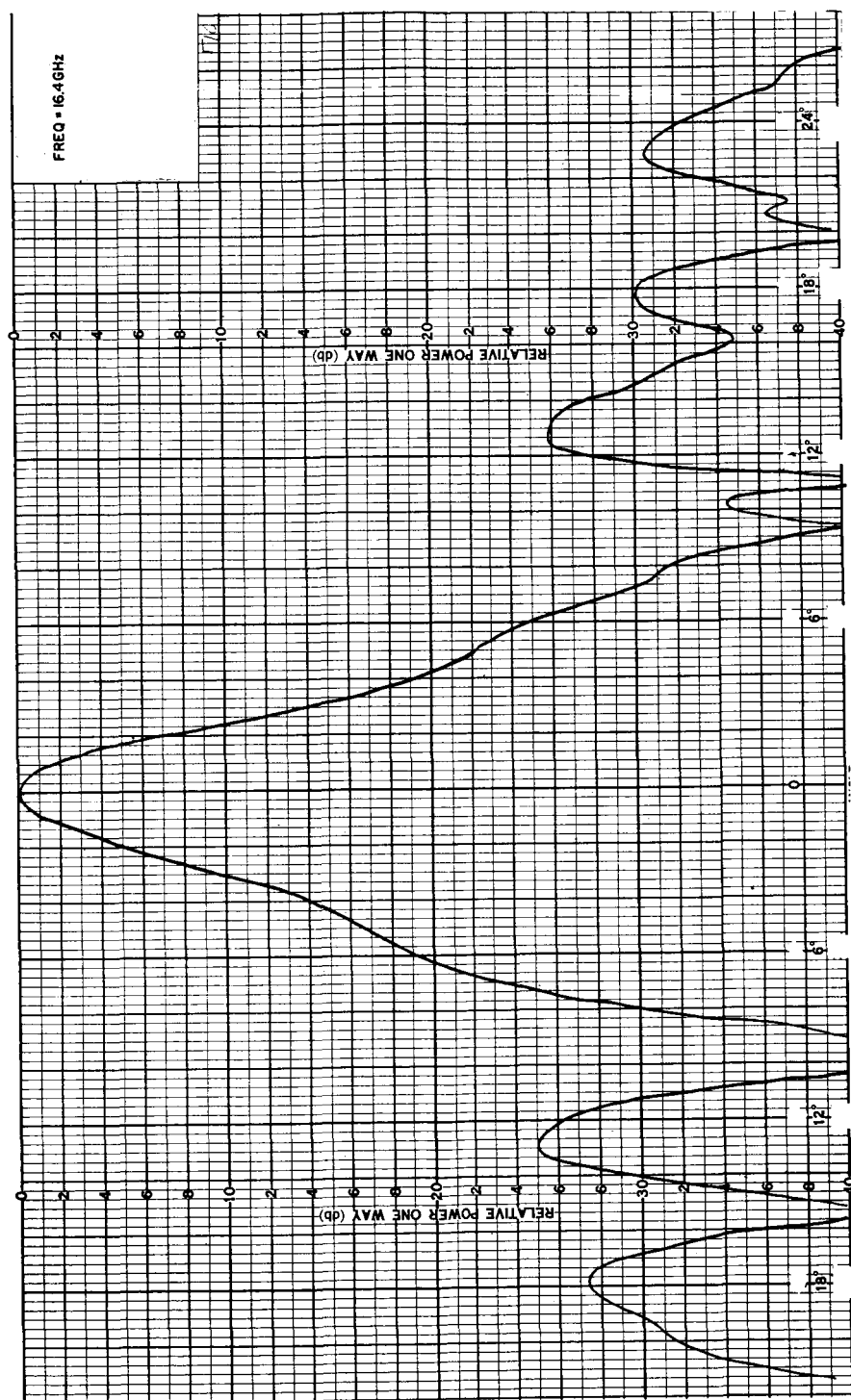Figure 56e. $H_{10} + H_{11}$ Mode Pattern for Horn #4 (Sheet 5 of 5)

In order to obtain data from an active element in an array environment prior to the writing of this report, the single reduced-width horn-lens model was modified and combined with the two five-element dummy arrays representing a single active element with five dummy elements disposed on either side. Antenna patterns of the real element were recorded both in and out of the array.

The reduced-width horn-lens model modification required machining of the horn walls to a .050 inch thickness. Patterns of the isolated horn, measured after this modification, did not fully agree with those measured before modification. Maximum side-lobe levels increased from approximately -26 dB to -22 to -24 dB.

E-plane patterns of the multimode horn-lens model measured in and out of the dummy array environment with dummy elements terminated, were essentially identical. The effect of adjacent elements on the E-plane pattern of the multimode line source appears to be negligible.

A complete investigation of the effects of an array environment on the multimode line source gain E- and H-plane, radiation patterns and impedance will be performed upon completion of fabrication of the three-active-element array.

ANALYSIS OF EFFECTS OF PHASE SHIFTER ERRORS

An analysis has been performed to determine the effect of phase shifter errors on multimode array pattern characteristics. An expression was derived for the radiation pattern of a 37-element parallel array of multimode line sources combined through a multimode beam former. The expression for the pattern in spherical coordinates is given by

$$G(\theta, \phi) = f(\theta, \phi) \sum_{n=-18}^{18} e^{j(\alpha_n + \beta_n + \psi_n)} (1 + B \cos \pi n/18) \tag{33}$$

where n = element number

$\quad$ B = a_{11}/a_{10} = 0.8

$\quad$ $f(\theta, \phi)$ = multimode element pattern

$\quad\quad$ α_n = element phase for beam scanning

$\quad\quad$ β_n = phase error due to phase shifter

$\quad\quad$ ψ_n = $2\pi/\lambda$ ns sin θ cos ϕ

$\quad\quad$ S = spacing between elements

In the above expression the multimode element pattern $f(\theta, \phi)$ is

$$f(\theta, \phi) = \left(\frac{1 + \cos\theta}{2}\right)\left[\frac{\sin u_b \cos u_a}{u_b\left\{(\pi/2)^2 - u_a^2\right\}} + \frac{B u_b \sin u_a \cos u_a}{\left\{\pi^2 - u_b^2\right\}\left\{(\pi/2)^2 - u_a^2\right\}}\right] \tag{34}$$

where $u_b = \pi b/\lambda \sin \theta \sin \phi$

$\quad$ $u_a = \pi a/\lambda \sin \theta \sin \phi$

b and a are respectively the line source E and H-plane dimensions.

It is assumed that a 5 bit digital ferrite phase shifter will be employed to provide phase quantization sidelobes consistent with the array requirements. Phase shifter tolerances per bit are tabulated below.

Bit	$\Delta\beta$ (3σ value)
180°	± 5°
90°	± 5°
45°	± 3°
22.5°	± 3°
11.25°	± 3°

The phase shifter tolerances per bit are based on previous work done at RCA on similar C-band ferrite digital phase shifters. In addition to the phase tolerance per bit, a total insertion phase tolerance of ±15° (3σ value) must be included. This again is based on previously obtained data.

A normal distribution of errors was assumed for all cases and a random process was employed to permit determination of the phase error due to the phase shifters on a per element basis. This data was then applied to equation (33) and patterns for broadside and various scan conditions were computed on an IBM 1620 computer.

For the array receiving at broadside, the phase shifter insertion phase tolerance causes an increase in the maximum sidelobe level from −38.5 to −30 dB. This represents a decrease of beam efficiency to 96% from the theoretical value which exceeded 99%.

The effect of phase shifter errors on the radiation pattern for various scan angles is presently being determined.

CONCLUSIONS

The multimode E-plane sectoral horn line source provides patterns which exhibit very low sidelobe levels. An array of such elements combined through a like multimode sectoral horn with divided outputs will result in an array characterized by low sidelobes in all planes and very high beam efficiency.

Basically, two line source designs have been extensively evaluated. The initial line source for the staggered array configuration had excellent pattern characteristics over a 10% frequency band with maximum sidelobes less than -30 dB over at least half of this band. The modified reduced-width model exhibited somewhat higher sidelobe levels for operation over a 5% frequency band. The reduced-width model was fabricated from the initial line source model and because of its reduced width is more sensitive to tolerance variation. The fact that two fabrication processes were required in construction of the reduced width model and the probability of increased fabrication error due to the two processes may account for differences in performance between the two models. An array of three reduced-width models is currently being fabricated for evaluation in a dummy array configuration. Additional work will be done to further improve pattern characteristics upon completion of fabrication.

Analysis of the staggered array configuration revealed the existence of a grating lobe pair off the scan axis which would occur in visible space as the beam is scanned a few degrees. These additional lobes significantly reduce beam efficiency as the beam is scanned rendering this configuration undesirable for the intended application.

A parallel array of the reduced width horns is suitable for operation with ± 30° beam scan at the expense of reduced bandwidth to approximately 5%.

An analysis of phase shifter errors indicates a 5-bit phase shifter will not seriously degrade array performance at broadside.

REFERENCES

1. P. D. Potter, "A New Horn Antenna with Suppressed Sidelobes and Equal Beamwidths", The Microwave Journal, pp. 71-78, June 1963.

2. P. A. Jensen, "A Low-Noise Multimode Cassegrain Monopulse Feed with Polarization Diversity", NEREM Record, pp. 94-95, 1963.

3. S. W. Drabowitch, "Multimode Antennas", The Microwave Journal, pp. 41-51, January 1966.

4.   C. E. Profera Jr., L. H. Yorinks "A High Efficiency Dual Frequency Multi-mode Monopulse Antenna Feed System", Supp. to IEEE Trans. on Aerospace and Electronic Systems, Vol. AES-2 No. 6, Nov. 1966.

5.   N. Marcuvitz, "Waveguide Handbook", MIT Radiation Laboratory Series, Vol. 10, McGraw-Hill.

6.   S. Silver, "Microwave Antenna Theory and Design", MIT Radiation Laboratory Series, Vol. 12, McGraw-Hill.

7.   H. Jasik, "Antenna Engineering Handbook", Chap. 14, McGraw-Hill, 1961.

8.   P. H. Vartanian et al, "Propagation in Dielectric Slab Loaded Waveguide", IRE Transactions on Microwave Theory and Techniques, April 1958.

9.   J. L. Allen, "The Theory of Array Antennas", MIT Technical Report No. 323, July 1963.

NEW TECHNOLOGY APPENDIX

ITEM 1   MULTIMODE LINE-SOURCE ELEMENT

Pages of this report wherein the above item is described are: 11, 14, 40, 58 and referenced figure pages.

APPENDIX A

GRATING LOBE ANALYSIS FOR OFFSET ARRAY

A calculation of the array pattern in direction cosine space was made to determine the grating lobe structure associated with the staggered array of multimode line sources. The array configuration shown in Figure A-1 was analyzed as a linear array of multimode half elements with progressive phase shift applied between half elements.
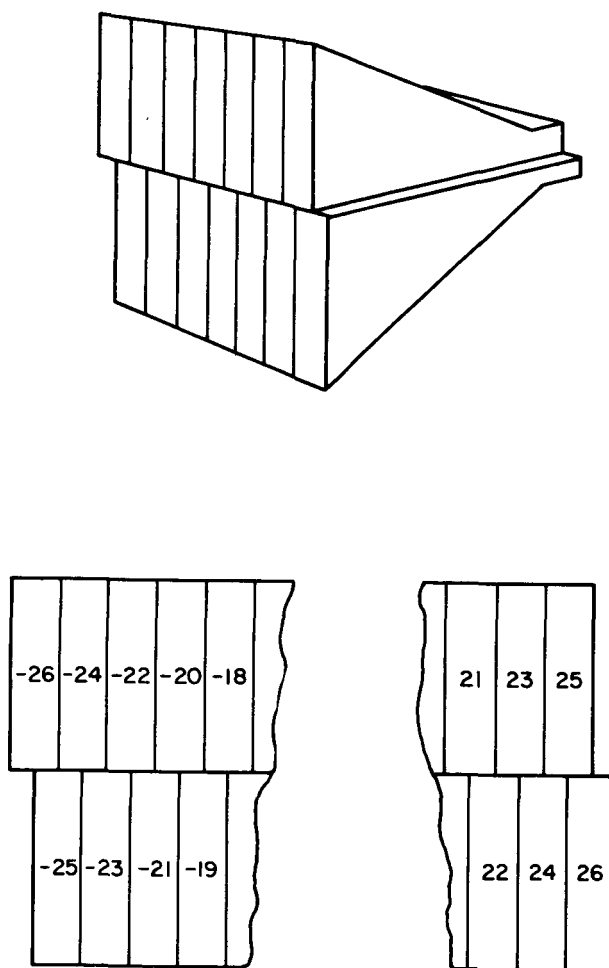

Figure A-1. Staggered Multi-Mode Half-Element Array

Initially the multimode half-element pattern was determined in real space and transformed to direction cosine space. For the multimode half element shown in Figure A-2, the radiation pattern in spherical coordinates is

$$g(\theta,\phi) = \left[\frac{j\frac{\ell}{2}\left(1 - e^{ju_1 \cos\phi}\right)}{u_1 \cos\phi} - \frac{j B \frac{\ell}{2}(u_1 \cos\phi)}{\pi^2 - (u_1 \cos\phi)^2}\left(1 + e^{ju_1 \cos\phi}\right) \right]$$

$$\times \left[\frac{\pi a/2}{(\pi/2)^2 - (u_a \sin\phi)^2} \right] \cos(u_a \sin\phi) \tag{A-1}$$

where $u_1 = \pi\ell/\lambda \sin\theta$

$u_a = \pi a/\lambda \sin\theta$
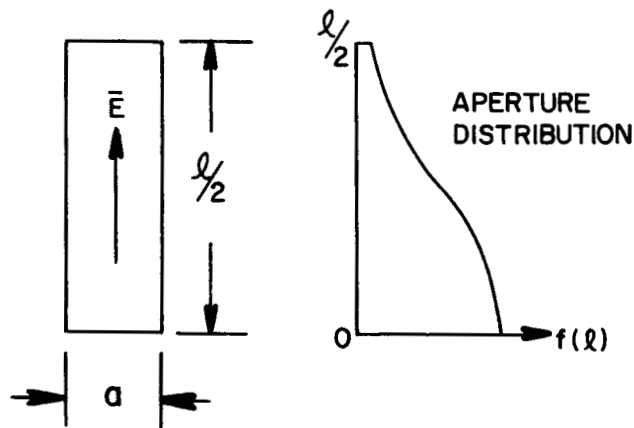
$B = a_{11}/a_{10}$

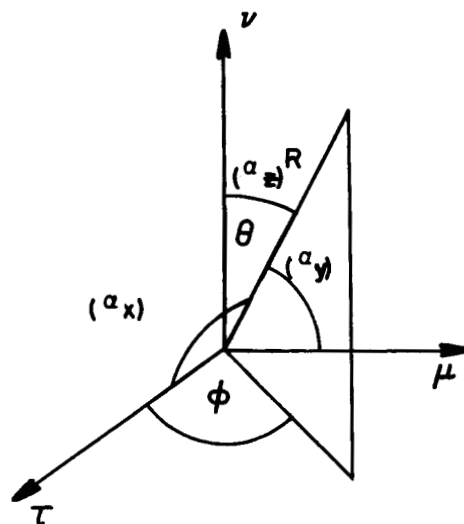Figure A-2. Half-Element Geometry

Figure A-3. Spherical Coordinates & Direction Cosine Space

Transformation from spherical coordinates to direction cosine space, illustrated in Figure A-3, is accomplished using the following relationships

$$\sin \theta = \left[\tau^2 + \mu^2\right]^{1/2} \tag{A-2}$$

$$\cos \phi = \frac{\tau}{\left(\tau^2 + \mu^2\right)^{1/2}} \tag{A-3}$$

where

$$\tau = \cos \alpha_x$$

$$\mu = \cos \alpha_y$$

Using the transformation identities shown above, the element function in direction cosine space is found to be

$$g(\tau, \mu) = \frac{A\ell}{4}\left[\frac{j(1 - e^{\frac{j\pi\ell}{\lambda}}\tau)}{(\pi\ell/\lambda)\tau} - \frac{jB\frac{\pi\ell}{\lambda}\tau}{\pi^2 - \left(\frac{\pi\ell}{\lambda}\tau\right)^2}\left(1 + e^{\frac{j\pi\ell}{\lambda}}\right)\tau\right]$$

$$\times \left[\frac{\pi}{(\pi/2)^2 - \left(\frac{\pi a}{\lambda}\mu\right)^2}\cos\left(\frac{\pi a}{\lambda}\mu\right)\right] \tag{A-4}$$

The radiation pattern of a linear array of n elements is

$$G(\theta, \phi) = g(\theta, \phi)\sum_n i_n \exp\left[jK\overline{\rho_n} \cdot \overline{R}\right] \tag{A-5}$$

where in spherical coordinates

$$\overset{>}{R} = \sin\theta \cos\phi\, \overline{i}_x + \sin\theta \sin\phi\, \overline{i}_y + \cos\theta\, \overline{i}_z$$

$$\overline{R} = \text{unit radial vector} = \tau\overline{i}_x + \mu\overline{i}_y + \nu\overline{i}_z$$

and

$$\rho_n = \text{vector from array center to } n^{th} \text{ element}$$

$$i_n = \text{current in } n^{th} \text{ element}$$

$$K = 2\pi/\lambda$$

The corresponding array pattern in direction cosine space is (Ref. 9)

$$G(\tau,\mu) = g(\tau,\mu) \sum_n i_n \exp\left[jKns\mu\right] \qquad \text{(A-6)}$$

where

S = spacing between adjacent elements.

For the 52 multimode half element array configuration in Figure A-1 employing multimode power combining the complete array pattern in direction cosine space is

$$
\begin{aligned}
G(\tau,\mu) = g(\tau,\mu) &\left\{ \sum_1^{26} \left(1+B\cos\frac{\pi n}{26}\right) \exp\left[jK\mu\frac{(2n-1)a}{4}\right] \right. \\
& n \text{ odd} \\
&+ \sum_{-1}^{-26} \left(1+B\cos\frac{\pi n}{26}\right) \exp\left[jK\mu\frac{(2n+1)}{4}a\right] \Bigg\} \\
& n \text{ even} \\
+ g(-\tau,\mu) &\left\{ \sum_1^{26} \left(1+B\cos\frac{\pi n}{26}\right) \exp\left[jK\mu\frac{(2n-1)a}{4}\right] \right. \qquad \text{(A-7)} \\
& n \text{ even} \\
&+ \sum_{-1}^{-26} \left(1+B\cos\frac{\pi n}{26}\right) \exp\left[jK\mu\frac{(2n+1)a}{4}\right] \Bigg\} \\
& n \text{ odd}
\end{aligned}
$$

where

$$ns = \frac{(2n-1)a}{4} \quad (n>0); \quad ns = \frac{(2n+1)a}{4} \quad (n<0); \quad B = a_{11}/a_{10}$$

Equation (A-7) was programmed for computation on an IBM 1620 computer. The resulting data indicates the location of pattern maxima as a function of τ and μ. The grating lobe locations in real and imaginary space can then be easily determined as a function of pattern scan angle. The pattern maxima of equation (A-7) plotted in the τ, μ plane are shown in Figure A-4.

A-4

array with single plane scanning, the translation of the unit circle is related to the phase difference between elements βr in radians by the following relationship

$$\mu_o = \frac{\beta_r}{KS} \qquad K = 2\,\pi/\lambda$$

But the scan angle, θ_s, is determined from the following expression

$$\sin\theta_s = \beta_r/S_r$$

where S_r is expressed in radians and equals KS. Hence the translation and scan angle θ_s are related by the following equation

$$\mu_o = \sin\theta_s$$

As the beam is scanned, the off-axis grating lobes on one side of the main beam appear in visible space when the scan angle is approximately 6°. The level of the grating lobes increases relative to the main lobe as the main lobe is scanned. This increase is caused by the element factor $g\,(\tau,\ \mu)$ which is always maximum at the center of the unity circle. Since the computed grating lobe levels represent a significant amount of power removed from the main beam, beam efficiency is drastically reduced. For this reason, the staggered-element array concept will not be useful for the radiometer application and was abandoned in favor of the parallel array.
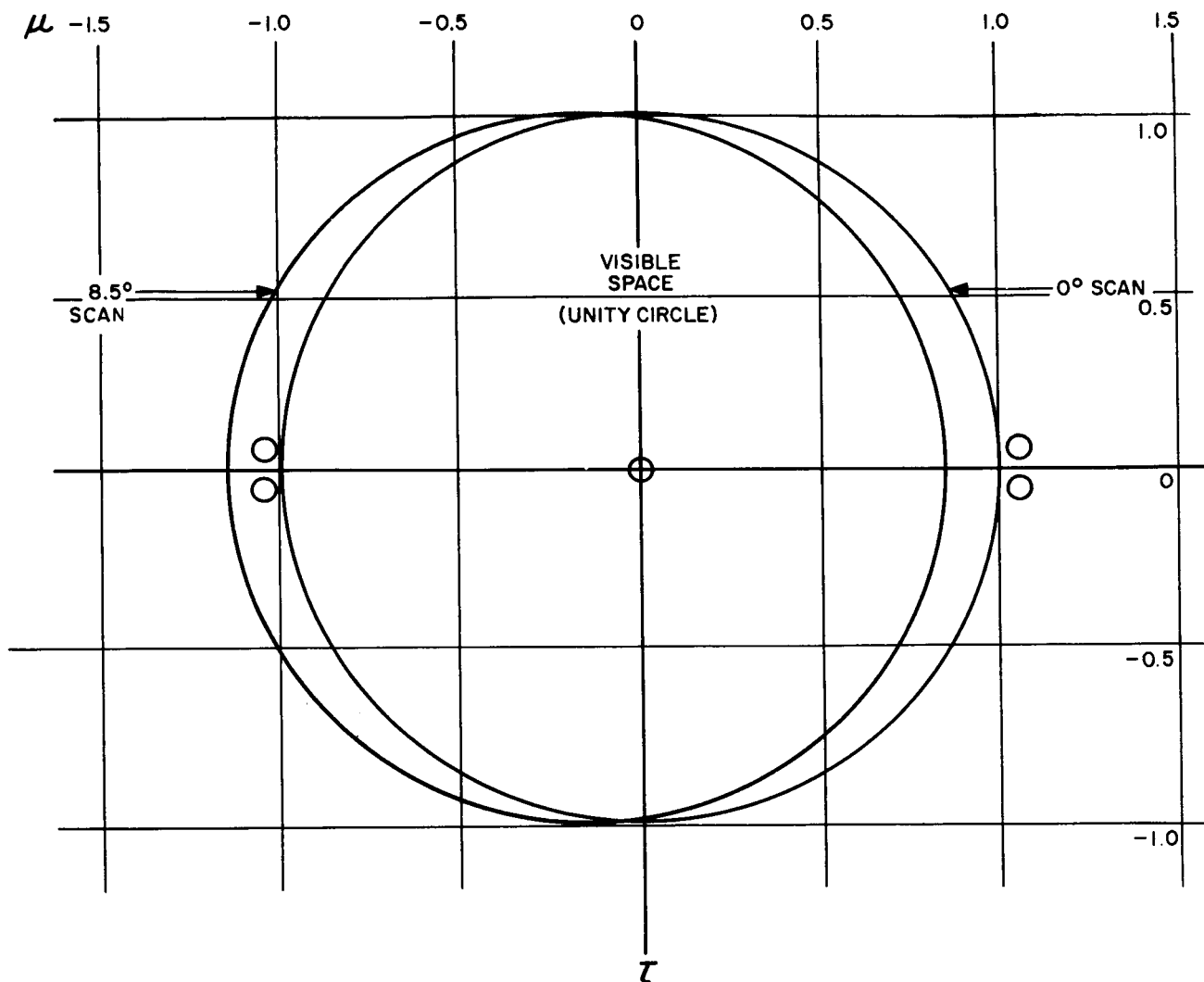
Figure A-4. Grating Lobes in τ, U Space for Staggered Array

As shown in Figure A-4 no grating lobes are located along the scan axis ($\tau = 0$), however, -13.8-dB grating lobes are located off the scan axis at $\mu = \pm1.1$, $\tau = \pm0.5$. These occur outside real space for broadside operation of the array. Real space for broadside operation is indicated by the circle of unity radius centered at $\tau = \mu = 0$, the location of the main beam maximum. Scanning the beam in real space is equivalent to translation of the unity circle in direction cosine space. For the multimode staggered

A-5